Plasmon-Enhanced Silicon Nanocrystal Luminescence for Optoelectronic Applications

Thesis by
Julie Suzanne Biteen

In Partial Fulfillment of the Requirements
for the Degree of
Doctor of Philosophy

California Institute of Technology
Pasadena, California

2006

(Defended May 25, 2006)

Acknowledgements

When I first entered graduate school, I was known as the cheery girl in pink who would claim, "I love it here" to anyone within shouting distance. As a result, I was repeatedly warned that my love for science, Caltech, and Southern California would all wear out. Well, five years later, I am proud to say that I haven't become all too jaded, and it is with great pleasure that I thank the people who have made my time in graduate school such a wonderful adventure.

The most important thanks go to Harry Atwater, who has been a terrific advisor. I have benefited strongly from his creative project ideas, his support, and his guidance. Above all, Harry's energy, enthusiasm, and positivity are awe-inspiring. Even on his busiest days, I have never seen Harry turn away a student needing answers, advice, or a sounding board. I'm not sure how he has remained interested, alert, and intelligent in the midst of so many commitments, but Harry has been a tremendous role model for me.

I am also indebted to Nate Lewis, who agreed to be my co-advisor and opened the doors to his lab group for me without hesitation when I approached him ripe with fears of an Atwater group move to Boston. In addition to helping me keep a foot in the world of chemistry, Nate has always been willing to help me out with research feedback, writing corrections, and career advice.

I appreciate the willingness of my committee members, Professors Jim Heath, Bill Goddard, and Rick Flagan, to come across to my side of campus for my candidacy and propositions exams, to discuss my work and interests, and to provide me with excellent feedback.

Hopefully I have not been spoiled by my graduate school experience. I feel so fortunate to have had the opportunity to present my work at many conferences and to participate in several intercontinental research collaborations. Most notably, my learning experience has benefited tremendously from collaborating with Albert Polman and his group at the FOM-AMOLF institute in Amsterdam. During my two stays in Amsterdam and during his sabbatical visit to Caltech, Albert has

always treated me as one of his own students, and I've really appreciated his wonderful ideas and his practical nature, whether he was aiding me with project planning or paper writing.

The students and postdoctoral researchers at AMOLF were all wonderful to me. I owe a huge thank you to Hans Mertens, with whom I have been working very closely for the past year. I really appreciate his dedication and work ethic; without his push, our collaboration on plasmon-enhanced luminescence would never have been so fruitful. I thank Hans not only for the knowledge and deep thinking that he has brought to our discussions, but also for his patience, which must have been tried while working side by side with me for hours on end. Also at AMOLF, in my first year of graduate school, Anna Tchebotareva served as an excellent role model for what it is like to be a serious researcher, in terms of her enthusiasm and dedication.

I am very fortunate to have been a member of the Atwater group, where I was surrounded by a collection of intelligent, knowledgeable, and interested people. Everyone has a distinct academic background, and as a result, I almost never had to leave the second floor of the Watson building to get help or feedback, regardless of the problem at hand. In particular, this thesis would not have been possible without my two classmates, Robb Walters and Luke Sweatlock, who are two of the smartest men I have ever met. Robb is a wonderful experimentalist and never complained about spending hours helping me set up optics experiments, and Luke combines brilliant physics intuition with fabulous communication skills when explaining concepts in electromagnetism. I also want to thank Domenico Pacifici, who joined the group a few years ago with an explosion of energy. Domenico has great insight and a deep understanding of semiconductor photonics, and is completely selfless about helping his labmates, even when that means giving away his time in the optics lab to them. I also learned a lot from productive discussions with the other plasmonics researchers in the group: Jen Dionne, Henri Lezec, and Carrie Ross.

In addition to scientific knowledge and experience, my labmates in the Atwater

group have provided me with support and friendship, and I thank them for that. For the past three years, Christine Richardson has regaled me with the daily misadventures of Aiden and Dillon and proofread every resume I've ever sent out. Maribeth Mason shared my love for J. Lo and spider solitaire; the office hasn't been the same since she graduated. In addition to making work more pleasant with his stories, Brendan Kayes has provided the indie pop soundtrack to many of my working days. Once he starts talking, he rarely stops, so it's no surprise that I happily wiled away many hours chatting with Jimmy Zahler. Jen Ruglovsky introduced me to online shoe shopping and shared the experience of dating a mechanical engineer with me. Indeed, all of the people with whom I've overlapped in the Atwater group have contributed to my academic and social life; for this I thank Julie and Rhett Brewer, Matt Dicken, Ken Diest, Tao Feng, Anna Fontcuberta i Morral, Melissa Griggs, Jason Holt, Ben Kaufmann, Michael Kelzenberg, Pieter Kik, Sungjee Kim, Krista Langeland, Stefan Maier, Young Bae Park, Morgan Putnam, Cecily Ryan, and Katsu Tanabe.

I haven't gotten to know the members of my second group as well as I wish I had, since I've really enjoyed what interactions I have had with the members of the Lewis group. In particular, thanks to Lauren Webb for very, very patiently teaching me to alkylate silicon and use the XPS, as well as for being a tireless wealth of information on surface chemistry. Thanks also to Matt Traub, Bruce Brunschwig, and Dave Michalak for thought-provoking questions and feedback.

My studies of surface states on silicon nanocrystals were brought to a new level because of the terrific computational work of Professor Giulia Galli and her group at Lawrence Livermore. Thanks in particular to Giulia Galli, Aaron Puzder, and Andrew Williamson for many fruitful conversations. On the other hand, the plasmon enhancement portion of my thesis began after Professor Jonah Erlebacher of Johns Hopkins University told Harry about his group's work on nanoporous gold. Thanks to Dr. Erlebacher for inviting me out to Baltimore to learn how to make and characterize this interesting material that turned out to be a great match for silicon nanocrystals.

I have found the Caltech scientific community as a whole to be a very interactive group, and I am grateful to all of the wonderful scientists of all levels who have played a role in my time here. Thanks to Michael Gordon, who so patiently taught me about ion beamlines during my first few months at Caltech, Issac Garcia-Munoz, my summer student who made starting the plasmon enhancement work much more fun, David Boyd, who made colloidal gold samples for me to see if we could improve our enhancements, Dean Holunga, who synthesized silicon nanocrystals in his aerosol reactor for me, and Hsin-Ying Chiu, who wire-bonded my LED devices. I am also indebted to the staff in Watson for all their help. In particular, Eleonora Chetverikova, Ali Ghaffari, Irene Loera, Cierina Marks, Mary Metz, and April Neidholt really made my time here go smoothly.

Writing my thesis has felt overwhelming at times, so I'm really appreciative of all the last-minute proofreading and feedback that I got from Jen Dionne, Brendan Kayes, Stuart Laurence, Hans Mertens, Domenico Pacifici, Luke Sweatlock, and Robert Walters.

My sanity has been retained by leaving lab every so often, and when I do that, I'm so fortunate to have made fabulous friends at Caltech. From the international students I met during my first week in Pasadena to the girlfriends who are always around for coffee or a drink, I feel so lucky to always have the support and camaraderie of these supportive, interesting, and fun individuals. I am also thankful to have had the enduring support of my friends from Princeton and Montreal, whose voices on the phone have allowed me to feel a little less far from home.

I am grateful to my parents and my brother, Dale, Jeff, and Andrew Biteen, who have been so supportive from afar. They have all done their best to figure out the appropriate times to celebrate or to sympathize with me as I have struggled through a world so foreign to them.

Finally, thank you to Eric Johnsen, my husband, my partner, and my true love. For the past five years, I have had the joy and privilege to share all of my successes and all of my fears with this wonderful man, and without his support, nothing would have ever been possible.

Plasmon-Enhanced Silicon Nanocrystal Luminescence for Optoelectronic Applications

by Julie Suzanne Biteen

Abstract

On the path toward the realization of silicon-based optical emitters for integrated microelectronics, this thesis studies the optoelectronic properties of silicon nanocrystals as a function of their surface passivation and their interactions with plasmonic materials. The first part of the thesis utilizes controlled oxidation exposures and photoluminescence spectroscopy to verify previous theoretical and computational predictions of oxygen-related surface states that effectively narrow the energy band gap of small silicon nanocrystals. The focus of the second half of the thesis is on experimental and computational studies of enhanced luminescence from silicon nanocrystals in the near field of noble metal nanostructures.

Surface plasmon enhancement is a technique that has only recently been applied to semiconductor nanocrystal luminescence. This thesis thoroughly investigates the emission of silicon nanocrystals coupled to gold and silver nanostructures to achieve a new level of understanding of the enhancement effect. By pairing silicon nanocrystals to metal nanostructures, up to ten-fold increases in the luminescence intensity are realized, concomitant with enhancements of the radiative decay rate, the absorbance cross section, and the quantum efficiency. Moreover, coupling at the plasmon resonance frequency is used to tune the nanocrystal emission spectrum. A computational exploration of these experimental observations indicates that the enhancement effects can be ascribed to emission in the concentrated local field that results from the excitation of metal particle plasmon modes. Finally, the process of coupling silicon nanocrystal emitters to plasmonic metals is applied to a silicon-nanocrystal light-emitting diode, and enhanced electroluminescence is realized.

Contents

List of Figures

List of Publications

Portions of the material presented here have appeared in the following references and are reproduced with permission:

Julie S. Biteen, Luke A. Sweatlock, Hans Mertens, Nathan S. Lewis, Harry A. Atwater, and Albert Polman, "Electromagnetic simulations of resonant plasmon enhancement of silicon quantum dot photoluminescence," *in preparation.*

Hans Mertens, Julie S. Biteen, Robert J. Walters, Nathan S. Lewis, Harry A. Atwater, and Albert Polman, "Plasmon-enhanced electroluminescence from silicon quantum dots," *in preparation.*

Julie S. Biteen, Nathan S. Lewis, Harry A. Atwater, Hans Mertens, and Albert Polman, "Spectral tuning of plasmon-enhanced silicon quantum dot luminescence," Applied Physics Letters **88**, 131109 (2006).

Julie S. Biteen, Domenico Pacifici, Nathan S. Lewis, and Harry A. Atwater, "Enhanced radiative emission rate and quantum efficiency in coupled silicon nanocrystal-nanostructured gold emitters," Nano Letters **5**, 1768 (2005).

Julie S. Biteen, Nathan S. Lewis, Harry A. Atwater, and Albert Polman, "Size-dependent oxygen-related electronic states in silicon nanocrystals," Applied Physics Letters **84**, 5389 (2004).

Julie S. Biteen, Anna L. Tchebotareva, Albert Polman, Nathan S. Lewis, and Harry A. Atwater, "Controlled passivation and luminescence blue shifts of isolated silicon nanocrystals," MRS Proceedings **770**, I6.2.1 (2003).

Chapter 1

Introduction

1.1 Silicon-Based Photonics

As device dimensions decrease to ever smaller sizes, new miniaturization strategies are sought. In 1965, Gordon Moore predicted that the number of transistors incorporated in a chip will double every 24 months,[1] and, forty years later, device dimensions continue to scale down accordingly. In addition to enabling the conveniences afforded to us by today's microelectronic devices, such as wireless phones and personal computers, this miniaturization of electronics has led to improved speed and performance, as well as to lower power consumption. As microcomponents—or increasingly nowadays, "nanocomponents"—become smaller and more densely packed, the traditional electrical interconnects between areas on a chip become increasingly impractical. These wires are bulky, and heat dissipation resulting from signal propagation along them causes the device reliability to suffer.

In the long term, traditional interconnect solutions will cease to be effective in microelectronics design strategies.[2] Optical interconnects provide a pragmatic and efficient alternative for satisfying performance requirements by overcoming propagation delay, power, and bandwidth limitations. Since transferring energy via optical signals requires an on-chip emitter and detector, an important materials and process integration challenge in the semiconductors community is the development of new technologies to perform these functions.

The integration challenges for combining photonic and electronic components on a chip are not trivial. Currently, silicon-based complementary metal oxide semiconductor (CMOS) fabrication dominates the semiconductor world, and silicon microelectronics has benefited enormously from this economy of scale. Jack Kilby said in 1976, "One of the great strengths of the integrated circuit concept has always been that it could draw on the mainstream efforts of the semiconductor industry,"[3] and so too do microphotonics seek to profit from this already existent infrastructure. Silicon-based waveguides, modulators, and detectors have been realized, but the actualization of practical, efficient, CMOS-compatible silicon light-emitting devices (LEDs) and lasers has yet to occur.

The purpose of this thesis is to examine the photophysics of silicon-based light emitters. We will explore the novel possibility of tuning silicon nanocrystal emission through surface modifications and coupling to plasmonic metals, investigate ways of enhancing the overall emission, and, finally, examine the potential for integrating such bright, efficient emitters into electrically pumped devices.

1.2 Semiconductor Nanocrystal Optoelectronics

1.2.1 Silicon Nanocrystals

Silicon is the most prevalent material in the electronics world, not only because of its abundance and low cost, but also because it has a high-quality, stable oxide that provides excellent electronic passivation. However, due to its indirect band gap, the electronic structure of silicon prevents this material from being a strong light emitter. In indirect band gap semiconductors like silicon, there is a mismatch in momentum space between the electron and hole states. To conserve momentum, excitation and relaxation between the conduction band and valence band extrema require the assistance of a crystal lattice vibration. Radiative recombination of excited charge carriers is therefore a three-body process, and, as a result, it is much less efficient than the analogous two-body recombination in a direct band gap semiconductor, where the conduction and valence band extrema

are matched in momentum space. The low probability of radiative recombination in indirect band gap materials favors non-radiative decay processes, and excited electrons generally lose energy as heat, not emitted photons. These materials exhibit only very faint luminescence, even at low temperatures, and this weakness has traditionally prevented the desirable extension of silicon microelectronics to silicon optoelectronics; LEDs and lasers cannot be produced from bulk silicon.

Hope for using silicon as a light emitter was resurrected in 1990, when Canham discovered that porous silicon, which has nanometer-scale features, exhibits efficient room-temperature photoluminescence at visible energies above the bulk Si band gap of 1.12 eV.[4,5] Here, photoluminescence (PL) refers to the emission of a photon upon the relaxation of an electron-hole pair (exciton) that has been excited by some external light source. The relaxation energy of the charge carriers is determined by the energy difference between the conduction and valence bands.

Since the discovery of room-temperature PL from porous silicon, considerable effort has been devoted to the development of silicon nanostructure-based light emission sources. The luminescence of Si nanocrystals has been studied in various systems, from single nanocrystals[6] to multilayered structures,[7] and efficient electroluminescence has also been reported.[8–10] Photoluminescent silicon nanostructures have been fabricated by many methods, including porous etching,[4] implantation of Si^+ ions,[11] aerosol synthesis,[12] rf co-sputtering of Si and SiO_2,[13] and chemical vapor deposition of silicon suboxides.[14] Though each system has unique advantages and disadvantages, the ion implantation method, which creates a Gaussian profile of excess Si in a SiO_2 substrate that is subsequently annealed to nucleate and grow nanocrystals, is a fully CMOS-compatible procedure. We therefore choose to work on silicon nanocrystals produced by ion implantation in order to explore the optoelectronics of this easily integratable system.

1.2.2 Quantum Dot Energetics

The origin of photoluminescence from silicon nanocrystals has been attributed to excitonic emission in a quantum-confined system.[15] When an exciton is created in

a nanocrystal with dimensions smaller than the excitonic Bohr radius, the electrons and holes are confined in real and reciprocal space. The Bohr radius of an exciton is a material-specific property; in bulk silicon, this length is 4.9 nm.[16] By disrupting the crystal symmetry, quantum confinement causes a relaxation of the momentum selection rules in the silicon nanocrystal. Radiative recombination is therefore a much more efficient process in silicon nanocrystals than in bulk silicon, and the emission efficiency skyrockets accordingly. Quantum-confined nanocrystals, or quantum dots, based on a wide range of semiconductor materials, are now being widely investigated as emitters, detectors, biological sensors, and solar cells; in the present thesis, we focus on the application of silicon nanocrystals as optical emitters for integrated photonics.

Quantum confinement has the effect of increasing the band gap of a material relative to the bulk value. Therfore, silicon nanocrystals emit in the near-infrared to visible range. In these systems, the emission of a photon upon the radiative recombination of quantum-confined excitons occurs at an energy that depends on the nanocrystal size, and the photoluminescence is size-tunable.[17] An analytical model, introduced by Brus in 1986, predicts that the quantum confinement effect in nanocrystals scales with confinement radius, r. Neglecting higher-order terms, the expected energy-size relationship in the simple reduced mass picture is[18]

$$E_{g,nc}(r) = E_{g,bulk} + \frac{\hbar^2\pi^2}{2m_{red}}r^{-2} - \frac{1.8e^2}{4\pi\epsilon_0\epsilon}r^{-1} \tag{1.1}$$

Here, $E_{g,nc}(r)$ is the band gap of the nanocrystal, which increases from the bulk value, $E_{g,bulk}$ (1.12 eV for silicon), as r decreases. The relative dielectric constant is given by ϵ, and the reduced mass is $m_{red} = (1/m_e + 1/m_h)^{-1}$, where m_e and m_h are the electron and hole effective masses, respectively. The dominant second term in Eq. (1.1) is the localization energy, which scales as r^{-2}, and the less important third term scales as r^{-1} to account for the shielded Coulomb interaction between electron and hole.

1.2.3 Surface States on Silicon Nanocrystals

For an optical emitter, the quantum efficiency is defined as the probability of radiative recombination following excitation. The efficiency of silicon nanocrystals, which can decay through radiative and non-radiative pathways, is therefore given by the ratio of the radiative decay rate to the total decay rate. As described in Section 1.2.2, quantum confinement leads to an enhancement in the radiative rate. In systems of silicon nanocrystals, one can additionally take advantage of the high-quality oxide to passivate the surface and therefore eliminate many non-radiative channels, such as dangling bonds and defect centers. This further enhances the quantum efficiency by reducing the total decay rate.

However, the effect of the silicon nanocrystal surface structure cannot be neglected. Indeed, despite the predicted essentially r^{-2} dependence of the nanocrystal band gap in Eq. (1.1), several experimental studies have indicated that, although the PL of silicon is indeed blue-shifted as its dimensions decrease, the shift is smaller than expected.[19,20] In addition, a relatively wide range of experimental PL measurements for small Si nanocrystals have been reported in the literature. In the majority of systems that have been investigated, the silicon nanocrystals are coordinated to oxygen at the surface, either because they are synthesized within a SiO_2 matrix or due to the rapid native oxidation of silicon surfaces in an aerobic environment. It is therefore difficult to separate the role of these surface groups from the intrinsic properties of the nanocrystals, but recent theoretical models suggest that localized states at the surface of these materials can in fact account for trends in experimental data.[21–23] A complete understanding of this effect has yet to be achieved.

1.2.4 Enhanced Luminescence

The radiative decay rate of silicon nanocrystals is typically found to be on the order of $10-100$ kHz. This is several orders of magnitude greater than the rate of radiative recombination in bulk silicon, leading to extremely high quantum

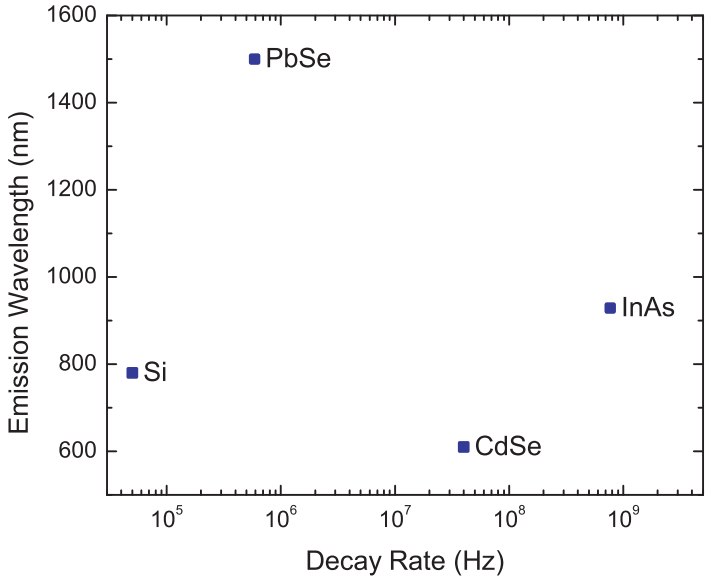

Figure 1.1: Comparison of emission wavelengths and decay rates for four different semiconductor nanocrystals based on literature values. The data for Si, PbSe, CdSe, and InAs are taken from references 24, 25, 26, and 27, respectively.

efficiencies ($\gtrsim 50\%$) in silicon nanocrystals.[24] Unfortunately, despite their high emission efficiency, the overall brightness of silicon nanocrystals is still limited. This is true because, though the PL intensity of an emitter depends on the quantum efficiency, it also depends strongly on the absorption cross section and the radiative decay rate. Unfortunately, the cross section and decay rate in silicon nanocrystals are still very low compared to those of dyes and direct band gap emitters.

This quandary is illustrated in Figs. 1.1 and 1.2. Based on a survey of the semiconductor quantum dot literature, in Fig. 1.1 we compare the emission wavelengths and total decay rates of silicon nanocrystals[24] to those of direct band gap semiconductor nanocrystals (PbSe,[25] CdSe,[26] and InAs[27]) produced by colloidal syntheses. The quantum efficiencies of these nanocrystals are not indicated in this Figure; these range from 10 to 50%. The total power, P, emitted by a semiconductor quantum dot is given by the product of the total decay rate, the emission energy, and the quantum efficiency, i.e.,

$$P = \Gamma_{exp} \times E_{emission} \times Q \tag{1.2}$$

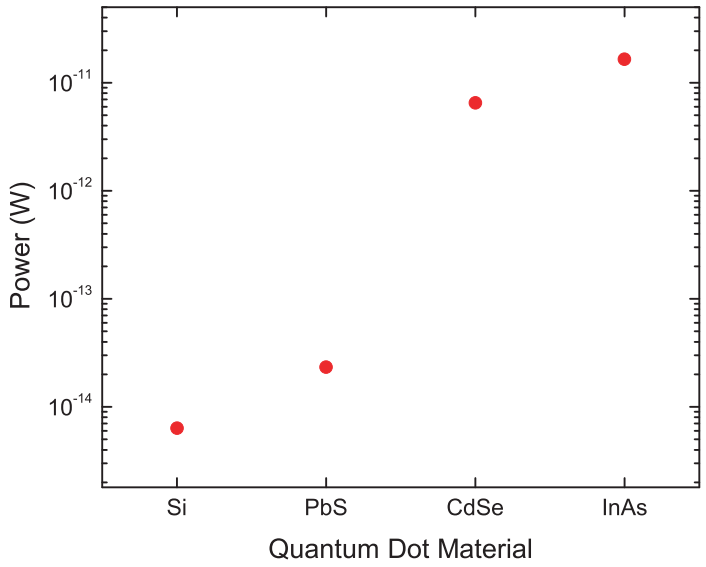

Figure 1.2: Emission power of four different semiconductor nanocrystals based on the data in Fig. 1.1.

For each of the nanocrystal materials in Fig. 1.1, we therefore computed the emitted power; this is given in Fig. 1.2. Here, it is clear that in order to compete with such direct band gap quantum dots as CdSe and InAs, the emission intensity of nc-Si must be enhanced by three orders of magnitude.

If one goal of the study of silicon nanocrystal luminescence is the realization of a photoemitter for integrated circuits, then it is important to attain much higher emission intensities. Several schemes for enhancing emission from a silicon-based emitter have been proposed. Among these approaches are defect engineering using silicon nanocrystals as sensitizers for secondary emitters, such as erbium ions,[28,29] and band structure engineering through alloying silicon to direct band gap materials like tin.[30,31] A more recent innovation has been the coupling of emitters like silicon nanocrystals to nanostructured metals.

Since 1974, sensing applications have been taking advantage of roughened metal surfaces to enhance the detected signal in Raman spectroscopy; this process is known as surface-enhanced Raman spectroscopy (SERS).[32] Though its origin is not fully understood, the SERS effect is widely attributed to the coupling of a molecular dipole to the highly concentrated electromagnetic field generated by a

resonantly oscillating surface plasmon mode in the roughened metal surface.[33] The electromagnetic effects that gave rise to SERS also spawned interest in related topics, including enhanced absorption and fluorescence in dye molecules near rough metal surfaces.[34] More recently, enhanced luminescence from semiconductor quantum dots and wells has been reported.[35–37] In the present thesis, we explore this strategy of coupling semiconductor emitters to plasmonic nanostructured noble metals, and extend the applications of plasmon enhancement to silicon nanocrystal photoluminescence and electroluminescence.

1.3 Outline of Thesis

In this thesis, we perform a thorough investigation of the photophysical properties of silicon nanocrystal (nc-Si) emitters as a function of their surface passivation and their interactions with plasmonic materials. Experimental and computational methods are used to further our understanding of silicon nanocrystal photonics, and we characterize the photoluminescence and electroluminescence of these emitters.

In Chapter 2, we investigate the effect of silicon nanocrystal surface passivation on the electronic band gap. Using a selective etching technique to isolate the nc-Si on a silicon substrate, we study the nanocrystal emission energy during controlled oxidation. Based on these experiments, we identify a size regime, that of nanocrystals with diameters $\lesssim 2.8$ nm, where oxidation leads to the presence of an intergap surface state that decreases the emission energy. This reduction in excitonic emission energy following oxidation is a first experimental verification of the formation of an oxygen-related excitonic recombination state for very small nc-Si. Using the same techniques that enabled the silicon nanocrystal surface oxidation experiments, other procedures, including physical manipulations of the nanocrystal density and chemical modifications of the nanocrystal surfaces, were performed; these are described in Appendix A.

Our treatment of the electromagnetic effects that give rise to enhanced emis-

sion upon coupling nc-Si to nanostructured metals begins in Chapter 3. There, we introduce the physics of nanoparticle surface plasmon polaritons, describe the theory of plasmonic field enhancement, and outline its connection to the radiative properties of dipole emitters, which include semiconductor nanocrystals. We present some full-field electromagnetic simulation results for lithographically attainable metal nanoparticle array configurations, and, based on these computations, we make predictions regarding the tunability of these arrays as a function of materials properties, dimensionality, and geometry.

Chapter 4 describes the first experimental realization of enhanced photoluminescence from nc-Si. This is achieved by coupling silicon nanocrystals to nanoporous gold, and varying the metal/semiconductor separation distance in a controlled fashion. A four-fold, separation distance-dependent enhancement in PL intensity is observed. To determine the source of the intensity enhancement, a detailed investigation of the system dynamics is performed. The individual contributions from enhancements in absorbance cross section, radiative decay rate, and quantum efficiency are thus identified. An analysis of the luminescence data indicates a local-field-enhanced quantum efficiency of 58% for nc-Si coupled to the nanoporous gold layer. Some additional details about the theoretical model used to deconvolute the ensemble measurements considered in Chapter 4 are elaborated upon in Appendix B

Building on the plasmon-enhanced PL results of Chapter 4, the nanoporous gold film is replaced in Chapter 5 by lithographically defined arrays of silver nanoparticles. In contrast to nanoporous gold, these arrays have very sharp plasmon resonance peaks, which are identified by transmission spectroscopy, and the resonances can be tuned with the particle diameter and the array pitch (center-to-center spacing). The coupled nc-Si/metal nanoparticle emission is measured by micro-photoluminescence spectroscopy, and the enhancement in PL intensity is found to have a spectral dependence: the frequency of maximum nc-Si PL enhancement coincides with the Ag nanoparticle array plasmon resonance frequency. Plasmon-enhanced photoluminescence is thus identified as a resonant process.

The physics that lead to resonantly enhanced PL from nc-Si coupled to Ag nanoparticle arrays are explored with full-field electromagnetic simulations in Chapter 6. We solve Maxwell's equations with finite-integral time domain computations to study the systems investigated experimentally in Chapter 5. Our computational treatment permits the examination of the exact system analyzed experimentally, i.e., reasonably closely coupled cylindrical particles. For metal particles of a given diameter arranged in arrays with a specific pitch, we find excellent agreement between the measured and calculated resonance frequencies. Furthermore, by integrating the enhanced electromagnetic field over the plane of the nc-Si emitters, we find that the calculated increase in field intensity corresponds well to the measured photoluminescence intensity enhancement.

In Chapter 7, the concept of plasmon-enhanced photoluminescence is extended to increased electroluminescence upon coupling to metal nanostructures. This is done by arranging the nc-Si emitters in a field-effect light-emitting diode. By pairing electrically pumped nc-Si with arrays of Ag nanoparticles, more than two-fold emission enhancements are measured, indicating that enhanced luminescence from nc-Si can be achieved for devices.

Finally, in Chapter 8, some general conclusions are drawn and we provide our perspective for the future of silicon microphotonics.

Chapter 2

Size-Dependent Electronic Surface States in Silicon Nanocrystals

2.1 Introduction

Silicon nanocrystals (nc-Si) with diameters, d, less than 5 nm exhibit room-temperature photoluminescence (PL)[4] due to the recombination of quantum confined excitons.[17] Detailed assessments of the relationship between Si nanocrystal size and band gap using self-consistent tight binding[21] and Quantum Monte Carlo (QMC)[22] methods predict a continuous increase in band gap with decreasing diameter in nanocrystals with diameters down to less than 1 nm. Experimental measurements have confirmed that the excitonic emission energy of nc-Si increases as the nanocrystal size decreases, but the increase is smaller than that expected theoretically.[19–21] This discrepancy suggests the presence of excitonic recombination through a localized electronic state whose energy level lies within the band gap of the smaller nanocrystals.

Silicon nanocrystals are typically embedded in silicon dioxide or surrounded by a native oxide layer, and theoretical models suggest that oxygen-related states at the nanocrystal surface can produce intragap energy levels.[21,22] Wolkin et al. theoretically evaluated the effect of a surface silicon-oxygen double bond (Si=O) on the electronic band structure of a Si nanocrystal.[21] Their semi-empirical computations predicted that the energy difference between the conduction and valence

bands would increase with nanocrystal diameter roughly according to d^{-2}, but their calculations also predicted that, for nanocrystals with $d \lesssim 3$ nm, the Si=O double bond would produce interface states that lie within the band gap, thereby reducing the energy of emitted photons. Puzder et al. used QMC calculations for small nanocrystals and interpolated to the bulk band gap with trends from density functional theory to confirm the semi-empirical results; they additionally showed that a variety of other surface terminations can produce deep-lying surface states in the Si nanocrystal band structure.[22] The emission energy of silicon nanocrystals is therefore predicted to depend strongly on the number and nature of bonds on the nanocrystal surface, and a better understanding of surface effects would permit band gap engineering. The additional localized states that arise in the presence of a Si=O double bond can also help to explain more recent reports of non-linear optical effects in silicon nanocrystal systems.[38,39] Explaining such non-linear effects requires invoking three- or four-level models for steady-state optical inversion; they cannot occur in the presence of silicon conduction and valence bands alone. We seek to test these interface-related excitonic recombination models experimentally, in particular those related to the presence of oxygen. In this chapter, we use photoluminescence (PL) spectroscopy to measure the exciton recombination energy of Si nanocrystals in a well-controlled size range, $d \sim 2.5{-}3.4$ nm ($400{-}1000$ Si atoms), with and without passivation by an oxygen environment.

2.2 Experimental

2.2.1 Preparation of Silicon Nanocrystals in SiO_2 Films and on Bulk Si Substrates

Nucleation and Growth of Nanocrystals

Ensembles of nc-Si were produced by implantation of 5-keV Si^+ ions to a fluence of 1.3×10^{16} cm^{-2} into 15 nm thick silicon dioxide films that were grown by thermal oxidation of lightly p-doped Si(100). According the Monte Carlo simulation program TRIM,[40] such implantations lead to a Gaussian depth distribution of silicon

in the SiO_2 matrix and produce a peak excess Si concentration of 14% at a depth of 10 nm. The implanted samples were annealed at 1100 °C for 5 min in Ar. Transmission electron microscopy has previously revealed that this process produces spherical nanocrystals,[41] and in the present chapter, we utilize atomic force microscopy (AFM) on HF-etched samples to characterize the heights (and therefore diameters) of the nanocrystals. The unetched samples were subsequently heated in a 10% H_2(g) in N_2(g) forming gas for 30 min at 450 °C to eliminate emission from dangling surface bonds and defect states in the SiO_2 matrix.[42]

Following this synthesis, the nanocrystal sizes could be controlled with high-temperature oxidation. For this purpose, the annealed, passivated samples were annealed in a flow of 99.998% O_2(g) at 800 °C. Previous reports have shown that this method can be used to reduce the mean Si nanocrystal diameter in order to tune the emission across the visible.[43]

Controlled Etching and Deposition

To access the surface of the silicon nanocrystals of all sizes, it was essential to remove them from the SiO_2 matrix in which they were formed. For this purpose, a controlled etching procedure was developed. First, the embedded nc-Si samples were cleaned by immersion in a solution of 5:1:1 H_2O:H_2O_2:NH_4OH at 80 °C for 10−20 min followed by a rinse in 18 MΩ·cm resistivity water. The nanocrystals were subsequently removed from the SiO_2 and deposited onto the silicon substrate with a 40 s chemical etch in buffered hydrofluoric acid (7.2% HF(aq), 36% NH_4F(aq) v/v). Care was taken to hold the samples horizontally. This etching procedure produced samples of Si nanocrystals physisorbed on a bulk Si wafer via van der Waals interactions. The etch rate of the buffered HF etchant was $\sim$ 1 nm/s. Since the bulk Si substrate serves as an etch stop when etching with HF, we chose to etch the 15 nm nc-Si-doped SiO_2 for a relatively long etch time of 22 s to ensure that the SiO_2 layer was completely removed.

In the present chapter, we focus on the effect of the surface oxidation of these nanocrystals on their optoelectronic properties. However, additional manipula-

tions of the freestanding nanocrystals, including chemical surface treatments and physical manipulations, were also performed, and these techniques are discussed in Appendix A.

2.2.2 Optoelectronic Characterization

Photoluminescence measurements were acquired from samples maintained in a chamber under a flow of 99.99% Ar(g) through a clear glass window. The samples were excited by the $\lambda_{ex} = 457.9$-nm line from an Ar^+ laser with a power density, P_{ex}, of 60 mW/mm^2, and emission was collected using a silicon charge-coupled device detector (sensitivity range 200−1100 nm) cooled with liquid nitrogen to $-132\,^{\circ}$C, in conjunction with a 27.5 cm focal length grating spectrograph. A 510 nm long-pass filter in front of the entrance slit was used to cut off scattered laser illumination. PL spectra were obtained with a 60 s integration, and the spectrum of a clean silicon wafer taken under identical alignment conditions and excitation power was used to remove dark count signatures. The decay dynamics were probed by modulating the photoexcitation source with an acousto-optic modulator at 250 Hz, and recording the PL with a GaAs photomultiplier tube (PMT) coupled to a multichannel photon counting system. This system's time resolution was < 50 ns.

2.2.3 Physical Analysis of Silicon Nanocrystals

The freestanding Si nanocrystals on Si(100) substrates discussed in this chapter were suitable candidates for standard surface science analysis techniques. We relied on atomic force microscopy (AFM) to verify the presence of Si nanocrystals on the substrate, as well as to measure the nanocrystals' heights and determine a lower limit for the coverage of nanocrystals. Since a traditional contact mode AFM tip will pick up and move small nanoparticles, we utilized non-contact mode AFM, with a cantilever resonant frequency of ~ 300 kHz, to scan our samples. Standard gold-coated tips with a radius of $\lesssim 10$ nm were used, so a pair of nanocrystals in close proximity to one another could not be resolved laterally. Still, the instrument is accurate to $\pm$ 1 Å in the vertical direction; this technique could therefore

precisely quantify the nanocrystal heights, and hence the diameters, since these nanocrystals have been previously determined to be approximately spherical.[41]

The samples were also characterized by UHV scanning tunneling microscopy (STM). This provided a means to analyze the nanorystals in an oxygen-free environment, as the pressure was maintained at 1×10^{-10} Torr. STM also gives a greater lateral resolution than does AFM, ± 1 nm rather than ± 10 nm; this technique is therefore a better method for measuring surface coverage.

To characterize the chemical nature of the samples in this chapter, we used X-ray photoelectron spectroscopy (XPS) with an M-Probe surface spectrometer (VG Instruments). The sample was excited by monochromatic (1486.6 eV) Al Kα X-rays incident at $55\,^\circ$ from the normal focused to a beam spot of 800 μm $\times$1500 μm. The emitted photoelectrons were collected by a hemisphere analyzer at a takeoff angle of $55\,^\circ$ from the normal. The system pressure was $\leq 1 \times 10^{-9}$ Torr. Measured binding electron energies were referenced to the Fermi level of the spectrometer.

Further characterization was performed using reflection high-energy electron diffraction (RHEED). In this technique, 25.0-keV electrons are incident on the sample at a glancing angle ($\sim 1{-}5\,^\circ$), and their diffraction pattern upon interaction with the surface is recorded.

2.3 Results and Discussion

2.3.1 Embedded Silicon Nanocrystals

Figure 2.1(a) shows the room-temperature PL spectrum of the prepared nc-Si ensemble. The large spectral width can be ascribed to the distribution of nanocrystal sizes resulting from the nucleation and growth process, as well as to the significant (50$-$100 nm) linewidths that are known to characterize even single silicon nanocrystals at room temperature.[6] The peak PL energy, E_{max}, of 1.60 eV in Fig. 2.1(a), when compared with calculations by Puzder et al.,[22] corresponds to a mean nanocrystal diameter, d_0, of 3.4 nm. To obtain nanocrystal ensembles with slightly

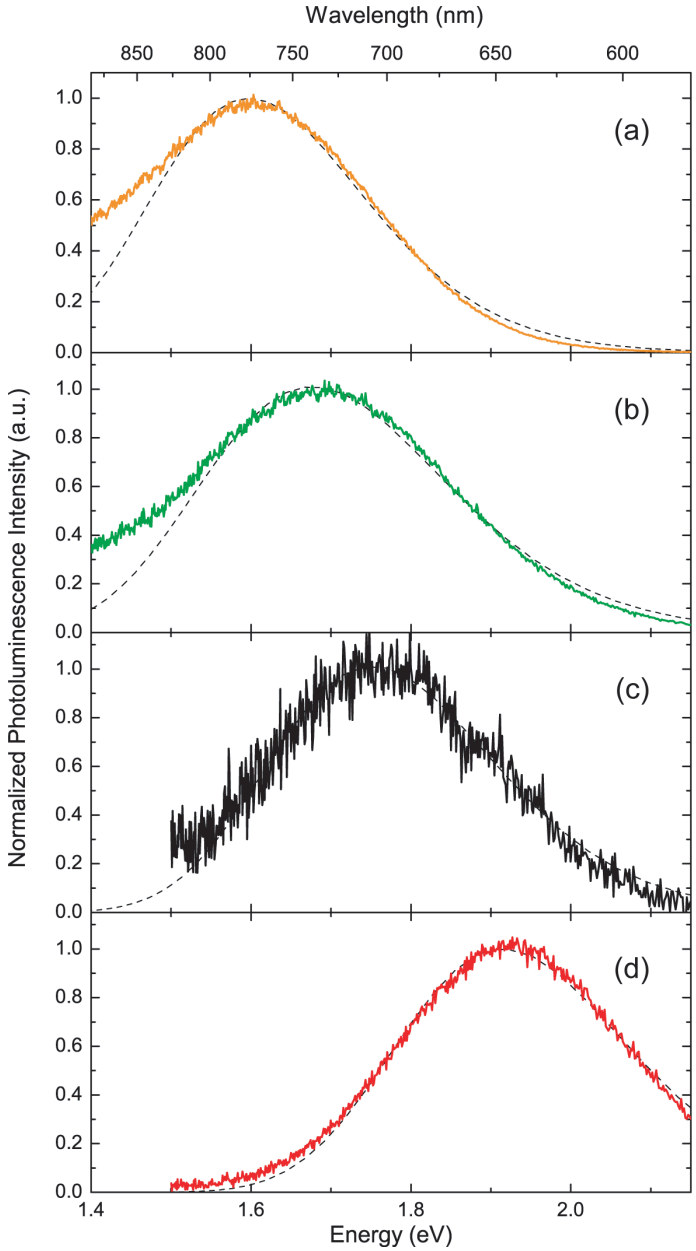

Figure 2.1: Normalized room temperature photoluminescence measurements on nanocrystal samples embedded in 15 nm SiO_2 [panels (a) and (b)], and immediately after etching the SiO_2 [panels (c) and (d)]. Panels (a), (b), (c), and (d) are the spectra of Si nanocrystal ensembles with average diameter, d_0, of 3.4, 3.3, 3.2, and 2.9 nm, respectively. The absolute intensity of the emission in (a) and (b) is 20 times that in (c) and (d). The dashed lines are fits of the data to Gaussian distributions. $\lambda_{ex} = 457.9$ nm, $P_{ex} = 60$ mW/mm^2.

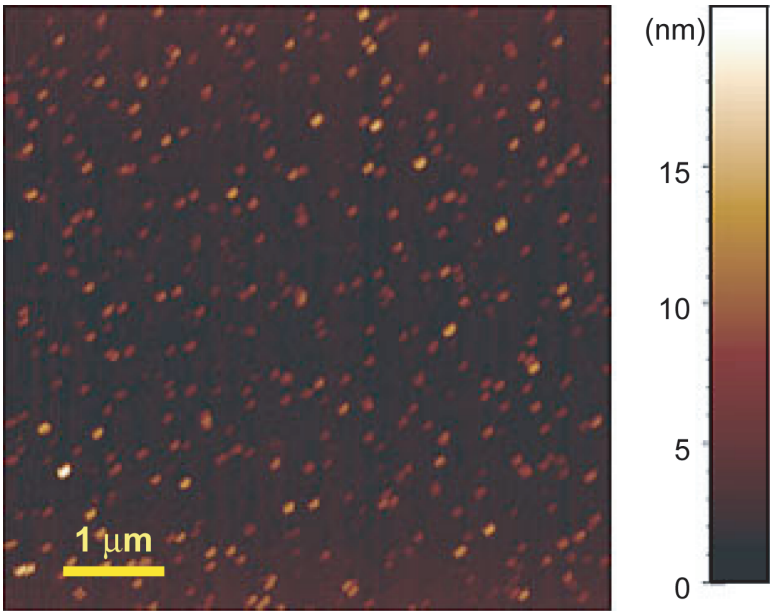

Figure 2.2: 6 μm $\times$ 6 μm non-contact atomic force microscope image of the d_0 = 3.2 nm etched sample in Fig. 2.1(c).

smaller mean diameters, the SiO_2 film containing the embedded nanocrystals was annealed for 20 min at 800 °C under O_2. The resulting PL spectrum (Fig. 2.1(b)) was blue-shifted by 80 meV, and the corresponding diameter is 3.3 nm.[22]

2.3.2 Microscopy and Spectroscopy of Etched Silicon Nanocrystals

To obtain even smaller nanocrystals and to isolate them from the SiO_2 matrix, the controlled etching procedure described in Section 2.2.1 was applied. Non-contact atomic force microscopy (AFM) was used to examine these samples; this technique can provide information about the nanocrystal diameters by measuring their heights, and it can also give a lower limit on surface coverage. The AFM image in Fig. 2.2 shows a scan of the d_0 = 3.2 nm sample characterized in Fig. 2.1(c), and indicates a coverage of $\geq$ 30 nanocrystals per μm^2 and average nanocrystal diameter of 2−4 nm.

The same samples were investigated by scanning tunneling microscopy (STM). The STM image in Fig. 2.3(a) shows a 50 nm $\times$ 50 nm region of nc-Si on a

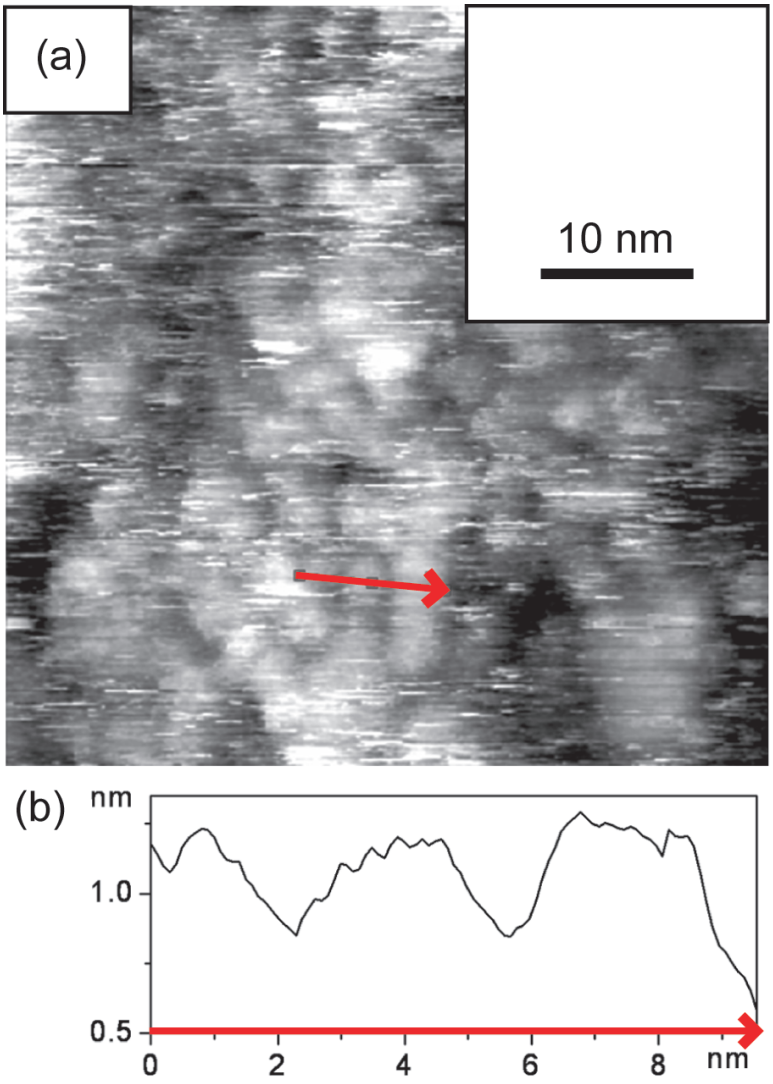

Figure 2.3: (a) 50 nm × 50 nm scanning tunneling microscope image of the d_0 = 3.2 nm etched sample. (b) Line profile along the cut indicated by the red arrow in panel (a). After Fig. 2.6 of the thesis of Tao Feng, California Institute of Technology.[44]

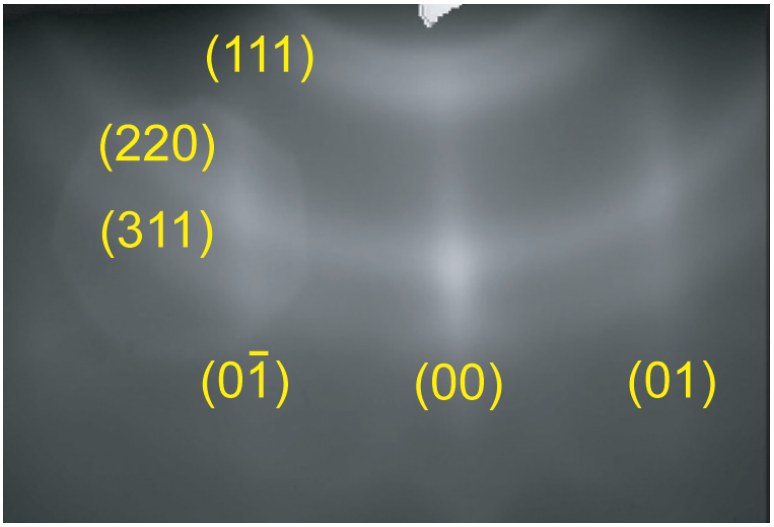

Figure 2.4: Reflection high-energy diffraction (RHEED) pattern of randomly oriented Si nanocrystals on a Si(100) substrate. The concentric circles, labeled on the left, correspond to diffractions from the nc-Si, and the vertical streaks, labeled at the bottom, correspond to diffractions from the Si(100).

Si substrate. This figure shows a dense distribution of nc-Si with a coverage of 10^{11}–10^{12} cm^{-2}. The line scan in Fig 2.3(b) is the height profile along the cut indicated by the red arrow in Fig 2.3(a). STM can discern individual nanocrystals, even when these have heights less than 1 nm.

Reflection high-energy electron diffraction (RHEED) was used to verify that the small particles observed on the surface by AFM were indeed silicon nanocrystals. Electron diffraction can distinguish between single-crystal and polycrystalline materials; in the present experiments, we expect the collection of randomly oriented nc-Si to look like a polycrystalline silicon surface. We therefore anticipate that the sparse layer of randomly oriented silicon nanocrystals on a Si(100) substrate will have a diffraction pattern in RHEED that is a combination of polycrystalline rings and silicon(100) lines. Figure 2.4 shows the result for a RHEED measurement of diffraction along the (110) direction. In this figure, the three concentric rings are the (111), (220), and (311) diffractions of the randomly oriented silicon nanocrystals, and the three vertical streaks are the $(0\bar{1})$, (00), and (01) lines from the Si(100) substrate.

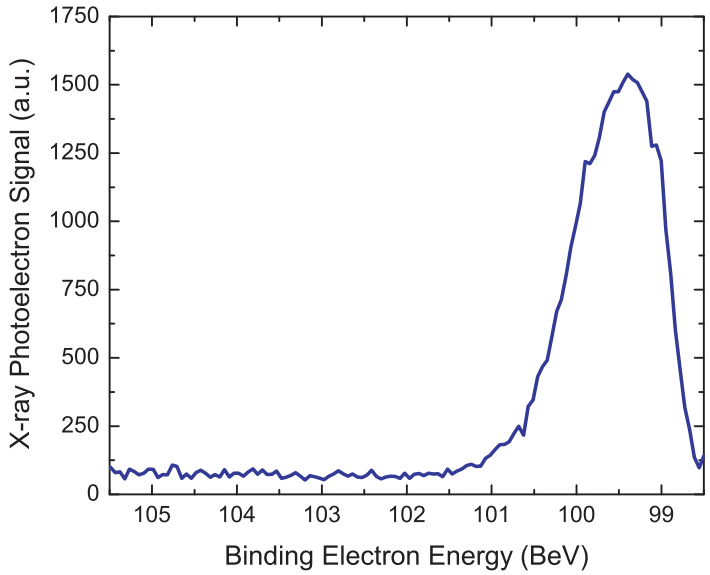

Figure 2.5: X-ray photoelectron spectrum for the Si 2p region of a freshly etched sample of Si nanocrystals on an Si(100) substrate showing a single peak characteristic of the Si^0 oxidation state at 99.5 BeV and no evidence of a silicon oxide signal at higher binding energies.

Upon removal from the buffered HF etching solution, the Si substrates with Si nanocrystals were examined by X-ray photoelectron spectroscopy (XPS). The XP spectrum of the Si (2p) region of a typical freshly etched sample is shown in Fig. 2.5. In this region, the Si^0 peak of bulk Si or Si-H occurs at 99.3 BeV, while silicon oxide and suboxide peaks show in the range of 101−105 BeV.[45] The spectrum in Fig. 2.5, which contains a single peak at 99.5 BeV, demonstrates that the nanocrystals and the Si surface were oxide-free to the limit of the instrument resolution (i.e., less than 5% of a monolayer of oxide), implying that the nanocrystals' surfaces were hydrogen-terminated. To prevent oxidation, the nanocrystals were stored under a flow of 99.99% Ar. When left in ambient air, the nanocrystal surfaces oxidized on a scale of minutes, as determined by XPS.

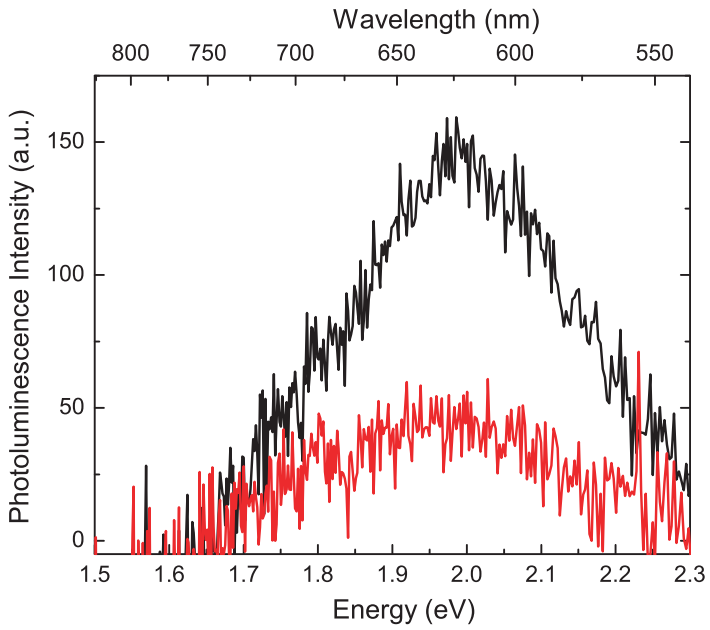

Figure 2.6: Photoluminescence spectra of a freshly etched sample [black curve] and the same sample after 15 min of irradiation in air by the PL excitation source [red curve]. Photobleaching in air causes a 3.2× decrease in the signal intensity. $\lambda_{ex} = 457.9$ nm, $P_{ex} = 60$ mW/mm^2.

2.3.3 Photoluminescence Spectroscopy of Etched Silicon Nanocrystals

After etching, the intensity-normalized PL spectra of both samples (Figs. 2.1(c) and (d)) exhibited a 140−150 meV blue shift relative to the spectra of the corresponding embedded samples from which they were etched (Figs. 2.1(a) and (b)). The corresponding average nanocrystal diameters are $d_0 = 3.2$ nm (Fig. 2.1(c)) and $d_0 = 2.9$ nm (Fig. 2.1(d)). After etching, the widths of the PL spectra remained in the range of 340−360 meV, indicating that the size distribution remained unchanged from the embedded samples. The peaks were symmetric for all of the measurements discussed in this paper. The reduction in diameter by 0.2−0.4 nm produced by HF etching corresponds to the conversion of approximately two monolayers of Si (one on each side of the nanocrystal) to silicon hydrides as a result of the etch process.

The absolute PL intensity for the etched samples was reduced by a factor of

$\sim$ 20 relative to that of their respective embedded precursors, which can be explained by a reduction in nanocrystal coverage during this process. After etching, the average nanocrystal coverage, estimated from the implanted Si fluence, average nanocrystal diameter, and PL intensity decrease was in the range of $10^{11}-10^{12}$ cm^{-2}, i.e., one nanocrystal per $10-100$ nm^2 of substrate area. This upper limit is consistent with the lower limit for coverage obtained from the AFM image in Fig. 2.2. The intensity stayed constant with time in air after etching, but decreased upon photoexcitation in air. Figure 2.6 shows the PL intensity from a typical sample left in air immediately (black curve) and after 15 min of photoexcitation in air ambient (red curve). The emission intensity decreases three-fold. All subsequent PL measurements were therefore taken through the window of a chamber in which the sample was stored under a flow of 99.99% Ar to prevent photobleaching.

To verify that the emission from the etched samples was excitonic in nature, the photoluminescence decay lifetime was determined with time-resolved PL measurements. The decay trace of a typical sample of etched nanocrystals, monitored at the emission wavelength of 775 $\pm$ 20 nm, is shown in Fig. 2.7. The decay of silicon nanocrystal emission intensity, $I_{PL}(t)$, is fitted with a stretched exponential function,

$$I_{PL}(t) = I_{PL,0} \exp\left[-(t/\tau)^{\beta}\right] \tag{2.1}$$

where $I_{PL,0}$ is the initial PL intensity, t is the time, τ is the experimental decay lifetime, and β is a parameter between 0 and 1 ($\beta = 1$ in the case of single exponential decay) that depends on a host of factors including interactions between neighboring nanocrystals, the presence of defect states, and intermittency in the emission. The curve in Fig. 2.7 is characterized by $\beta = 0.8$ and a decay time of $\tau = 16$ μs that is consistent with excitonic emission from Si nanocrystals.[46,47]

2.3.4 Effect of Oxidation on the Emission of Silicon Nanocrystals

To examine the effect of oxygen on nc-Si emission, samples were subjected to short periods (30 s) of *in situ* oxidation in air ($21-22\,^{\circ}C$, $30-35\%$ humidity). To

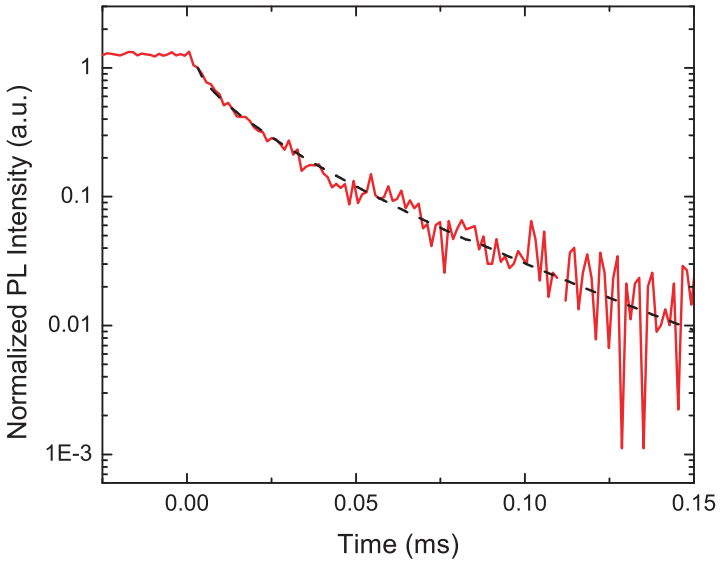

Figure 2.7: Time-resolved photoluminescence measurement on a freshly etched Si nanocrystal sample in Ar. The excitation source is turned off at time, $t = 0$, with a response time of < 50 ns. The dashed line is a fit to stretched exponential decay, as described in Eq. (2.1). $\lambda_{ex} = 457.9$ nm, $\lambda_{det} = 775 \pm 20$ nm.

minimize pump-induced photo-oxidation, the nanocrystal oxidation was performed in the dark. After each oxidation step, the sample chamber was refilled with Ar, and PL data were recorded. Before any exposure to air, the $d_0 = 3.2$ nm and $d_0 = 2.9$ nm samples in Figs. 2.8(a) and (b) have the spectra shown in panels Figs. 2.1(c) and (d), respectively; here, d_0 is the initial mean diameter of the particles as deduced from the relationship between the PL energy and the QMC theory results in Ref. 22. Figures 2.8(a) and (b) depict the evolution of E_{max} with oxidation time for these two samples, as determined from Gaussian fits to the PL spectra.

To study the excitonic recombination energy for even smaller nanocrystal sizes, the sample with $d_0 = 3.2$ nm of Fig. 2.8(a) was reoxidized in ambient air and exposed to a second buffered HF etch. The PL spectrum and intensity of this twice-etched sample was less spatially homogenous relative to the samples that had only been etched once, presumably resulting from etch-induced nanocrystal size distribution inhomogeneities. By selecting a particular location on the sample, regions with different PL peak energies and thus different inferred mean nanocrys-

tal diameters could be probed. The spectra labeled $d_0 = 2.8$ nm and $d_0 = 2.5$ nm in Figs. 2.8(c) and (d), respectively, were identified and probed using this approach. Care was taken to focus the exciting beam on a fixed spot throughout each experiment so that any changes in luminescence intensity for a single experiment were nominally due solely to changes within a given nanocrystal ensemble. The error bars in Figs. 2.8(c) and (d) are larger than those in 2.8(a) and (b) due to a significant decrease in emission intensity for these twice-etched samples.

For the samples in Figs. 2.8(a) and (b), as the oxidation time increased, the emission energy increased monotonically, in accord with expectations for a concomitant decrease in nanocrystal diameter. In contrast, for the two nanocrystal ensembles in Figs. 2.8(c) and (d), where d_0 is smaller, the emission energy initially increased, but then began to decrease after ~ 7 min of oxidation.

The solid line that appears in both panels of Fig. 2.9 shows the predictions of the QMC model of Puzder et al. for the emission energy of completely hydrogen-terminated Si nanocrystals as a function of their diameter.[22] For nanocrystals with $d \gtrsim 3$ nm, this model predicts that surface states should have little effect on the excitonic recombination energy, and consequently, in this size regime, both hydrogen- and oxide-terminated nanocrystals should exhibit PL emission at their band gap energy. The monotonically increasing emission energies upon oxidation in Figs. 2.8(a) and (b) indicate that the $d_0 = 3.2$ nm and 2.9 nm samples fall in this size regime. The QMC model was therefore used in conjunction with the PL data of Figs. 2.8(a) and (b) to evaluate the nanocrystal diameter at each oxidation time by constraining the observed E_{max} (from Figs. 2.8(a) and (b)) to the computational trend line of Fig. 2.9. The resulting deduced decrease in nanocrystal diameter, Δd, as a function of air exposure time, t, is plotted for the $d_0 = 3.2$ nm and 2.9 nm samples in Fig. 2.10. The data are well-fitted by the logarithmic function,

$$\Delta d\,[\text{nm}] = 0.037 \cdot \ln\left(t\,[\text{min}] - 1.7\right) \tag{2.2}$$

where $t > 1.7$ min. This logarithmic relationship is in accord with experiments on

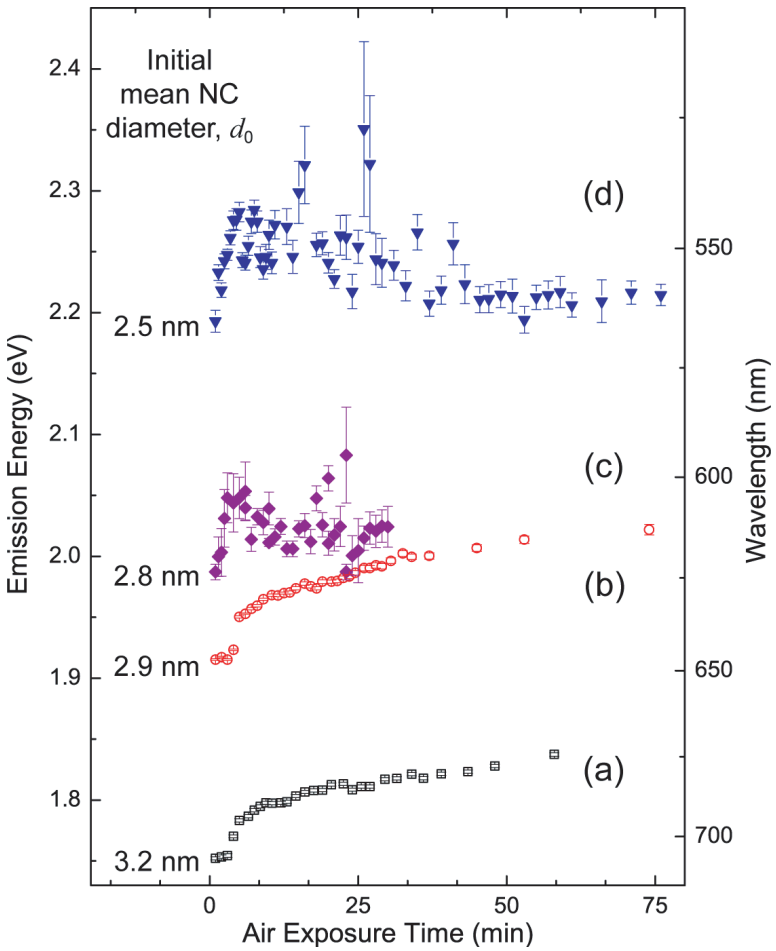

Figure 2.8: Time evolution of E_{max} over the course of ambient reoxidation. The samples were etched at $t = 0$ min and transferred to an Ar flow chamber within less than 1 min, where they remained during PL measurements; excitation and collection were done through a fused silica window. $\lambda_{ex} = 457.9$ nm, $P_{ex} = 60$ mW/mm^2.

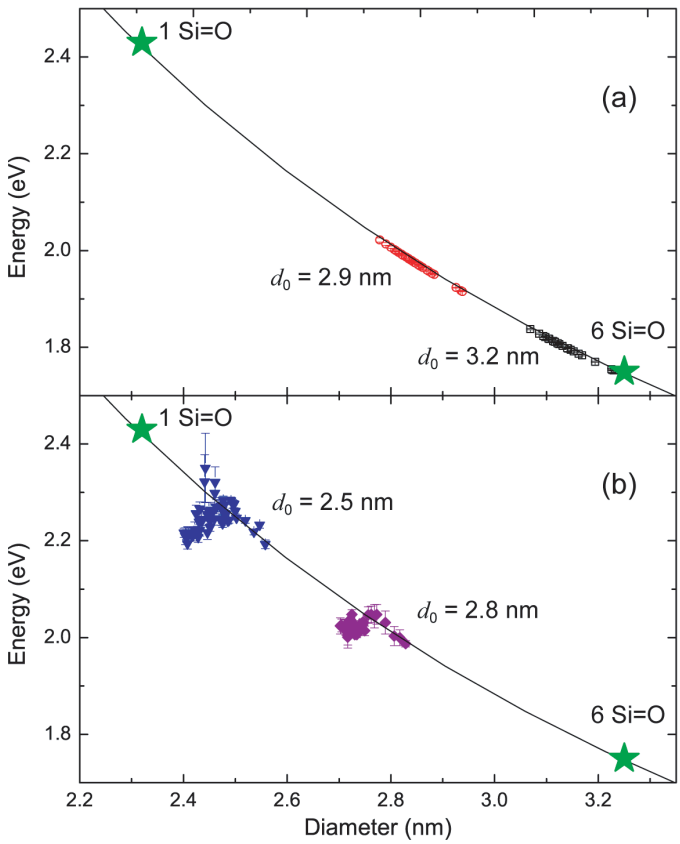

Figure 2.9: Fit of data from Fig. 2.8 to the QMC computations of Ref. 22 (solid line) for samples of Si nanocrystals with 2.5−3.2 nm initial diameters, d_0. (a) The nanocrystal emission energies are constrained to the computed curve for the emission energy of a silicon nanocrystal in the absence of surface states. (b) The nanocrystal samples air exposure time is converted to size according to the relationship determined in Fig. 2.10. The stars represent the sizes at which, according to calculations, one and six Si=O double bonds, respectively, are required to introduce surface states.

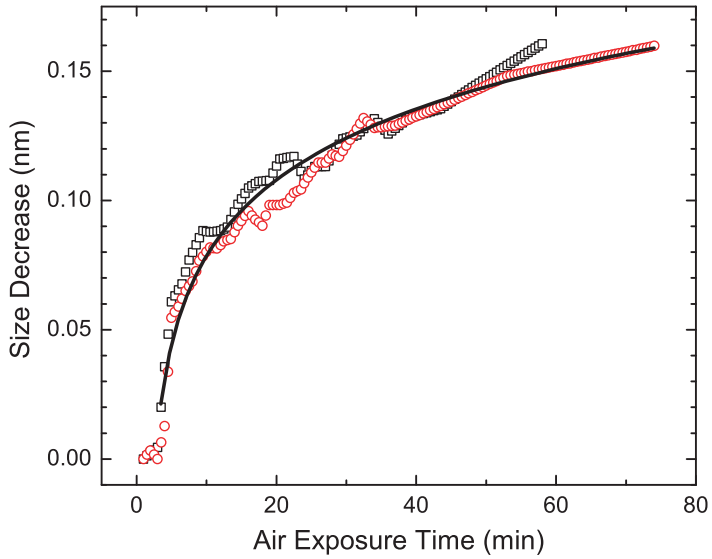

Figure 2.10: Relationship between size decrease and air exposure time derived from comparing the air exposure time in Figs. 2.8(a) and (b) to the sizes in Fig. 2.9(a). The black squares and red circles correspond to the $d_0 = 3.2$ and 2.9 nm nc-Si in Figs. 2.8(a) and (b), respectively. The solid line shows a fit of the size decrease, Δd, to the logarithmic function, $\Delta d\,[\mathrm{nm}] = 0.037 \cdot \ln(t\,[\mathrm{min}] - 1.70)$.

the time-dependence of the room temperature growth of thin native oxide films on bulk Si surfaces.[48]

The emission energies of the smaller-diameter nanocrystals clearly cannot be constrained to the calculated curve of Fig. 2.9, because the PL was red-shifted as the oxidation time increased (and presumably as particle size decreased). Instead, since the samples in Figs. 2.8(c) and (d) were oxidized in the same way as the samples in Figs. 2.8(a) and (b), (i.e., with 30 s intervals of exposure to air), all samples were assumed to have the same logarithmic oxidation kinetics. The times in Fig. 2.8(c) and (d) could therefore be converted to the diameters in Fig. 2.9(b). This latter figure shows that, for the initial period of oxidation, the observed PL energies for these smaller-diameter nanocrystals followed the calculated curve for band-to-band emission, but once $\sim$ 0.1 nm of Si had been converted to $\sim$ 0.3 monolayers of silicon oxide, the emission energies were red-shifted below the expected band gap. These data are consistent with the formation of an (oxygen-related) trap state in the Si nanocrystals having $d_0 < 2.8$ nm.

According to Puzder et al. and Wolkin et al.,[21,22] below a certain diameter, a double-bonded surface group will introduce a deep-lying state that reduces the exciton recombination energy. One candidate for the oxygen-related state indicated by the data of Figs. 2.8 and 2.9 is therefore the Si=O double bond. Though there is a significant barrier to making this bond, the formation of Si=O bonds has been calculated to occur on a silicon surface by the photoexcitation of Si-OH (an expected species due to water vapor in the air), with a barrier to formation of ~ 2.4 eV.[49] The 2.7 eV photons used for luminescence measurements could drive such a reaction process. The Si=O double bond has also been observed by Fourier transform infrared spectroscopy as a metastable transient.[50] Indeed, observation of PL does not require the luminescent state to be long-lived, since exciton lifetimes in Si nanocrystals at room temperature are on the order of tens of microseconds.[43]

Finally, we note that Puzder et al. have shown that while one Si=O bond will produce a defect level only for nanocrystal sizes below ~ 2.4 nm, multiple Si=O bonds will lead to the emergence of deep-lying states for larger nanocrystal sizes.[22] The star symbols on the drawn line in both panels of Fig. 2.9 indicate the minimum diameters at which one or six Si=O bonds are expected theoretically to produce a deep-lying state. The observed trap-related red shift in the present chapter occurs between these two extrema; it can therefore be theoretically explained by the binding of only a small number of double-bonded surface species.

2.4 Conclusions

In conclusion, the PL peak emission energy of Si nanocrystals with $d_0 \sim 2.9-3.4$ nm shows an increase in excitonic recombination energy upon oxidation-induced size reductions, in agreement with calculations. For smaller nanocrystals ($d_0 \sim 2.5-2.8$ nm), oxidation leads to an initial emission blue shift, but after the growth of ~ 0.3 monolayers of native oxide, a red shift is observed. The latter is consistent with the formation of a theoretically predicted oxygen-related intraband surface state. Selective etching of Si nanocrystal/SiO_2 composites leads to the formation of

controlled ensembles of isolated nanocrystals that display oxidation kinetics similar to those of planar surfaces, making them available for future single-nanocrystal studies.

Chapter 3

Plasmonic Enhancements of Semiconductor Nanocrystal Emission

3.1 Introduction

The optical properties of small noble metal particles have attracted the attention of physicists for hundreds of years.[51,52] Silver and gold nanoparticles interact very strongly with incident visible illumination, and their absorption spectra demonstrate clear differences from their bulk counterparts, including enhanced absorption and spectral changes. These extraordinary properties can be explained by the excitation of coherent free electron oscillations, or particle surface plasmon polaritons, in the nanoparticles. As a result of the high polarizability induced by such modes, a strong electric field develops about the particle surface. This enhanced local field has been exploited for many diverse applications, among them, surface-enhanced spectroscopy,[32,34,53,54] subwavelength optical propagation,[55] higher harmonic generation,[56] and targeted surface photochemistry.[57]

Studies of silicon nanocrystal (nc-Si) luminescence have long been plagued by the weak emission intensity resulting from the low radiative recombination rates of these emitters. In the remainder of this thesis, we therefore strive to take advantage of the enhanced local field about metal nanostructures for the novel application of engineering the decay rate and emission intensity of silicon nanocrystals. Motivated by the desire to enhance and manipulate the photoluminescence (PL) and

electroluminescence (EL) of silicon nanocrystals, in the present chapter, we introduce the concept of plasmon-enhanced quantum dot emission. In particular, we explore the prediction of enhanced dipole emission in the vicinity of a metal nanoparticle, we discuss the nature of particle plasmon modes, and we present calculations that describe the enhanced local field about a resonantly excited metal nanostructure.

3.2 Plasmon-Enhanced Emission

3.2.1 Theoretical Predictions of Enhanced Emission

Thirty years ago, spectroscopists remarked on the remarkable sensitivity of Raman spectroscopy when studying molecules absorbed on metal surfaces.[32,53,54] Since that time, enhancement factors up to $10^{14}-10^{15}$ have been reported in the literature, making SERS a convenient tool even for delicate measurements like single-molecule spectroscopy, and surface-enhanced Raman spectroscopy (SERS) has become an established analytical technique.[58] Raman spectroscopy, a technique that detects vibrational modes through inelastic scattering events, is strongly non-linear with respect to the electric field strength of the pump beam. Though the interpretation of the enhancement effect remains somewhat controversial, the bulk of the surface-induced enhancement observed in SERS is generally attributed to an increase in the local electromagnetic field.[33,59,60] Accordingly, this large enhancement effect has generated a large body of interest in utilizing the powers of surface enhancement for other spectroscopic applications that might take advantage of the increases in absorption and luminescence that are manifestations of the enhanced local electromagnetic field about rough and nanostructured metal surfaces.[34,61]

In the present thesis, we focus on the potential that exists for using the enhanced local field about a nanostructured metal to increase the luminescence of an emitter. The emission of a dipole in the vicinity of a metal particle has been treated theoretically in many works.[61–69] The majority of these studies focus on

the problem of a dye molecule emitting in proximity to a spherical or ellipsoidal metal nanoparticle, but the theory is quite general and thus can be easily extended to the case of a semiconductor nanocrystal emitter near an arbitrary metal nanostructure. Here, we make use of the formalism of Gersten and Nitzan,[61] which has been extended by Wokaun et al. to address fully radiationless energy transfer quenching,[62] and which has been restated more recently by Kümmerlen et al.[63]

An emitter in the near field of an excited metal nanoparticle will experience an enhanced local field, $E(\omega) = L(\omega)E_0(\omega)$, where $L(\omega)$ is the frequency-dependent field enhancement. The origin and properties of such enhanced electromagnetic fields will be addressed in Sections 3.3 and 3.4, and at the present, we simply remark that $L(\omega)$ is a function that depends on the materials properties of the metal particle and its environment, as well as on the specific size and shape of the metal nanostructure and the distance between the emitter and the metal surface.

Due to the local-field enhancement, the luminescence of an emitter will be modified upon its coupling to an excited metal nanoparticle, and the PL intensity enhancement, η_{PL}, of this optical emitter is given by

$$\begin{aligned} \eta_{PL}(\omega_{exc}, \omega_{PL}) &= \eta_{\sigma}(\omega_{exc})\eta_{Q}(\omega_{PL}) \\ &= |L(\omega_{exc})|^2 \, \eta_{Q}(\omega_{PL}) \end{aligned} \tag{3.1}$$

Here, the first factor reflects increases in PL intensity due to enhanced absorption, η_{σ}, at the excitation frequency, ω_{exc}, and the second factor is the enhancement in radiative quantum efficiency, η_{Q}; this latter term describes the variations in emission resulting from changes in the radiative and non-radiative decay dynamics at the emission frequency, ω_{PL}.

The radiative quantum efficiency of an emitter is the ratio of the radiative decay rate to the total decay rate along radiative and non-radiative pathways. In the absence of the metal nanoparticle, the quantum efficiency, Q_0, is then given by

$$Q_0 = \frac{\Gamma_{r,0}}{\Gamma_{r,0} + \Gamma_{nr,0}} \tag{3.2}$$

where $\Gamma_{r,0}$ and $\Gamma_{nr,0}$ are the radiative and non-radiative decay rates of the emitter in free space. Upon coupling to the metal nanoparticle, these rates are increased by $\Delta\Gamma_r$ and $\Delta\Gamma_{nr}$, respectively, and the quantum efficiency, Q', becomes

$$Q' = \frac{\Gamma_{r,0} + \Delta\Gamma_r}{(\Gamma_{r,0} + \Delta\Gamma_r) + (\Gamma_{nr,0} + \Delta\Gamma_{nr})} \tag{3.3}$$

The quantum efficiency enhancement is the ratio, $\eta_Q = Q'/Q_0$.

As discussed in great depth by Gersten and Nitzan, the radiative decay rate of a dipole emitter near a metal nanoparticle is a complex function of the nanoparticle geometry, the position of the dipole relative to the nanoparticle, and the dielectric environment.[61] However, Kümmerlen et al. point out that for particles with dimensions that are small relative to the wavelength, only the dipolar plasmon mode contributes significantly to emission. Therefore, since the dipole moment of the coupled nanoparticle/emitter system, emitting at frequency ω_{PL}, is proportional to $L(\omega_{PL})$, the radiative decay rate of the coupled system is proportional to the square of this enhancement factor, i.e.,[63]

$$\Gamma_{r,0} + \Delta\Gamma_r = \Gamma_{r,0} \left|L(\omega_{PL})\right|^2 \tag{3.4}$$

In determining the coupled system radiative rate with Eq. (3.4), the enhancement factor, L, is evaluated at the emission frequency, ω_{PL}.

Unfortunately, to experience high local fields, the emitter must be in close proximity to the metal. As a result, in addition to the beneficial dipole-dipole coupling effect that results in an enhanced radiative emission rate, the emitter is also affected by the presence of higher-order modes, which are non-radiative. Such radiationless energy transfers from the excited emitter molecule to higher-order surface plasmon modes in the metal lead to an increase in the non-radiative decay rate of the coupled system.[62]

For the case of an emitter very close to a metal nanoparticle, the metal surface can be approximated as an infinite plane,[63] and we can simplify our treatment of the radiationless energy transfer process by considering it equivalent to the

extensively explored case of the damping of an emitter near a planar metal film.[70] In this small separation-distance limit, the change in non-radiative decay rate is found to depend on the emitter/surface separation distance, d, and the free emitter radiative rate, i.e.,[63]

$$\Delta\Gamma_{nr} = A\frac{\Gamma_{r,0}}{d^3} \tag{3.5}$$

where the amplitude, A, depends on the dielectric functions of the metal and the embedding medium.

Given the functional forms of $\Delta\Gamma_r$ and $\Delta\Gamma_{nr}$ in Eqs. (3.4) and (3.5), the quantum efficiency of the coupled system in Eq. (3.3) becomes

$$Q' = \frac{\Gamma_{r,0}\left|L(\omega_{PL})\right|^2}{\Gamma_{r,0}\left|L(\omega_{PL})\right|^2 + \Gamma_{r,0}Ad^{-3} + \Gamma_{nr,0}} \tag{3.6}$$

The quantum efficiency enhancement, $\eta_Q = Q'/Q_0$, is then

$$\eta_Q = \frac{\left|L(\omega_{PL})\right|^2}{Q_0\left|L(\omega_{PL})\right|^2 + Q_0Ad^{-3} + (1-Q_0)} \tag{3.7}$$

and the total emission enhancement in Eq. (3.1) is expressed by

$$\eta_{PL} = \left|L(\omega_{exc})\right|^2 \cdot \frac{\left|L(\omega_{PL})\right|^2}{Q_0\left|L(\omega_{PL})\right|^2 + Q_0Ad^{-3} + (1-Q_0)} \tag{3.8}$$

3.2.2 Experimental Observations of Plasmon-Enhanced Emission

By coupling an emitter to a field that is locally enhanced at the excitation or emission frequency, emitter enhancements are predicted according to Eq. (3.8). Such effects have been observed in many different systems. The first experimental evidence of plasmon-enhanced emission was seen in 1980 by Glass et al., who examined changes in absorption and emission from the dyes rhodamine B and nile blue adsorbed on films of Ag nanoparticles.[34] This work highlighted many of the important features of the plasmon enhancement effect. Firstly, the dye absorption spectrum was greatly enhanced upon coupling to the metal particles. Secondly, when separated by a 3 nm polymethyl methacrylate (PMMA) spacer layer, the

dye absorbance was still enhanced, but much less so. Thirdly, the fluorescence intensities of each dye were enhanced in the presence of the metal nanoparticles, and these intensities reached their maximum values when the Ag particle plasmon resonance occured at the absorption wavelength of each specific dye. Finally, the luminescence from the same dye molecules adsorbed on smooth, continuous metal surfaces was heavily quenched.[34]

Many other studies of plasmon-coupled dye emission followed, including some more recent single-molecule investigations.[71–74] Through these studies, it has become clear that, as predicted in Section 3.2.1, a competition between enhancing (radiative coupling) and quenching (non-radiative coupling) accurately describes the observed electromagnetic effects. At very small metal/dye separation distances, fluorescence is quenched, but at some slightly larger optimal distance, radiative coupling becomes dominant and fluorescence is enhanced.[74]

The plasmon-enhanced emission effect is not limited to the emission of dyes, and indeed, coupling to metal surface plasmons has shown enhancements in the radiative decay rates and emission intensities of semiconductor quantum wells.[37,75–77] More recently, in part spurred by reports of enhanced SERS signals for CdS quantum dots that are coated by Ag nanoparticles,[78] investigators have turned their attention to plasmon-enhanced photoluminescence from semiconductor nanocrystals. In 2002, Kulakovich et al. observed distance-dependent enhancement and quenching of the PL emission from CdSe/ZnS core/shell nanocrystals coupled to Au nanoparticles,[36] and, in that same year, Shimizu et al. observed enhanced PL emission from CdSe/ZnS core/shell nanocrystals on a rough gold film, concurrent with a $10^3\times$ enhancement in emission rate.[35] It is therefore clear that this scheme has great potential for enhancing the emission of silicon nanocrystals.

3.3 Local-Field Enhancements about Metal Nanostructures

3.3.1 Plasmon Modes in Small Metal Nanoparticles

Illumination incident on noble-metal nanoparticles interacts strongly with them by inducing coherent oscillations of the free electrons. These collective bound modes are termed surface plasmon polaritons, and at the plasmon resonance frequency, ω_p, the coherent response is exactly $\pi/2$ out of phase with the applied external field, and a large polarization is induced by surface charges. As the resonant field builds up in the particle, a strong dipolar local field evolves in the vicinity of the particle.[79] It is this enhanced local field to which the electromagnetic enhancement effects described in Section 3.2 are attributed. The field enhancement is strongly tied to the plasmon mode, and the local field is therefore strongest at the plasmon resonance frequency.

In a dielectric environment with dielectric constant, ε_m, the induced polarization, $\mathbf{p}$, is proportional to the applied field, $\mathbf{E_0}$, i.e.,

$$\mathbf{p} = \varepsilon_m \alpha \mathbf{E_0} \tag{3.9}$$

The constant of proportionality, α, is a measure of the ease with which the metal may be polarized. In the electrostatic limit of a very small spherical metal nanoparticle, with radius, r, much smaller than the radiation wavelength, λ, the polarizability, α, is given by[80]

$$\alpha(\omega) = 4\pi r^3 \frac{\varepsilon_1(\omega) - \varepsilon_m}{\varepsilon_1(w) + 2\varepsilon_m} \tag{3.10}$$

Here, $\varepsilon_1(\omega)$ is the complex dielectric function of the metal; this varies strongly with ω. The denominator of Eq. (3.10) approaches zero at the Fröhlich condition,

$$\Re\left\{|\varepsilon_1(\omega)|\right\} = -2\varepsilon_m \tag{3.11}$$

and the polarizability is resonantly amplified. The frequency at which this occurs

is the plasmon resonance frequency, ω_p.

At this resonance frequency, the absorbance efficiency, Q_{abs}, is also amplified significantly. Again, for the case of a very small sphere, the absorbance efficiency is given analytically by[80]

$$Q_{abs}(\omega) = \frac{4r}{\lambda} \frac{\varepsilon_1(\omega) - \varepsilon_m}{\varepsilon_1(w) + 2\varepsilon_m} \tag{3.12}$$

At the plasmon resonance, charge is confined to a very small volume, and in the small particle limit, the polarizability and absorbance cross sections are limited only by the imaginary part of $\varepsilon_1(\omega)$, which accounts for Ohmic losses. Strong increases in plasmonic effects are therefore expected at the plasmon resonance frequency.

3.3.2 More Complicated Metal Nanoparticle Systems

The analytical model described in Section 3.3.1 accounts only for small, isotropic spheres in a homogeneous environment. Moreover, it is based on the quasistatic approximation, where the electric field is assumed to be constant over the nanoparticle volume. Additional consideration must be given to the analysis of more complicated systems.

Larger Nanoparticles

As the dimensions of metal nanoparticles approach the wavelength of light, additional factors must be considered to account for the experimental observation that the local plasmon resonance frequency and amplitude depend strongly on the particle diameter. For these larger particles, higher-order multipolar spherical harmonic modes begin to affect the absorption and extinction spectra.[81] Such multipole modes are in general lossy and cannot contribute to the dipole-dipole interaction enhancement effects described in this chapter. The dipolar plasmon resonance itself is also not independent of particle size. Due to the finite ratio of particle size to wavelength, the electrons cannot all oscillate in phase, and such

retardation leads to a depolarization of the radiation across the particle surface. Consequently, the dipolar resonance is shifted to lower energies as the particle size grows.[79] Finally, large particles also suffer from radiative damping, which decreases the dephasing time, $T_2 \sim 5{-}10$ fs. Since the field enhancement about the plasmonic metal is directly proportional to T_2, processes that dampen the plasmon mode will lead to smaller enhanced local fields and therefore smaller optical enhancement effects.[82]

Anisotropic Nanoparticles

The formalism of Section 3.3.1 can be extended from spheres to anisotropic ellipsoids. In this case, the single-dipole resonance of the sphere is split into several plasmon modes, each with a specific directionality. Relative to a sphere of the same volume, the long-axis mode will be red-shifted and the short-axis mode will be blue-shifted.[80]

Coupling Between Closely Spaced Nanoparticles

In a chain or array of metal nanoparticles, the effect of particle interactions is determined by the polarization induced in each particle due to the fields arising from its neighboring particles.[81] These interactions give rise to very intense local-field confinement in the spaces between adjacent particles,[83] and have also been shown to permit waveguiding along particle chains.[55] At very small particle spacings, s, near-field dipolar interactions dominate; these have a s^{-3} distance dependence. For the longer distances more typical of lithographically fabricated samples, neighboring particles interact mainly through radiative far-field interactions that scale as $1/s$.[79]

Interactions between adjacent nanoparticles strongly affect the collective plasmon modes, and this result is highly dependent on the geometry of the particle assembly.[84] For chains of closely spaced particles with polarization parallel to the chain, the plasmon mode red shifts with decreasing interparticle spacing due to the constructive interference of adjacent nanoparticles upon forming this longitudinal

mode. Conversely, for chains of closely spaced particles arranged perpendicular to the direction of polarization, a transverse mode is excited. In such a mode, neighboring nanoparticles oppose one another's polarization, and this leads to a blue-shifting of the collective plasmon oscillation with decreasing spacing.[85]

Finally, for two-dimensional arrays of nanoparticles, the plasmon mode is highly dependent on the array geometry. At small separation distances, s, the above-mentioned longitudinal red shifts are generally stronger than the transverse mode blue shifts, leading to an overall red shift of the collective array plasmon with decreasing s. However, the behavior changes for larger separation distances. As s approaches $\lambda/2\pi$, retardation will prevent neighboring particles from oscillating in phase. In this case, a blue shift of the longitudinal plasmon mode is expected. Such retardation-related blue shifts are also predicted to occur for the longitudinal mode of one-dimensional arrays of nanoparticles with very large separation distances.[84]

3.4 Electromagnetic Simulations of Lithographically Attainable Metal Nanoparticles

In this thesis, we are particularly interested in the plasmon modes of lithographically attainable metal nanostructures. Due to their relatively large sizes, non-ellipsoidal shapes, and interparticle interactions, these structures are in general too complex to treat analytically, and we therefore use electromagnetic computations. In the present section, we discuss the properties of noble metal nano-assemblies investigated by finite-integration time domain simulations.

3.4.1 Finite-Integration Time Domain Calculations

The simulations in this chapter and in Chapter 6 were performed by three-dimensional full-field electromagnetic simulations utilizing finite-element integration techniques to solve Maxwell's equations.[86] This method allows us to investigate metal cylinders explicitly, rather than approximating them as oblate ellipsoids. Additionally, the effects of retardation, radiative damping, and interparticle coupling are ac-

counted for. Finally, implementing von Karman periodic boundary conditions allows us to investigate infinite one- and two-dimensional arrays.

The samples simulated in the present chapter consist of assemblies of 20 nm thick noble metal cylinders embedded in a medium with relative dielectric constant $\varepsilon = 1.6$, arranged in the xz-plane. The dipolar plasmon mode of this assembly is excited by illuminating the particle assemblies by a plane wave incident normal to the plane of particles, along the y-axis. The wave is polarized in the x-direction. After 75 fs, the incident plane wave is interrupted, and the amount of energy absorbed by the plasmon mode can be quantified. In the absence of the applied external field, the plasmon mode decays; this ringdown is observed for 100 fs, and a Fourier transform of the time decay behavior gives the characteristic oscillation rate of the mode; this is the plasmon resonance frequency.

3.4.2 Tunability of the Metal Nanoparticle Array Plasmon Resonances

Choice of Noble Metal

Gold and silver are often used in experiments of metal nanoparticle plasmonics as both have strong resonances in visible wavelengths. From a practical standpoint, gold is desirable because of its proven stability to oxidation and corrosion. Still, gold is plagued by *d-sp* electronic interband transitions that dampen the plasmon mode, whereas in silver, there is a larger spectral separation between the plasmon band and the interband transition edge. We therefore examined both of these noble metals.

Using electromagnetic simulations, we explored the difference in plasmon resonance between two-dimensional arrays of silver and gold nanoparticles. In both cases, we considered arrays of cylinders with diameter $d = 165$ nm, arranged in a square lattice with pitch (center-to-center interparticle spacing), $p = 400$ nm.

The metals are approximated using a modified Drude model fitted to tabulated data over the wavelength range of interest.[87] The dielectric function of silver, ε_{Ag},

as a function of radial frequency, ω, was given by the Drude relation,

$$\varepsilon_{Ag}(\omega) = 5.45 - 0.73\frac{\omega_{b,Ag}^2}{\omega^2 + i\omega\gamma_{Ag}} \tag{3.13}$$

where the bulk plasmon frequency is $\omega_{b,Ag} = 1.72 \times 10^{16}$ rad s^{-1}, and the plasmon decay rate is $\gamma_{Ag} = 8.35 \times 10^{13}$ s^{-1}. Similarly, the frequency-dependent dielectric function of gold, $\omega_{Au}(\omega)$, was

$$\varepsilon_{Au}(\omega) = 10.0 - 1.0\frac{\omega_{b,Au}^2}{\omega^2 + i\omega\gamma_{Au}} \tag{3.14}$$

where $\omega_{b,Au} = 1.35 \times 10^{16}$ rad s^{-1} and $\gamma_{Au} = 1.25 \times 10^{14}$ s^{-1}.

Our results for the spectral response of these arrays are shown in Fig. 3.1. The silver array (solid blue curve) has its dipole plasmon resonance at 705 nm, whereas the gold sample (dashed red curve) peaks at 790 nm. Despite the identical geometries of the two samples, because of their different dielectric functions, the plasmon resonant response of the silver nanostructure occurs at a higher energy than that of its gold counterpart.

Plasmon Modes in Particles, Chains, and Arrays

The collective plasmon mode from a collection of coupled metal nanoparticle assemblies is predicted to be different from that of an isolated single particle. We therefore used electromagnetic simulations to probe the effects of coupling particles in infinite chains and arrays. In Fig. 3.2, we consider Ag cylinders with $d = 165$ nm arranged in four different configurations: (a) an isolated single particle, (b) an infinite chain of particles aligned along the polarization direction, x, (c) an infinite chain of particles aligned perpendicular to the excitation wave polarization, and (d) an infinite two-dimensional array. In cases (b)−(d), the pitch is $p = 400$ nm. Figure 3.2 displays the intensity of the electric field induced by the applied electromagnetic field. Here, four contour lines represent an order of magnitude change in field intensity. It is clear that even at the relatively large separation distances

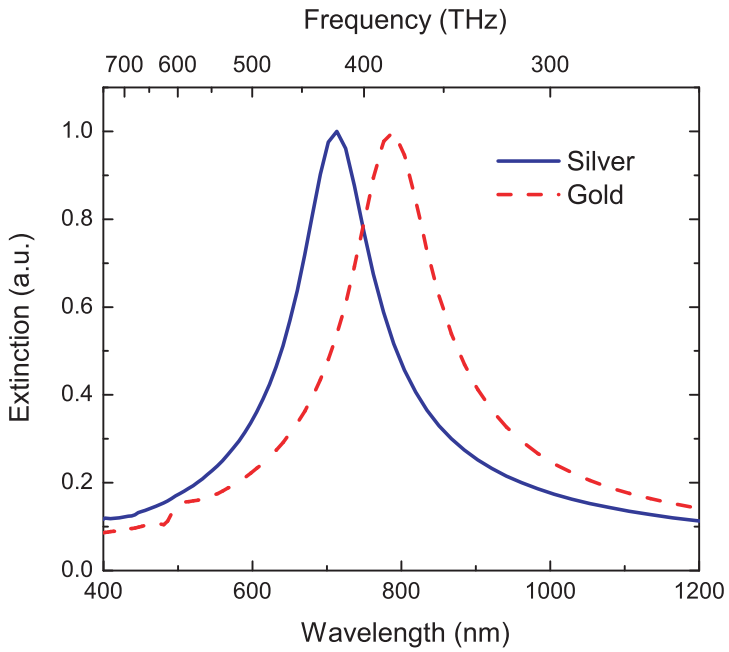

Figure 3.1: The dipole resonance modes calculated for infinite two-dimensional silver and gold nanoparticle arrays (d = 165 nm, p = 400 nm) are indicated by the solid blue and dashed red lines, respectively. The gold resonance is red-shifted from that of silver by 85 nm.

considered in this problem, the neighboring particles are strongly coupled through far-field interactions.

The spectral response of the arrays is given in Fig. 3.3. In this figure, the isolated particle (black curve) has the lowest plasmon resonance energy ($\lambda = 756$ nm). As expected, the chain aligned perpendicular to the polarization direction (green curve, $\lambda = 731$ nm) is blue-shifted relative to the single particle; this is attributed to the excitation of a higher-energy transverse mode in such a chain. At first glance it appears counterintuitive to observe that the spectral response of the chain parallel to the polarization direction (red curve, $\lambda = 719$ nm) and that of the two-dimensional array of particles (blue curve, $\lambda = 711$ nm), are blue-shifted yet further. However, as described in Section 3.3.2, we can assign this energy change to the collective retardation effects that become important at such relatively large particle spacings.

Realistic Anisotropies

When preparing cylindrical Ag particles by electron-beam lithography, the shape of the particles is determined by the stigmation and stability of the electron beam. Slight imperfections in either of these metrics invariably lead to subtle anisotropies in the particles. A deviation from a perfectly circular cylinder to a cylinder with a cross section that is an arbitrary ellipsoid is predicted to give rise to two non-degenerate dipole plasmon modes. We sought to determine the effect of typical deviations from perfectly isotropic cylinders.

In Fig. 3.4, we consider four different infinite arrays of Ag cylinders with constant pitch, $p = 400$ nm. Fig. 3.4(a) portrays isotropic cylinders with $d_x = d_z = 155$ nm. Anisotropies are introduced in Figs. 3.4(b) and (c), where the cylinders are elongated along the polarization direction (panel (b), $d_x = 175$ nm, $d_z = 155$ nm) and in the perpendicular direction (panel (c), $d_x = 155$ nm, $d_z = 175$ nm). Finally, Fig. 3.4(d) considers isotropic cylinders with $d_x = d_z = 175$ nm. The contour lines in Fig. 3.4 show the electric field intensity induced in the plane of the particles, where four lines represent an order of magnitude change in intensity.

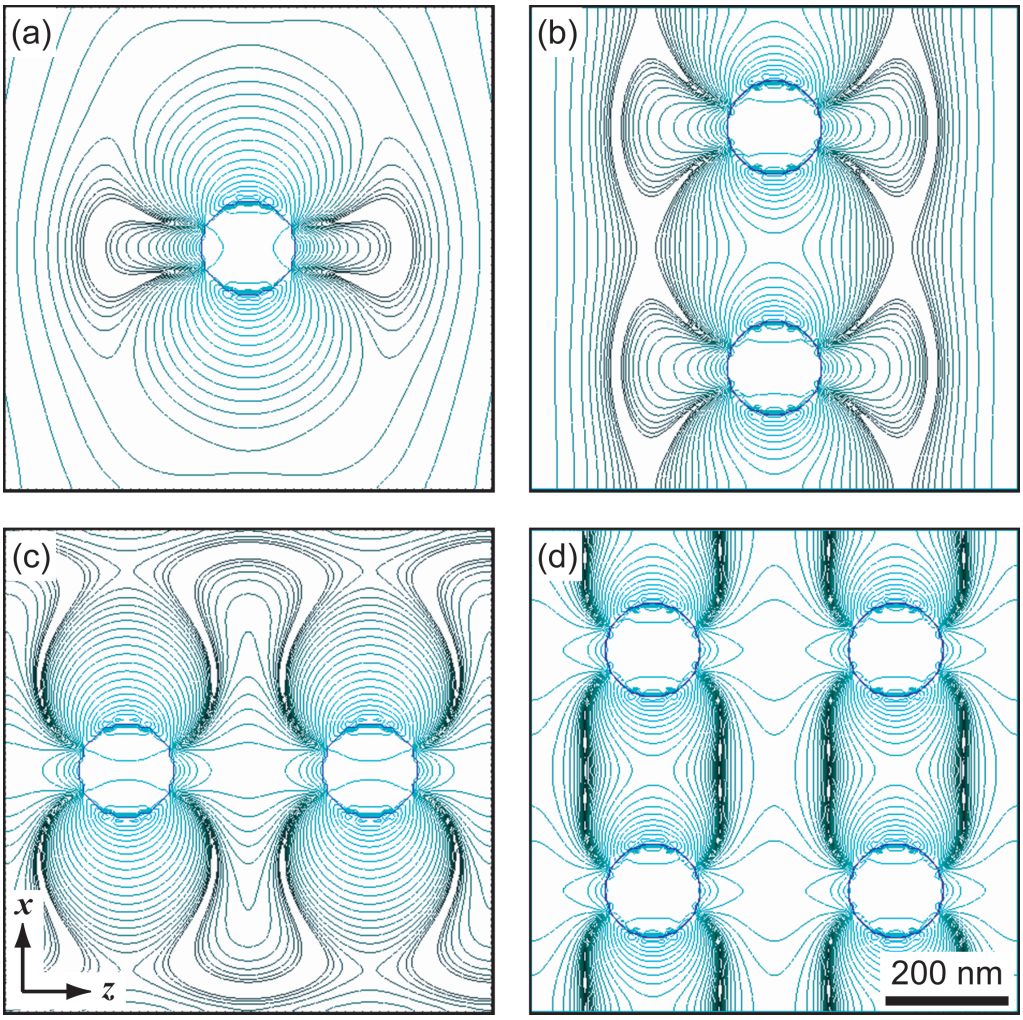

Figure 3.2: Instantaneous local-field intensities in the plane of assemblies of Ag nanocylinders with $d = 165$ nm, subject to an incident wave with polarization along the x-axis. (a) Isolated single particle, (b) infinite chain of particles aligned along the polarization direction, (c) infinite chain of particles aligned perpendicular to the excitation wave polarization, and (d) infinite two-dimensional array. In (b)−(d), the pitch is $p = 400$ nm. Four contour lines represent an order of magnitude change in the x-component of the field intensity. Each Ag assembly was excited at a wavelength close to its resonance. Excitation wavelengths for arrays (a), (b), (c), and (d) were 763, 737, 737, and 714 nm, respectively.

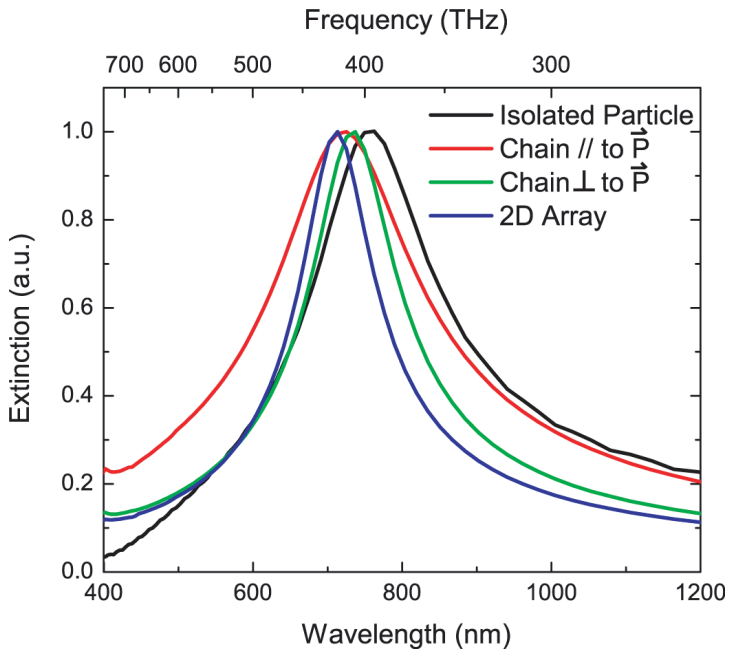

Figure 3.3: Dipole resonance modes calculated for Ag nanocylinders (d = 165 nm, p = 400 nm) assembled in four different geometries. From highest to lowest energy are the responses of the array (blue curve, 711 nm), the chain parallel to the direction of polarization (red curve, 719 nm), the chain perpendicular to the polarization direction (green curve, 731 nm), and the isolated particle (black curve, 756 nm).

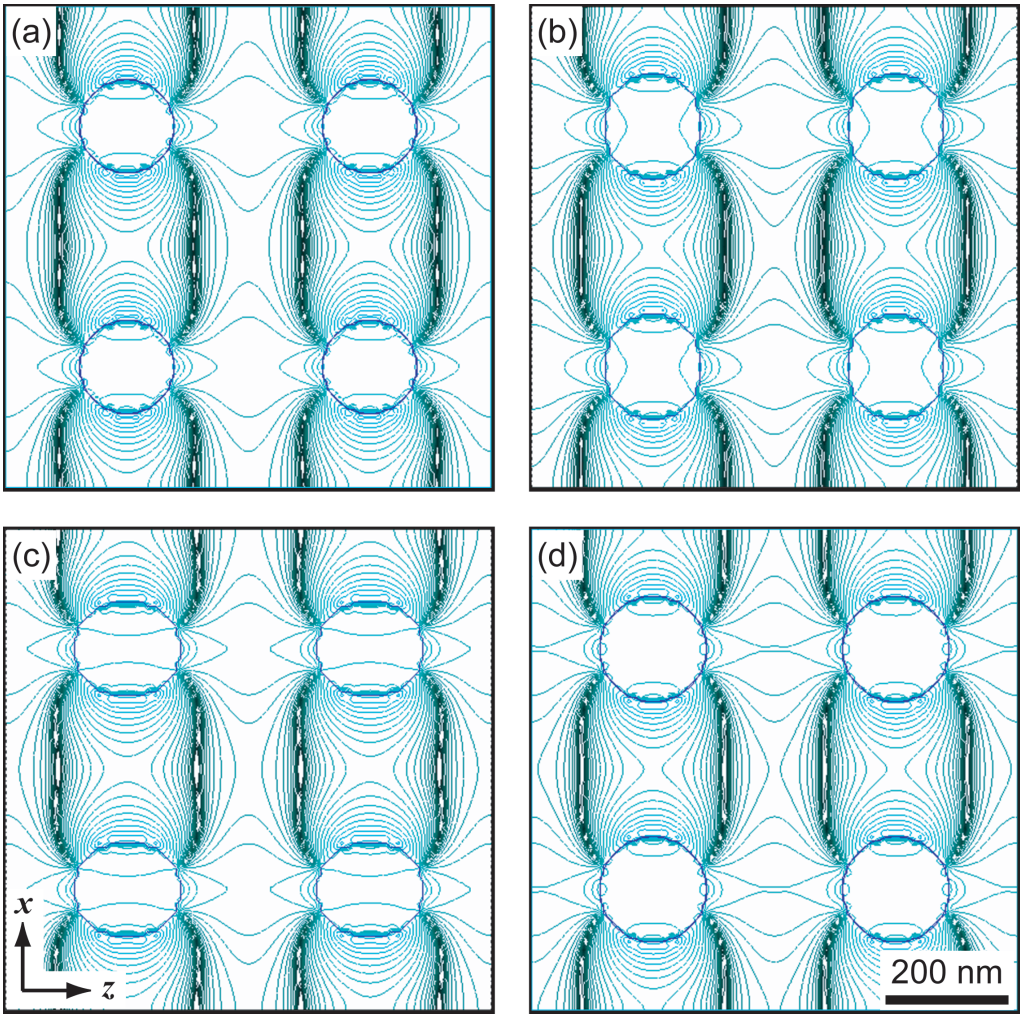

Figure 3.4: Instantaneous local-field intensity in the plane of Ag arrays with different particle anisotropies. The pitch is fixed at 400 nm, and the diameters along the two in-plane axes are: (a) $d_x = d_z = 155$ nm, (b) $d_x = 175$ nm, $d_z = 155$ nm, (c) $d_x = 155$ nm, $d_z = 175$ nm, and (d) $d_x = d_z = 175$ nm. Four contour lines represent an order of magnitude change in the x-component of the field intensity. Each array was excited at a wavelength close to its resonance. Excitation wavelengths for arrays (a), (b), (c), and (d) were 714, 763, 714, and 750 nm, respectively.

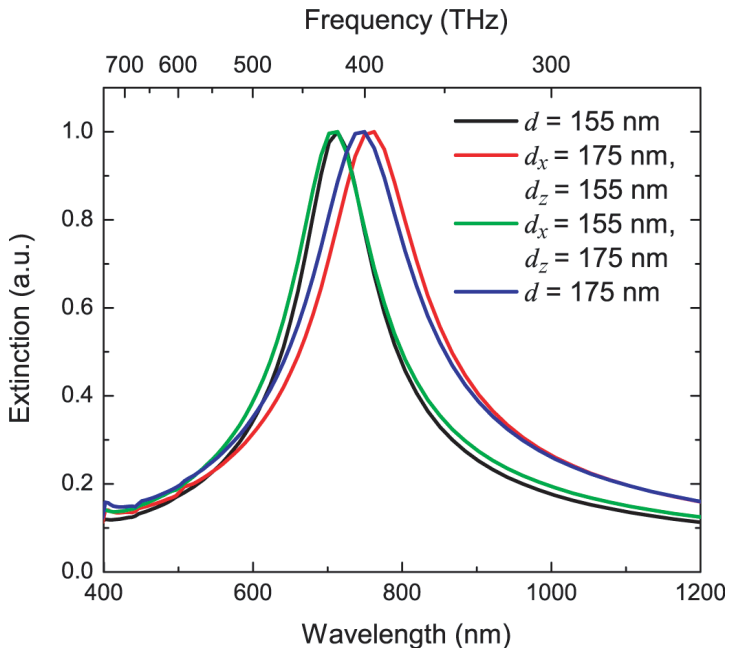

Figure 3.5: Dipole resonance modes calculated for Ag arrays with different particle anisotropies. From highest to lowest energy, the diameters along the two in-plane axes are: $d_x = 155$ nm, $d_z = 175$ nm (green curve, 707 nm), $d_x = d_z = 155$ nm (black curve, 712 nm), $d_x = d_z = 175$ nm (blue curve, 743 nm), and $d_x = 175$ nm, $d_z = 155$ nm (red curve, 756 nm).

The spectral response of the isotropic and anisotropic arrays is displayed in Fig. 3.5. Here, the isotropic, $d = 155$ nm particles (black curve) show a dipole resonance at 712 nm. Elongation of the particle in the direction perpendicular to the polarization (green curve, $d_x = 155$ nm, $d_z = 175$ nm) yields no significant change in the dipole resonance frequency ($\lambda = 707$ nm). However, elongation of the particle along the direction of polarization (red curve, $d_x = 175$ nm, $d_z = 155$ nm) causes a much larger red shift of the particle dipole resonance, to $\lambda = 756$ nm. This is attributed to an increase in the particle aspect ratio in the polarization direction, as well as to increased coupling between adjacent particles. Finally, an isotropic particle with $d = 175$ nm (blue curve, $\lambda = 743$ nm) demonstrates a very similar spectral response to that of the particle elongated in the x-direction.

Based on the results in Fig. 3.5, we can conclude that the collective plasmon resonance mode of an array is more sensitive to anisotropies in the direction of

the polarization. It is also important to note that the energy shifts induced by these anisotropies are quite subtle effects, comparable to the effect expected for a distribution in sizes of isotropic particles. Therefore, we do not expect the minor anisotropies discussed in this section to influence our experimental results strongly.

3.5 Conclusions

This chapter described the phenomenon of plasmon-enhanced emission and used analytical and computational techniques to explore the plasmon modes that give rise to this electromagnetic effect. Though the plasmon resonance modes of metal nanoparticles have been explored for over a hundred years, there is still much to be learned about these oscillations and their manifestations. The possibility for enhanced emission from silicon nanocrystals therefore motivates the next four chapters of this thesis.

Chapter 4

Enhanced Silicon Nanocrystal Emission from Coupling to Randomly Nanostructured Gold

4.1 Introduction

As discussed in the previous chapters, silicon nanocrystals (nc-Si) have many desirable properties as light emitters. These quantum dots exhibit room-temperature luminescence with high internal quantum efficiencies, and the emission energy can be tuned throughout the visible by varying the nanocrystal size[88] or surface termination.[21] However, due to the indirect band gap, Si nanocrystals suffer from low radiative emission rates and absorbance cross sections that decrease the photoluminescence (PL) intensity relative to direct band gap semiconductors and organic dyes. A method for overcoming this specific limitation and thereby increasing the emission intensity from these nanocrystals is thus highly desirable. It has been observed in compound semiconductor materials that coupling to a metal can lead to enhanced emission from solid-state quantum dots[35,36] and wells.[37]

In this chapter, we show the first evidence of PL enhancement from nc-Si coupled to metal nanostructures, and we report on a separation distance-resolved study of the photoluminescence intensity, experimental decay rate, and effective absorbance cross section. These measurements are used to deduce the radiative rate and quantum efficiency of the coupled emitter/nanostructured metal system, and our results allow us to make predictions for enhancements in an ideal system.

4.2 Theory

The system described in the present chapter takes advantage of the plasmonic nature of nanoporous gold (np-Au) to enhance the luminescence of silicon nanocrystals. Small gold particles strongly concentrate electric fields,[80] so we expect an enhanced local field to be present about the ellipsoids and spheroids that make up the np-Au film. A silicon nanocrystal in this enhanced field will have an altered optical density of states, and steady-state analysis indicates that this will enhance the decay rate of the nc-Si.[61] Moreover, the local field near a metal is inversely proportional to its radius of curvature, so the small ellipsoids in the np-Au will concentrate the electric field much more strongly than a planar Au film. We refer to the theory of plasmon enhancement, outlined in Chapter 3, to explain our experimental observations.

The nanoporous gold contains a great assortment of feature sizes and shapes. This roughness provides a fractal-like grating to couple energy of arbitrary frequencies from Au plasmon modes to far field radiation. In addition, the variety of spatial features gives rise to a range of different plasmon resonance energies. Therefore, the film absorbs over a broad spectral range, and can therefore act as a sensitizer for all nc-Si in its local field, irrespective of an emitter's specific emission energy.

4.3 Experimental

4.3.1 Preparation of Silicon Nanocrystals Coupled to Nanoporous Gold

Si nanocrystals were produced by the implantation of 11-keV Si^+ ions to a fluence of 1.7×10^{16} cm^{-2} into a 1.6 mm thick fused quartz strip (Technical Glass Products). According to Monte Carlo simulations performed with SRIM,[40] such an implantation yields a Gaussian depth distribution of implanted Si in the SiO_2, with a peak excess Si concentration of 10% at a depth of ~ 20 nm. The Si-doped

silica samples were cleaned by immersion in a solution of 5:1:1 H_2O:H_2O_2:NH_4OH at 80 °C for $10 - 20$ min, followed by a rinse in 18 MΩ·cm resistivity water. The implanted quartz was then annealed in argon for 20 min at 200 °C and 20 min at 450 °C to dry the surface, and then again for 30 min at 1000 °C to form nc-Si. The samples were subsequently heated in a forming gas ambient (10% hydrogen in nitrogen) for 30 min at 450 °C to eliminate emission from defect states in the SiO_2 matrix.[42]

After nanocrystal nucleation and growth, the surface of the 9 cm long strip of nc-Si-doped quartz sample was etched in a 1:20 mixture of 48% HF in water in a stepwise fashion. The etch rate was 0.25 nm/s, precisely calibrated by spectral ellipsometry of an analogous sample of SiO_2 on a Si substrate. Nine 2.5 nm deep steps were etched using a computer-manipulated stepper-motor to precisely control for step length (1 cm) and etch time (10 s). The 9 cm strip containing nc-Si-doped fused silica at different depths was then split lengthwise in two, and the first half was retained as a reference.

Subsequently, a film of nanoporous gold was prepared according to a method developed by Erlebacher and coworkers.[89] A 100 nm thick sheet of 12-carat gold leaf (50:50 Au/Ag alloy; Sepp Leaf Products) was dealloyed by floating on a bath of 70% nitric acid in water for 10 minutes. In this process, the selective dissolution of Ag left behind a 100 nm thick nanoporous Au film. The nanoporous gold (np-Au) film is then transferred to a bath of 18 MΩ·cm resistivity water via a graphite roller. The so-formed nanoporous gold layer was finally adhered to the nc-Si-doped silica surface without adhesive. Therefore, the Si nanocrystals in each step are at a controlled distance from the np-Au film. The final sample is represented by the schematic in Fig. 4.1, where D denotes the etch depth at each step.

4.3.2 Physical Characterization

The nanoporous gold film and the np-Au film/fused silica interface were characterized by scanning electron microscopy (SEM) with a LEO 1550VP Field Emission SEM. Since SEM requires a conductive substrate, the surface of the fused silica

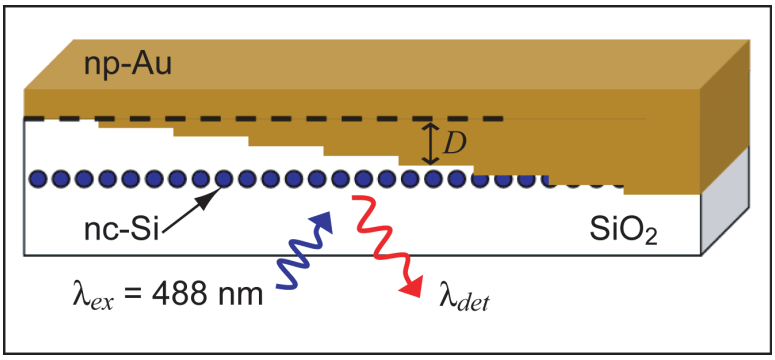

Figure 4.1: Schematic of the sample consisting of Si nanocrystals (nc-Si) separated from nanoporous gold (np-Au) in etched steps whose depths are represented by the symbol D. Photoluminescence measurements are made from the transparent side, as indicated by the blue arrow (photoexcitation at the wavelength, $\lambda_{ex} = 488$ nm) and red arrow (emission detected at λ_{det}).

samples was sputter coated with carbon to reduce charging. Additionally, samples of nanoporous gold on lightly doped silicon were used to obtain images at higher resolution.

A Sentech SE-850 spectral ellipsometer was used over the range of 300−820 nm to verify the step heights on the nc-Si-doped fused silica samples. Since precise measurements of thickness by ellipsometry require the presence of an opaque substrate beneath the film being measured, these ellipsometry measurements were performed on a silicon wafer with a 100 nm thick thermal SiO_2 layer, which served as an analog for the fused silica samples. For this purpose, the thermal-oxide-coated silicon analog was processed simultaneously with the nc-Si-doped fused silica samples during the stepwise etch described in Section 4.3.1. Since, at this relatively low concentration of nanocrystals, the nc-Si-doped fused silica and the thermal SiO_2 have approximately identical etch rates in HF, a measurement of the step heights on the thermal SiO_2 analog is a good proxy for a measurement of the step heights on the actual sample. Spectral ellipsometry with the Sentech SE-850 was also used to characterize the absorbance of the nanoporous gold film.

4.3.3 Optical Characterization

Photoluminescence (PL) spectra were acquired under excitation from the $\lambda_{ex} =$ 488 nm line of an Ar^+ laser focused to a ~ 1 mm^2 spot. The PL intensity was measured using a charge-coupled device detector (sensitivity range $200-1100$ nm), cooled with liquid nitrogen to $-132\,^{\circ}$C, in conjunction with a 27.5 cm focal length grating spectrograph. A dichroic filter that cuts off wavelengths below 510 nm was used to eliminate scattered laser light from the measurements.

Time-resolved PL measurements were performed by chopping the 488 nm excitation source with an acousto-optic modulator (AOM) at a frequency of 250 Hz. Photoluminescence emission at wavelengths of $\lambda_{det} = 780 \pm 20$ nm was selected with the spectrograph, and this PL emission was recorded with a GaAs photomultiplier tube in conjunction with a multichannel photon counting system. The time resolution of the system was ≤ 50 ns. PL measurements were made by exciting the nc-Si and collecting emission through the transparent side of the samples, as indicated by the arrows at the bottom of Fig. 4.1, and the reference sample was laid nanocrystal-side down on a polished silicon substrate to account for any reflection effects in the coupled np-Au/nc-Si sample.

4.4 Results and Discussion

4.4.1 Physical Characteristics of the Nanoporous Gold/Silicon Nanocrystal Sample

Of great importance for understanding the physics of the coupled metal nanostructure/semiconductor emitter system investigated in this chapter is the ability to carefully control the separation distance between the nc-Si and the np-Au. Before exposure to HF, the center of the nc-Si distribution is 19.2 nm beneath the fused silica surface. The purpose of the stepwise etch, then, is to produce macroscopically accessible mesas with a constant mean nc-Si depth that steadily decreases from the initial 19.2 nm. The results from an ellipsometric study of the thermal SiO_2 on Si analog described in Section 4.3.2 are shown in Fig. 4.2. This map of

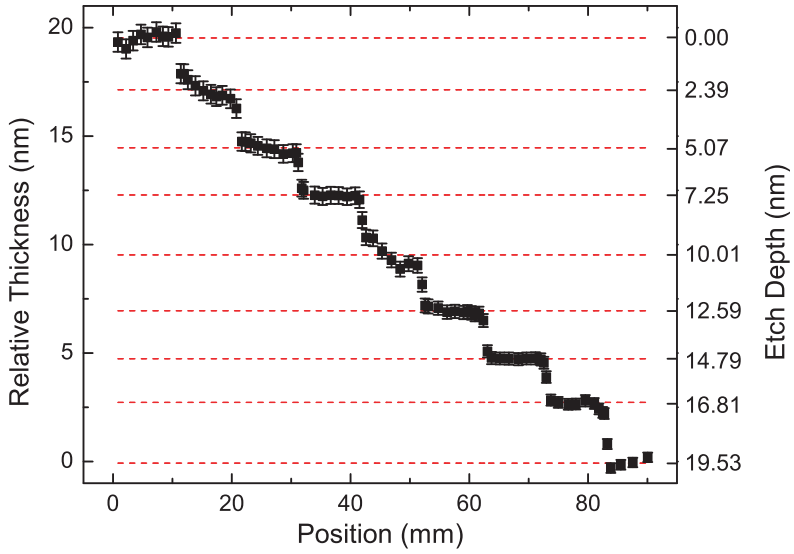

Figure 4.2: Step thicknesses measured by mapping the etched sample with spectral ellipsometry, showing nine 1 cm wide steps, each one uniform within ± 0.2 nm across the majority of its length.

thicknesses along the length of the etched SiO_2 film demonstrates that the etching procedure produced nine 1 cm wide steps, and that each step was uniform within ± 0.2 nm across the majority of its length. The results from ellipsometry indicate that, when the np-Au is adhered to such a stepped sample, at each gradation it is brought $\sim$ 2.5 nm closer to the center of the nc-Si distribution.

As indicated in Section 4.3.1, the np-Au layer is affixed to the nc-Si doped silica by hydrophilic interactions alone, without any additional adhesives. Even given the flat gradations produced by the stepwise etch procedure, constant, well-characterized metal/semiconductor separation distances can still only be achieved if the np-Au film is in close contact with the fused silica substrate. Scanning electron microscopy (SEM) was used to verify that this condition was indeed true. Figure 4.3 shows an SEM image of the fused silica/np-Au interface, taken at 100kx magnification. This image has a low resolution due to the insulating silica. Still, the SEM shows that the metallic film is in close contact with the fused silica layer. It also indicates that the np-Au film is 100 nm thick.

Despite the fact that the sample imaged in Fig. 4.3 was sputtered with carbon,

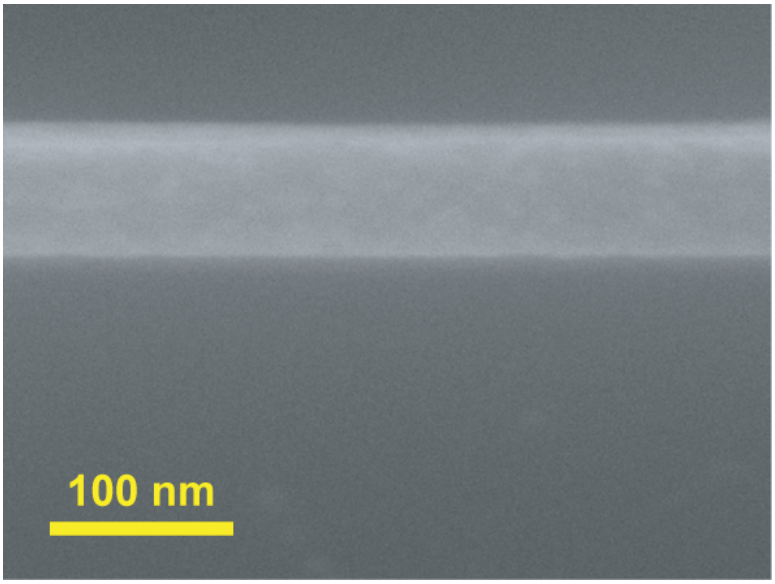

Figure 4.3: SEM image of np-Au film on nc-Si-doped fused silica at 100kx magnification showing that the np-Au film is 100 nm thick and in close contact with the SiO_2 substrate.

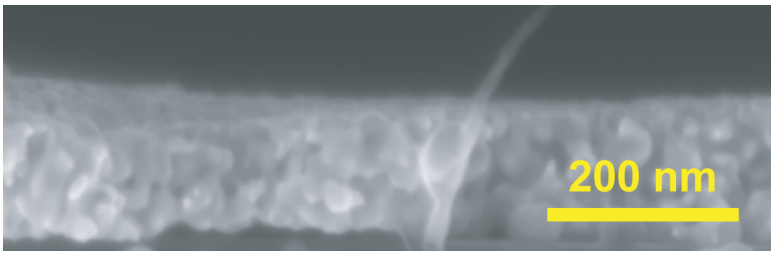

Figure 4.4: SEM image of np-Au film on Si substrate at 50kx magnification showing the fine structure of the np-Au film in cross section.

the fused silica layer is an excellent insulator and therefore subject to charging in the SEM. To obtain higher resolution images of the np-Au film, we therefore prepared samples of np-Au films on lightly doped silicon wafers. Fig. 4.4 shows the SEM image of such a sample in cross section, taken at 50kx magnification. The introduction of the conductive silicon substrate permits the imaging of much smaller features, and the porous nature of the np-Au film becomes clearly discernable.

The fine features of the np-Au film are best studied with a plan-view SEM image of the film's top surface. Figure 4.5 shows that the selective dissolution of Ag in nitric acid in Section 4.3.1 leaves behind a nanoporous gold film composed

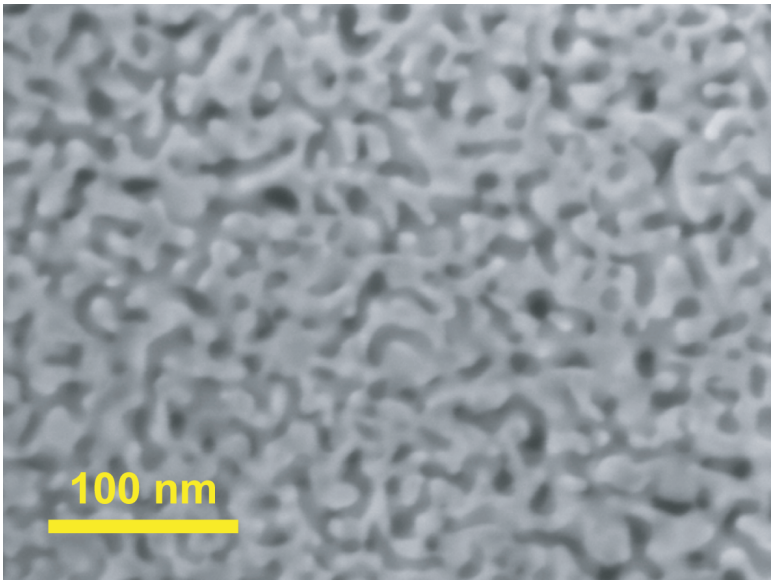

Figure 4.5: Plan view SEM (100kx magnification) of the np-Au surface showing features on the order of 10 nm.

of approximately 50% Au and 50% voids. From this 100kx-magnification SEM image, the gold feature dimensions are determined to be on the order of 10 nm, and we see that the features range from spheres to prolate spheroids with aspect ratios up to $\sim$ 1:3.

4.4.2 Evaluation of the Distribution of Silicon Nanocrystals by Photoluminescence Spectroscopy

Monte Carlo calculations predict that the 11-keV Si^+ ion implantation energy chosen in this experiment gives a Gaussian implantation profile with mean Si^+ depth of $\sim$ 20 nm. The Gaussian Si^+ ion implantation profile used to produce the nc-Si sample has been previously observed to give a Gaussian distribution of nc-Si concentrations, in which larger nanocrystals are abundant at the center of the distribution, where a greater Si excess exists, and smaller nanocrystals lie mainly in the tails.[90] The stepwise etched reference (no np-Au) sample provides a good platform for characterizing the actual distribution of nanocrystal sizes and concentrations in our samples; in contrast to imaging with microscopy, this method

has the advantage of detecting only the optically active nc-Si.

The triangles in Fig. 4.6(a) shows the PL intensity, I_{PLref}, of the reference sample integrated over all wavelengths as a function of etch depth, D, in the range $0-20$ nm. With each etch step, the top 2.5 nm of the nc-Si distribution is removed, and $I_{PLref}(D)$ decreases accordingly. The dashed line in Fig. 4.6(a) is a fit of the decreasing PL intensities to the integral of a stepwise-etched Gaussian distribution. The emission intensities are consistent with an initial nc-Si distribution, N_{total}, given by

$$N_{total}(d) \propto \exp\left[\frac{-2}{(14.1)^2} \cdot (d - 19.2)^2\right] \tag{4.1}$$

where d is the distance from the unetched surface. This Gaussian distribution is centered at a depth of 19.2 ± 0.1 nm from the unetched surface, and it has a width of 14.1 ± 0.2 nm. The blue line in Fig. 4.7 illustrates this result. The large, 14.1 nm distribution width in Eq. (4.1) indicates that the optical phenomena reported in this chapter contain contributions from Si nanocrystals strongly coupled to np-Au as well as from non-interacting nanocrystals much farther away from the np-Au; the quantitative analysis in Appendix B considers such distribution effects.

The sizes of the Si nanocrystals within the Gaussian distribution of nc-Si were inferred from the variation of the average PL emission wavelength with D (not shown), and the average nanocrystal size was found to be depth-dependent. The measured trends confirm previous reports that smaller nanocrystals, characterized by their bluer emission, form in the wings of the concentration distribution, while bigger nanocrystals, which have redder emission, are more prevalent toward the center.[90]

For the measurements in this chapter, it is desirable to characterize the emission from a specific size of Si nanocrystals. We select nanocrystals that emit at 780 ± 20 nm. Within the Si nanocrystal ensemble, those emitting at 780 nm are of an intermediate size, and we therefore expect them to have a bimodal concentration profile about the $d = 19.2$ nm distribution center. The squares in Fig. 4.6(b) show the dependence of the PL intensity on D for emission at this specific detection

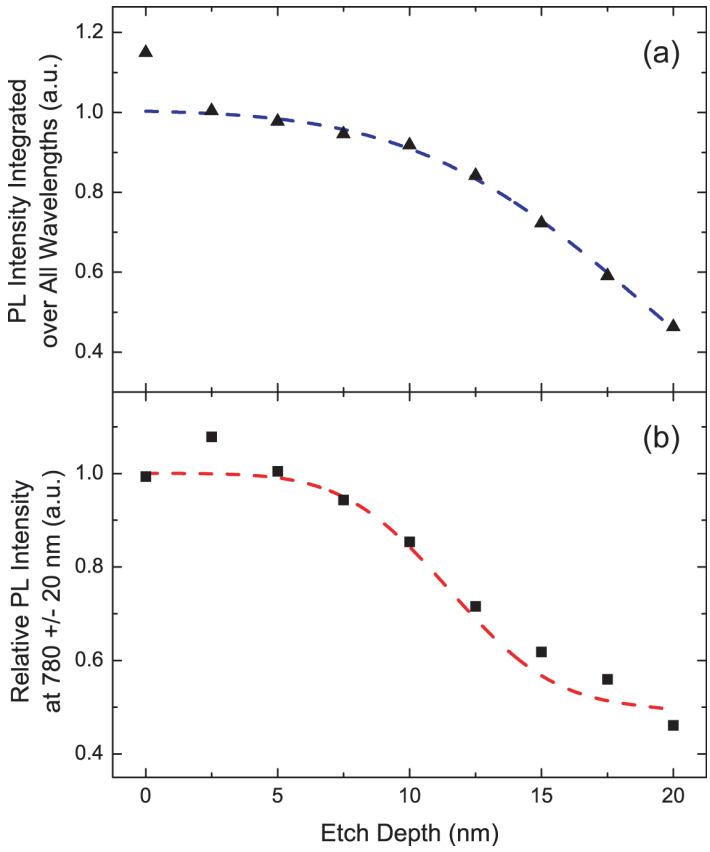

Figure 4.6: PL intensity of the reference sample as a function of etch depth, D. (a) PL intensity integrated over all wavelengths. (b) PL intensity detected at 780 $\pm$ 20 nm only.

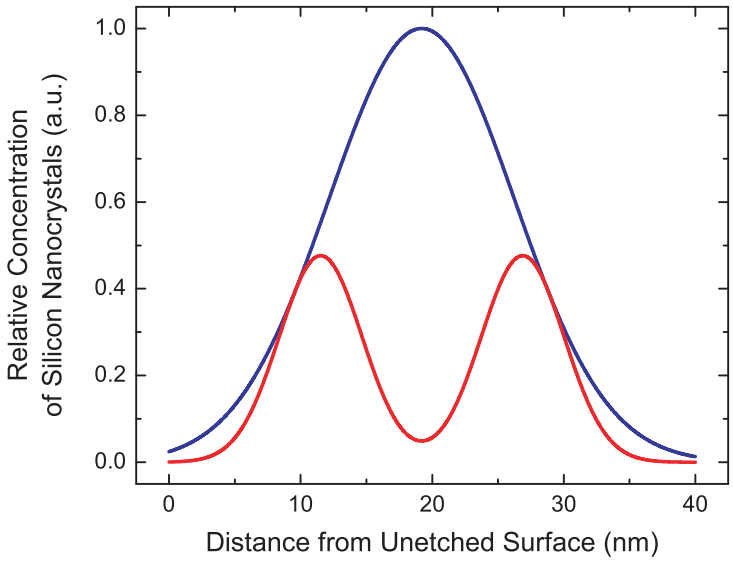

Figure 4.7: Depth distributions of optically active silicon nanocrystals in fused silica as inferred from the PL intensity variation with depth. Blue curve: Distribution of all nanocrystals. Red curve: Distribution of nanocrystals emitting at 780 ± 20 nm only, described by the sum of two Gaussians as in Eq. (4.2).

wavelength range, $\lambda_{det} = 780 \pm 20$ nm. The dashed line in this figure is a fit to the integral of a distribution that is the product of the total nanocrystal distribution, N_{total}, with the sum of two Gaussian distributions, peaking at 9.6 and 28.8 nm, respectively. This 780 nm emitter nanocrystal distribution, N, is given by

$$N(d) \propto N_{total}(d) \times \left\{ \exp\left[\frac{-2}{(7.05)^2} \cdot (d - 9.6)^2\right] + \exp\left[\frac{-2}{(7.05)^2} \cdot (d - 28.8)^2\right] \right\} \quad (4.2)$$

where d is the distance from the unetched fused silica surface. The bimodal red curve in Fig. 4.7 plots the trend in Eq. (4.2). Given this calculated distribution, it then becomes possible to take the etch depth, D, as a measure of the np-Au/nc-Si separation distance.

4.4.3 Ellipsometric Study of the Nanoporous Gold Film Extinction

The nanoporous gold film was characterized optically by ellipsometry. Spectra of the transmission, T, and reflection, R, were used to calculate the absorbance spectrum, $A = 1 - (T + R)$. Based on the np-Au film thickness of 100 nm, measured by SEM, the extinction cross section spectrum in Fig. 4.8 (red line) was derived from this measured absorbance, assuming, also based on SEM data, that the average np-Au particle in the 50% Au/50% air film is a sphere of radius 10 nm. In Fig. 4.8, the np-Au film has a broad extinction spectrum that shows a peak between 300 and 400 nm, and a tail that decreases with increasing wavelength through most of the visible spectrum. A 100 nm thick film of continuous Au deposited on SiO_2 by evaporation was also studied with the Sentech SE-850, and its transmission and reflection spectra were used to determine its absorbance spectrum (not shown). Though the absorbance cross sections of both np- and bulk Au peak at similar wavelengths, the percent absorbance of np-Au is more than three times that of planar bulk Au throughout the visible, and np-Au absorbs over a broader wavelength range than bulk Au. According to Mie-Gans theory,[80] the measured np-Au extinction cross section in Fig. 4.8 is consistent with the aggregate surface plasmon resonance response for a continuum of features including Au spheres and spheroids in air and spherical and spheroidal voids in gold, which corresponds to the morphology inferred from the plan view SEM image in Fig. 4.5.

At excitation wavelengths in the range considered in Fig. 4.8, the silicon nanocrystal absorbance cross section at an emission wavelength of 780 nm has been measured by Garcia et al.[91] (solid triangles), Kovalev et al.[92] (solid squares), and the present work, Section 4.4.4 (open circle). The extinction cross section of np-Au is much higher than that of nc-Si over this whole spectrum; for visibility, the latter is magnified by a factor of 20 in Fig. 4.8. The trend in Si nanocrystal absorbance cross sections is fit to a decreasing exponential (blue line), and it is found that the decreasing Si nanocrystal cross sections obey a trend similar to the np-Au cross sections, but that np-Au has a much larger absorbance cross section

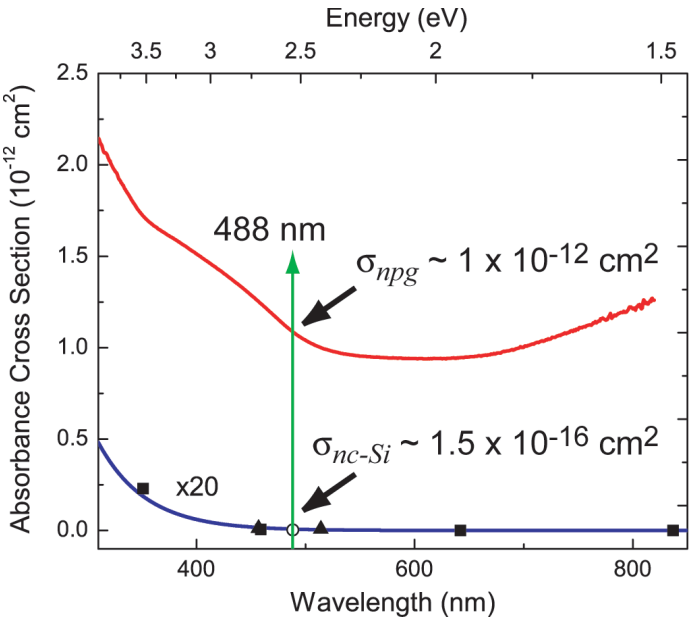

Figure 4.8: Red line: extinction cross section of np-Au as a function of absorbance wavelength. Blue line: fit to nc-Si absorbance cross section as measured at $\lambda_{det} = 780$ nm in reference 91 (solid triangles), reference 92 (solid squares), and the present work (open circle). At the pump wavelength, $\lambda_{ex} = 488$ nm, used in this experiment, the nanoporous gold film has an extinction cross section that is 7000 times greater than that of nc-Si.

than Si nanocrystals at all wavelengths investigated. For example, at the excitation wavelength, $\lambda_{ex} = 488$ nm, used in this experiment, the cross section of the np-Au film is four orders of magnitude greater than that of silicon nanocrystals. The np-Au can therefore act as a sensitizer for nc-Si, thereby increasing its effective absorbance cross section,[61] whether excited directly by a photon or indirectly by a surface plasmon.

4.4.4 Photoluminescence Measurements of the Nanoporous Gold/ Silicon Nanocrystal System

Variations in Photoluminescence Spectrum

Typical PL spectra from the reference and coupled np-Au/nc-Si samples are reported in Fig. 4.9 (black and red lines, respectively) for an etch depth, $D = 5$ nm, and for an excitation power density, $P_{ex} = 50$ mW/mm^2. The PL intensity of the coupled sample is slightly blue-shifted with respect to the reference sample, but the most notable feature is the increase in emission intensity in the np-Au/nc-Si sample relative to the reference.

We define the photoluminescence (PL) intensity enhancement, $\eta_{PL}(D)$ at depth D, as the ratio between the PL intensity of the np-Au/nc-Si coupled sample, $I_{PLnpg}(D)$, and the PL intensity, $I_{PLref}(D)$, of the reference sample, i.e., $\eta_{PL}(D) = I_{PLnpg}(D)/I_{PLref}(D)$. In Fig. 4.10, we report the magnitude of this enhancement integrated over all emission wavelengths, as a function of D, for two different pump powers. The red circles show the PL enhancement at a low pump power, $P_{ex} = 50$ mW/mm^2. We find that η_{PL} is greater than one (i.e., $I_{PLnpg} > I_{PLref}$) for all D, and there is a maximum PL enhancement of ~ 4 when 7.5 nm $< D <$ 15 nm.

However, I_{PLref} and I_{PLnpg} also vary with pump power. The dependence of I_{PLref} and I_{PLnpg} on P_{ex} at $D = 10$ nm, displayed in Fig. 4.11, shows that I_{PLref} (solid squares) increases linearly with P_{ex} up to ~ 120 mW/mm^2, and then grows sublinearly with further increases in P_{ex}, finally achieving its saturated intensity at $P_{ex} \sim 250$ mW/mm^2. The open circles in Fig. 4.11 show that for the coupled

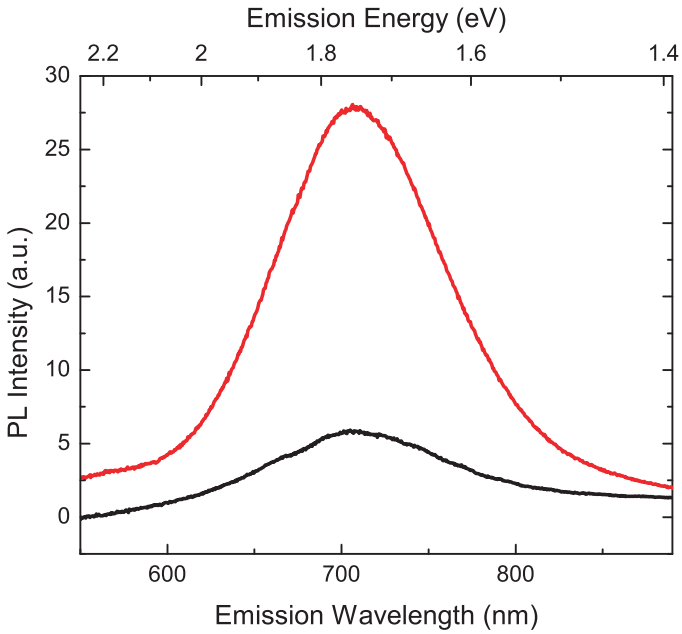

Figure 4.9: Typical PL spectra for the reference (black) and coupled np-Au/nc-Si (red) samples, at $D = 5$ nm and $P_{ex} = 50$ mW/mm^2.

sample, I_{PLnpg} increases linearly with P_{ex} to ~ 170 mW/mm^2, and does not fully saturate for any value of P_{ex}, up to the highest experimentally attainable pump power of 417 mW/mm^2. Similar trends were observed for all values of D, and the difference between the reference and coupled samples was most pronounced for D between 7.5 and 12.5 nm. Due to the reduced saturation effects in the coupled np-Au/nc-Si sample, the enhancement η_{PL} is more pronounced at higher pump powers: η_{PL} at $P_{ex} = 400$ mW/mm^2 is plotted in the blue squares in Fig. 4.10; at this pump power, η_{PL} is larger than it was at the lower power, and peaks at ~ 7.5 when $D = 7.5 - 10$ nm.

It is interesting to consider the role played by the nanoporous gold in this system. As was seen in Fig. 4.8, the np-Au film has an absorbance that peaks at wavelengths considerably shorter than the Si nanocrystal emission, itself centered at $\sim$ 780 nm. For the total PL intensity enhancements in Fig. 4.10, emission enhancement is then a primarily non-resonant process, which is predicted to be much weaker than a resonant one.[61] Still, the existence of nanostructure in the

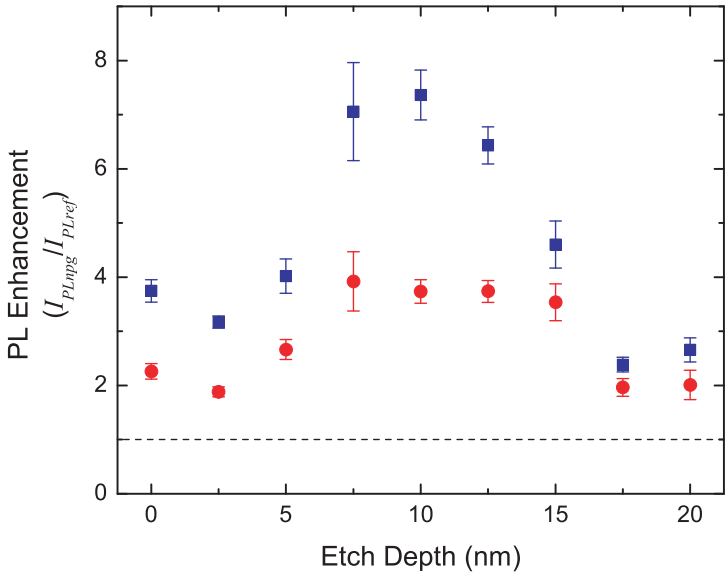

Figure 4.10: The enhancement in PL intensity, integrated over all emission wavelengths, was measured as a function of etch depth at P_{ex} = 50 mW/mm^2 (red circles) and 400 mW/mm^2 (blue squares).

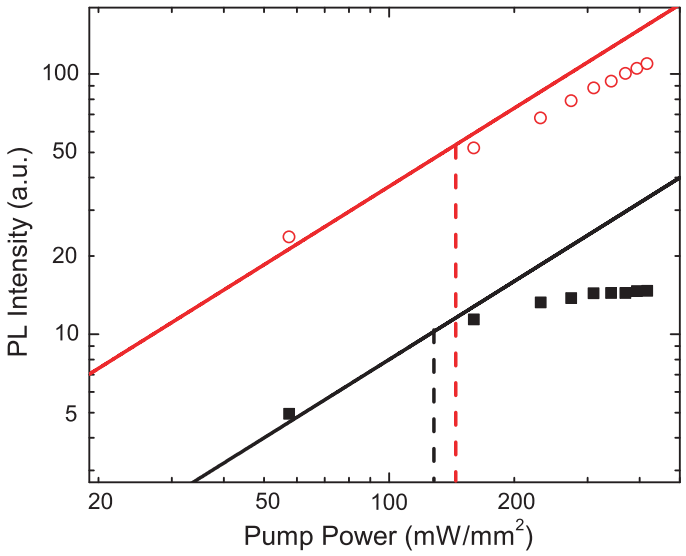

Figure 4.11: Total PL intensity integrated over all wavelengths, as a function of pump power, P_{ex}, at etch depth, D = 10 nm, for the reference sample (closed squares) and coupled sample (open circles), and fit of first data points (solid curves) to linear trends from which the reference sample deviates to a greater degree than the coupled sample as a result of saturation effects. The points at which saturation begins in the reference and coupled samples are indicated by the dashed black and red lines, respectively.

porous gold is important. Indeed, we found that, for all separation distances, upon replacing the np-Au film by a film of continuous Au, the luminescence intensity was decreased relative to an uncoupled reference sample, whereas luminescence from nc-Si near nanoporous gold was never reduced from the reference value.

According to the absorbance spectrum of np-Au in Fig. 4.8, we expect resonantly enhanced emission to be possible only in the case of the smallest (bluest) nanocrystals in the nc-Si ensemble. Since resonant enhancement effects are predicted to be much stronger than non-resonant contributions, we expect that even if a very small number of emitters are resonantly coupled, their emission should be disproportionately intense, and therefore detectable. We typically found in our samples that the enhanced np-Au/Si nanocrystal sample emits with a PL spectrum with a peak that is slightly blue shifted relative to the reference PL spectrum, and that the peak width is broadened. This is indeed consistent with the smallest nanocrystals experiencing greater emission enhancement than larger nanocrystals.

Variations in Photoluminescence Dynamics at a Single Emission Wavelength

To understand the origin of the PL enhancement better, we fix the detection wavelength at $\lambda_{det} = 780 \pm 20$ nm, thus focusing our investigation on a precise Si nanocrystal size, since the nc-Si PL wavelength is size-dependent. We also select the low excitation power regime by restricting measurements to $P_{ex} \leq 100$ mW/mm^2. In Fig. 4.12, the PL intensities measured at $\lambda_{det} = 780$ nm for both the reference (squares) and the np-Au/nc-Si coupled sample (circles) are reported as a function of D for $P_{ex} = 50$ mW/mm^2. From these measurements, the enhancement, η_{PL} at $\lambda_{det} = 780$ nm, is calculated; this ratio is reported in the red triangles of Fig. 4.13. Interestingly, the PL intensity enhancement is > 1 for all the etching depths and has a maximum value $\gtrsim 4$ at $D = 10$ nm. There is also evidence of a rising tail at $D = 20$ nm due to the bimodal distribution of nanocrystal concentrations outlined in Fig. 4.7. The green line in Fig. 4.13 is the fit of the measured $\eta_{PL}(D)$ to a model described in Appendix B. This model accounts for the spatial distri-

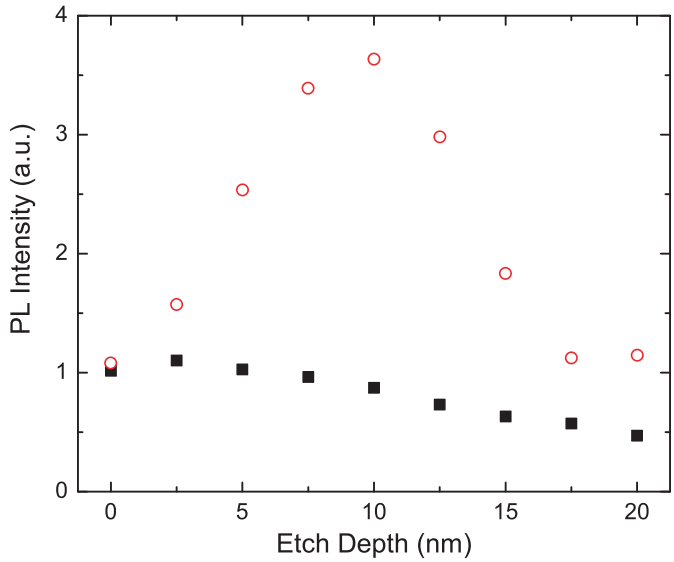

Figure 4.12: PL intensities at 780 nm vs. etch depth, D, for the reference (squares) and coupled np-Au/nc-Si (circles) samples.

bution of nanocrystals in the sample, the r^{-6} decay of the enhanced local field, which gives rise to enhancements with metal/emitter separation distance, r, and emission quenching at very small separation distances.

It is clear that the presence of the np-Au layer in proximity to the nc-Si plays a crucial role in determining the optical properties of the emitting centers. To understand the physical origin of the increase in luminescence intensity, we begin by noticing that, for a given photon flux, ϕ, the PL intensity of n optically active emitting centers is directly proportional to the product of the number of excited centers, n^*, and the radiative decay rate, Γ_{rad}. In particular, under steady-state conditions, an analysis of the two-level system allows us to express this relationship as

$$I_{PL} \propto n^* \cdot \Gamma_{rad} = \frac{\sigma\phi}{\sigma\phi + \Gamma_{exp}} \cdot n \cdot \Gamma_{rad} \tag{4.3}$$

where σ is the excitation cross section, and the experimental decay rate, $\Gamma_{exp} = \Gamma_{rad} + \Gamma_{nr}$, comprises the radiative as well as the non-radiative de-excitation paths.

As shown in Fig. 4.11, non-radiative recombination processes such as Auger recombination are induced by high pump powers. In the low-excitation regime,

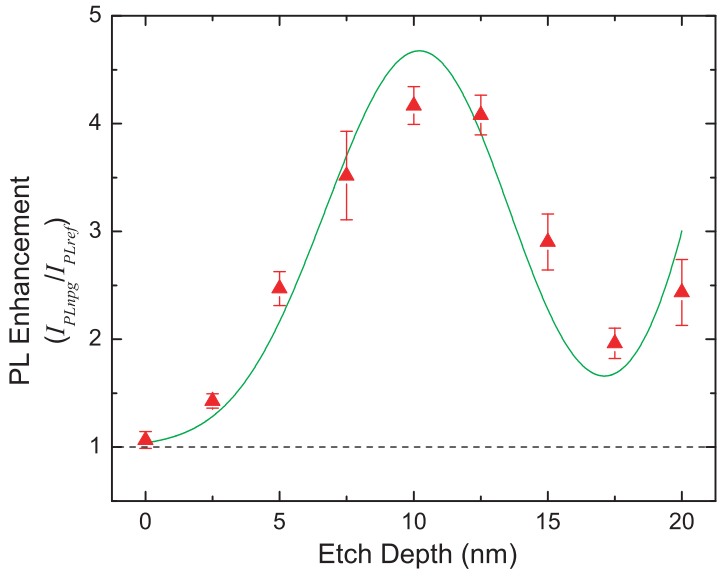

Figure 4.13: PL intensity enhancement, η_{PL}, measured at 780 nm as a function of etch depth, D (triangles). The solid line is a fit to the data using a model that accounts for the spatial distribution of Si nanocrystals in Fig. 4.7 and the enhanced local-field that decays as r^{-6} with separation distance. The solid line is a fit to the data using the model described in Appendix B, which accounts for the spatial distribution of Si nanocrystals and the decay of the enhanced local field.

however, nc-Si is not plagued by such effects, and we thus perform the remainder of the measurements in the present chapter with low power density excitation. In this regime, Eq. (4.3) reduces to

$$I_{PL} \propto n \cdot \frac{\sigma\phi}{\Gamma_{exp}} \cdot \Gamma_{rad} \quad (\sigma\phi \ll \Gamma_{exp}) \tag{4.4}$$

This equation indicates that, for a fixed number of optically active centers and a constant photon flux, the PL intensity depends on measurable physical quantities such as σ and Γ_{exp}, as well as on the radiative emission rate, Γ_{rad}, whose value is mostly unknown. Since, for a given etch depth, ϕ and n are identical for both the reference and the np-Au/nc-Si coupled samples, the PL intensity enhancement, $\eta_{PL}(D)$, can be formulated based on Eq. (4.4) as follows,

$$\eta_{PL} = \frac{I_{PLnpg}}{I_{PLref}} = \left(\frac{\sigma_{npg}}{\sigma_{ref}} \cdot \frac{\Gamma_{rad \cdot npg}}{\Gamma_{rad \cdot ref}} \cdot \frac{\Gamma_{exp \cdot ref}}{\Gamma_{exp \cdot npg}} \right) = \frac{\eta_\sigma \cdot \eta_{\Gamma_{rad}}}{\eta_{\Gamma_{exp}}} \quad (\sigma\phi \ll \Gamma_{exp}) \tag{4.5}$$

Here, the enhancements, $\eta_\sigma(D) = \sigma_{npg}(D)/\sigma_{ref}(D)$, $\eta_{\Gamma_{rad}}(D) = \Gamma_{rad \cdot npg}(D)/\Gamma_{rad \cdot ref}(D)$, and $\eta_{\Gamma_{exp}}(D) = \Gamma_{exp \cdot npg}(D)/\Gamma_{exp \cdot ref}(D)$ are increases in the effective excitation cross section, the radiative decay rate, and the experimental decay rate, respectively, at etch depth D.

The effective excitation cross sections of the reference and coupled np-Au/nc-Si samples, σ_{ref} and σ_{npg}, were determined from measurements of the PL rise time at $\lambda_{det} = 780 \pm 20$ nm with a technique derived from the steady-state relationships presented above.[92,93] The rise time, τ_{on}, defined as the average $1/e$ time required for the PL intensity to reach its saturation value, is inversely related to σ, according to the expression

$$1/\tau_{on}(\phi) = \sigma\phi + \Gamma_{exp} \tag{4.6}$$

The turn-on rate, $\Gamma_{on} = {\tau_{on}}^{-1}$, was measured as a function of the photon flux, ϕ, in the reference and np-Au/nc-Si samples at each D; the results for $\Gamma_{on}(D = 10$ nm) are shown in Fig. 4.14 for the reference (squares) and coupled (circles) samples. The absorbance, $\sigma(D)$, is determined from the slope of these trends; σ_{ref} was found

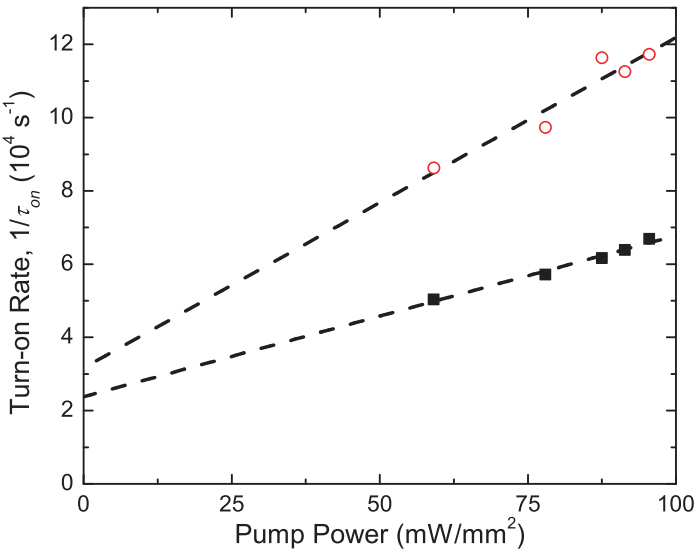

Figure 4.14: Representative values of turn-on rate as a function of pump power (at $D = 10$ nm) that are used with Eq. (4.6) to calculate the absorbance cross sections for the reference (solid squares) and coupled (open circles) samples.

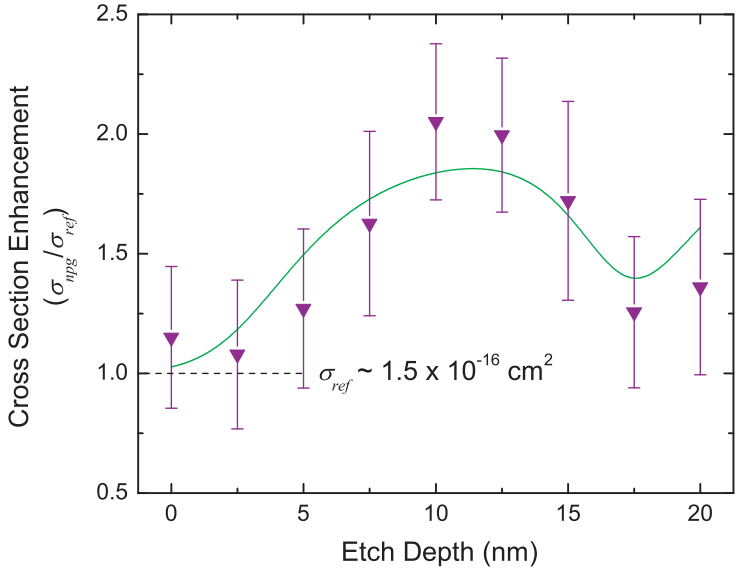

Figure 4.15: Effective excitation cross section enhancement, η_σ, at 780 $\pm$ 20 nm as a function of etch depth, D. The solid line is a fit to the data using the model described in Appendix B, which accounts for the spatial distribution of Si nanocrystals and the decay of the enhanced local field.

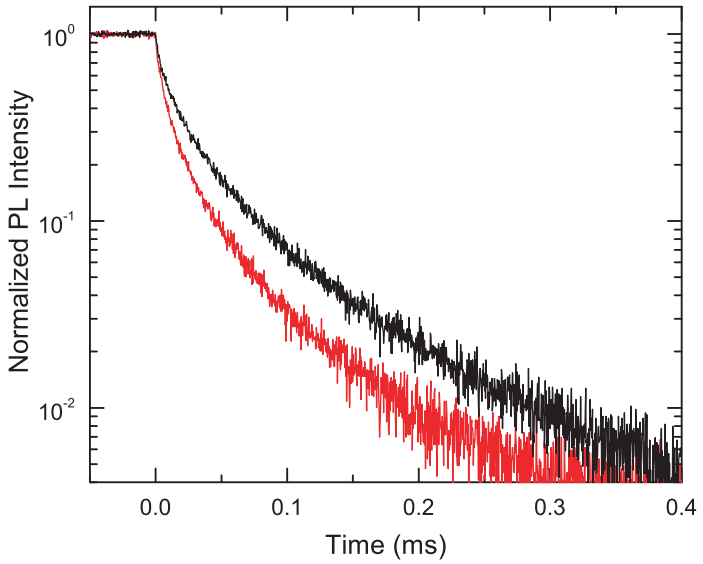

Figure 4.16: Representative PL decay traces for the reference (black) and coupled np-Au/nc-Si (red) samples at $D = 10$ nm.

to be essentially constant at $\sim 1.5\times10^{-16}$ cm^2, while $\sigma_{npg}(D)$ was highly dependent on D and always greater than or equal to $\sigma_{ref}(D)$. The inverted triangles reported in Fig. 4.15 show the excitation cross section enhancement, $\eta_\sigma(D)$, as a function of etch depth, D. The peak value is greater than 2 at $D = 10{-}12.5$ nm, meaning that at the optimal separation distance, the effective excitation cross section for the nc-Si emitting at 780 nm is enhanced by a factor of 2 in presence of the np-Au layer. This enhancement alone, however, cannot account for the four-fold increase in PL intensity in Fig. 4.13. Therefore, according to Eq. (4.5), either or both Γ_{exp} and Γ_{rad} must also be affected by the np-Au layer.

Figure 4.16 shows representative curves for the experimental PL decay of both samples at $D = 10$ nm. The decay of nc-Si emission intensity, $I_{PL}(t)$, is fitted with a stretched exponential function,

$$I_{PL}(t) = I_{PL,0} \exp\left[-\left(\Gamma_{exp} \cdot t\right)^{\beta}\right] \tag{4.7}$$

where $I_{PL,0}$ is the initial PL intensity, t is the time, Γ_{exp} is the experimental decay rate, and the parameter β is essentially constant at ~ 0.75 for the samples

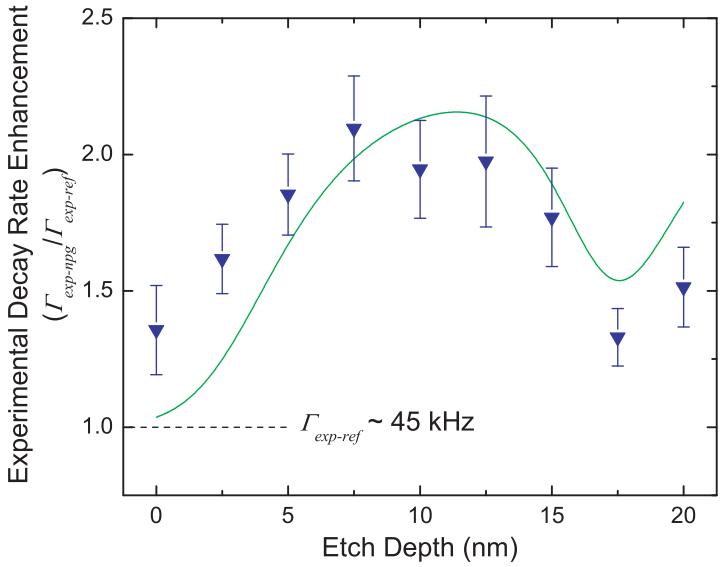

Figure 4.17: Experimental decay rate enhancement, $\eta_{\Gamma_{exp}}$, at 780 ± 20 nm as a function of etch depth, D. The solid line is a fit to the data using the model described in Appendix B, which accounts for the spatial distribution of Si nanocrystals and the decay of the enhanced local field.

considered in this chapter.

The PL intensity from the np-Au/nc-Si sample decays faster than the reference sample, and this was true at all etch depths. In particular, the reference sample is characterized by an experimental decay rate, $\Gamma_{exp\text{-}ref} = 40{-}50$ kHz, that is only weakly dependent on D. However, the PL decay rate for the np-Au/nc-Si sample is highly dependent on D, its values varying in the range of 55−105 kHz. The blue triangles in Fig. 4.17 show the experimental decay rate enhancement, $\eta_{\Gamma_{exp}}(D)$, as a function of D. This ratio is greater than unity for all D, and it reaches its maximum at 7.5 nm $< D <$ 12.5 nm, where it has a value of ~ 2. Interestingly, the enhancement of experimental decay rate roughly equals the increase in excitation cross section, in such a way that the two cancel each other out in Eq. (4.5), giving as a result no net contribution to the PL intensity enhancement. Therefore, to explain the experimentally observed four-fold PL intensity increase, we deduce that the nc-Si radiative emission rate, Γ_{rad}, must also increase in the vicinity of a np-Au film.

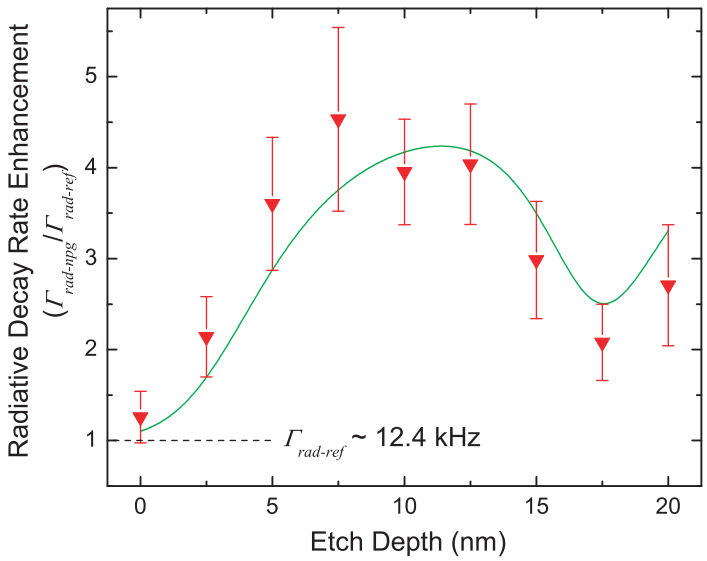

Figure 4.18: Radiative decay rate enhancement, $\eta_{\Gamma_{rad}}$, calculated with Eq. (4.5) for nc-Si emitting at 780 nm coupled to the np-Au film. The solid line is a fit to the data using the model described in Appendix B, which accounts for the spatial distribution of Si nanocrystals and the decay of the enhanced local field.

We measured Γ_{exp} at $P_{ex} = 50$ mW/mm^2, and σ was calculated using values of τ_{on} acquired at $5 < P_{ex} < 100$ mW/mm^2. At these pump powers, $\sigma\phi \simeq 10^2$–10^3 s^{-1} $\ll \Gamma_{exp} \simeq 5 \times 10^4$ s^{-1}. Thus we use Eq. (4.5), together with the measured enhancements η_{PL}, η_σ, and $\eta_{\Gamma_{exp}}$ reported in Figs. 4.13, 4.15, and 4.17, respectively, to estimate $\eta_{\Gamma_{rad}}$ directly for the nc-Si emitting at 780 $\pm$ 20 nm. The results of this exercise are reported as inverted triangles in Fig. 4.18. The enhancement $\eta_{\Gamma_{rad}}$ depends strongly on D, in particular it is greater than unity at all separation distances with a peak of ~ 4.5 at $D = 7.5$ nm. Indeed, this value suggests that the increase in radiative decay rate reported in Fig. 4.18 is uniquely responsible for the observed enhancement in PL intensity in Fig. 4.13.

On the basis of such an analysis, it is possible to give a quantitative estimate of the absolute values of the radiative rate, and therefore the quantum efficiency, of the nc-Si system. The enhancement in quantum efficiency, $\eta_Q = Q_{npg}/Q_{ref}$, is

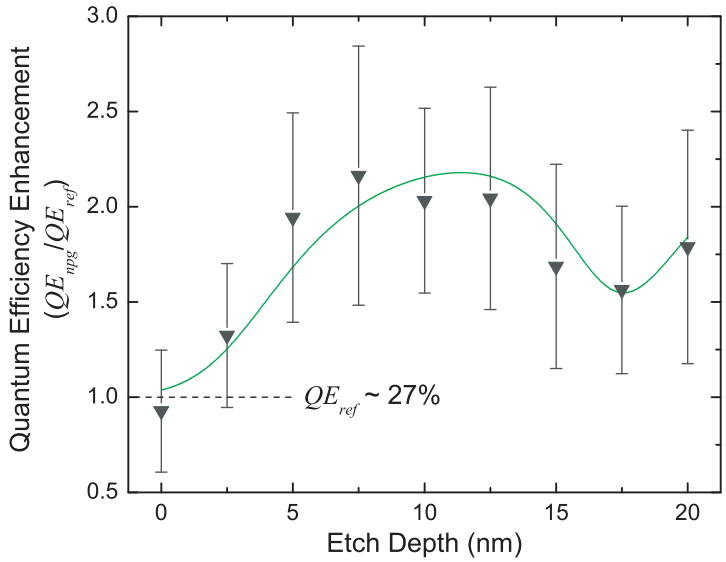

Figure 4.19: Quantum efficiency enhancement, η_Q, for nc-Si emitting at 780 nm and coupled to the np-Au film, as calculated using Eq. (4.8). The solid line is a fit to the data using the model described in Appendix B, which accounts for the spatial distribution of Si nanocrystals and the decay of the enhanced local field.

a function of the decay rate enhancements, i.e.,

$$\eta_Q = \frac{Q_{npg}}{Q_{ref}} = \left(\frac{\Gamma_{rad\cdot npg}}{\Gamma_{exp\cdot npg}} \cdot \frac{\Gamma_{exp\cdot ref}}{\Gamma_{rad\cdot ref}}\right) = \frac{\eta_{\Gamma_{rad}}}{\eta_{\Gamma_{exp}}} \tag{4.8}$$

The inverted triangles in Fig. 4.19 show η_Q, as calculated from Eq. (4.8) using the data for $\eta_{\Gamma_{exp}}$ and $\eta_{\Gamma_{rad}}$ reported in Figs. 4.17 and 4.18. The enhancement in quantum efficiency is dependent on D and has a peak of ~ 2 for 5 nm $< D <$ 12.5 nm.

From the definitions of the radiative and experimental rate enhancements, it follows that

$$\eta_{\Gamma_{rad}} = \eta_{\Gamma_{exp}} \cdot \left(\frac{\Gamma_{exp\cdot ref}}{\Gamma_{rad\cdot ref}}\right) - \left(\frac{\Gamma_{nr\cdot npg}}{\Gamma_{rad\cdot ref}}\right) \tag{4.9}$$

Here, $\Gamma_{nr\cdot npg}$ is the non-radiative decay rate of the coupled sample. Because for the reference sample, $\Gamma_{exp\cdot ref} = \Gamma_{rad\cdot ref} + \Gamma_{nr\cdot ref}$ is constant as a function of etch depth D, we can reasonably assume that $\Gamma_{rad\cdot ref}$ and $\Gamma_{nr\cdot ref}$ are also constant. Moreover, assuming that $\Gamma_{nr\cdot npg}$ is also approximately constant with D, a plot

of $\eta_{\Gamma_{rad}}$, shown in Fig. 4.18, versus $\eta_{\Gamma_{exp}}$, reported in Fig. 4.17, should give a straight line, according to Eq. (4.9). In Fig. 4.20, the experimental values of $\eta_{\Gamma_{rad}}$ and $\eta_{\Gamma_{exp}}$ are reported in a scatter graph. The trend is clearly linear, and indeed the data are very well fit (reduced $\chi^2 = 0.14$) by a straight line with slope, $(\Gamma_{exp\cdot ref}/\Gamma_{rad\cdot ref}) = 3.70 \pm 0.90$, and y-intercept, $(-\Gamma_{nr\cdot npg}/\Gamma_{rad\cdot ref}) = -3.33 \pm 0.82$. From this slope, and the measured value, $\Gamma_{exp\cdot ref} \sim 45$ kHz, we find for the reference sample that $\Gamma_{rad\cdot ref} \sim 12.4$ kHz, as indicated by the dashed line in Fig. 4.18. This measurement, corresponding to a radiative lifetime of 80 μs, is in good agreement with the values estimated for Si nanocrystals in this size regime by Garcia and coworkers,[91] and within the range calculated by Delerue et al.[94] The value of Q_{ref} for the reference sample is the inverse of the slope, i.e., 27%, as indicated by the dashed line in Fig. 4.19. From this value and the values of η_Q in Fig. 4.19, we estimate a peak enhanced quantum efficiency of 58% for nc-Si coupled to the nanoporous gold layer.

The overall luminescence intensity enhancements, at 780 nm and integrated over the entire spectrum, are consistent with the observed enhancements in σ and Γ_{rad}, as well as Γ_{exp}. Indeed, we found that $\Gamma_{exp\cdot npg}/\Gamma_{exp\cdot ref} > 1$ for all the separation distances D, as shown in Fig. 4.17. In principle, the presence of np-Au can determine the increase in Γ_{exp} by enhancing both the radiative and non-radiative decay channels. Here we want to investigate the relative importance of the two recombination paths in more detail. The radiative decay rate is enhanced by a factor of 4, as shown in Fig. 4.18, likely because of the increased local density of states related to the presence of the np-Au film in proximity to the optically active Si nanocrystals. As far as the non-radiative decay rate is concerned, for the reference sample we find $\Gamma_{nr\cdot ref} = (\Gamma_{exp\cdot ref} - \Gamma_{rad\cdot ref}) = 32.6$ kHz. For the np-Au/Si nanocrystal coupled sample, using the y-intercept of the straight line that best fits the data in Fig. 4.20, i.e., $(-\Gamma_{nr\cdot npg}/\Gamma_{rad\cdot ref}) = -3.33$, and using the value of $\Gamma_{rad\cdot ref} = 12.4$ kHz calculated above, we find $\Gamma_{nr\cdot npg} = 41.3$ kHz. This is indeed slightly greater than the reference value, meaning that the introduction of some novel non-radiative decay paths for the Si nanocrystals by the np-Au film

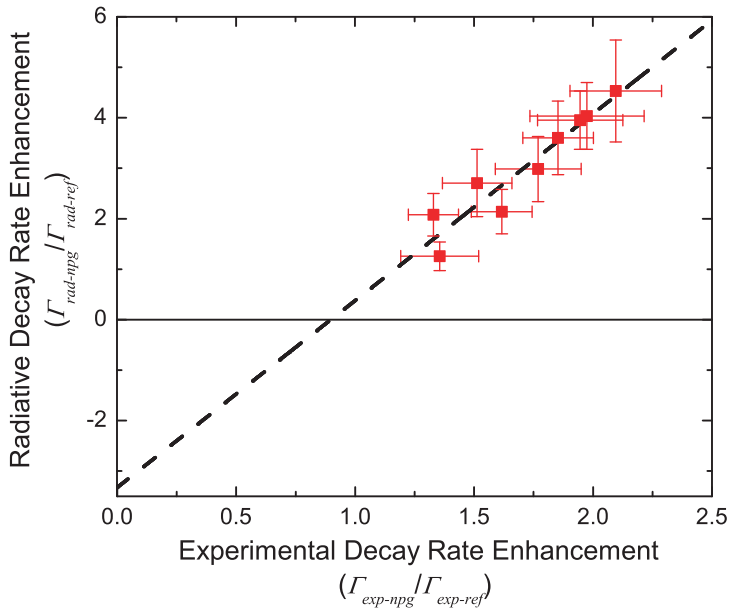

Figure 4.20: The decay rate enhancements, $\eta_{\Gamma_{rad}}$ and $\eta_{\Gamma_{exp}}$, are compared and fit to a straight line (reduced $\chi^2 = 0.14$) as in Eq. (4.9). The slope, $(\Gamma_{exp\cdot ref}/\Gamma_{rad\cdot ref}) = 3.70 \pm 0.90$, indicates a radiative rate, $\Gamma_{rad\cdot ref} \sim 12.4$ kHz, and a quantum efficiency of $Q_{ref} \sim 27\%$ for the reference sample. The y-intercept, $(-\Gamma_{nr\cdot npg}/\Gamma_{rad\cdot ref}) = -3.33 \pm 0.82$, is indicative of a coupled sample non-radiative rate, $\Gamma_{nr\cdot npg} \sim 41.3$ kHz.

cannot be fully neglected.

4.5 Conclusions

In conclusion, the coupling of silicon nanocrystals to nanoporous gold gives rise to up to eight-fold enhancements in photoluminescence intensity. Even at low pump powers, we find that coupling nc-Si to np-Au at optimal separation distances yields a four-fold enhancement in PL intensity at a detection wavelength of 780 nm, which was shown to be related to a four-fold enhancement in radiative decay rate as a result of local-field effects. The effective excitation cross section and the system quantum efficiency are enhanced by a factor of 2. These enhancements are especially promising considering that, here with a wide distribution of nc-Si, they contain contributions from a large number of far away unenhanced nanocrystals, which limits the overall achievable emission enhancement. Also, most nanocrystals are not resonant with the np-Au in the present work.

The techniques of the present chapter are particularly significant as they can be used for more general purposes than determining enhancement factors; in Section 4.4.4, we demonstrate that one can use the depth-dependent enhancement measurements to quantify the radiative decay rate and quantum efficiency, two quantities that are traditionally very difficult to evaluate.[24] We determine that, in the uncoupled reference sample, $\Gamma_{rad\cdot ref} \sim 12.4$ kHz, a true measure of the excitonic recombination dynamics that is not obvious from the straightforward measurement of the reference sample experimental decay rate, $\Gamma_{exp\cdot ref} \sim 45$ kHz. Also, we determine that the quantum efficiency of the reference sample of silicon nanocrystals in fused silica is $Q_{ref} \sim 27\%$. The two-fold enhancement in Q therefore brings the system's effective quantum efficiency to well over 50%, a very promising value. The initially high quantum efficiency, however, limits the extent to which plasmon coupling can enhance the overall emission; this quantity can of course never exceed 100%.

In spite of the complex structure of the nanoporous gold and the non-resonant

nature of the interactions, an analysis of the results of this chapter in the context of a model that we describe in Appendix B indicates that, with an optimized nanostructured sample consisting of a single, uniform (straggle $\lesssim$ 1 nm) monolayer of nc-Si resonant with np-Au, we can envisage enhancements in radiative decay rate, absorbance cross section and quantum efficiency, and therefore in PL intensity, by as much as two orders of magnitude. Such an increase in Si nanocrystal emission rate would make nc-Si competitive with direct band gap light emitters, enable us to fabricate brighter Si nanocrystal LEDs, and possibly even permit optical gain in an all-silicon device fabrication process.

Chapter 5

Spectrally Tunable Silicon Nanocrystal Emission from Coupling to Regular Silver Nanoparticle Arrays

5.1 Introduction

Since the observation in 1990 of strong room-temperature photoluminescence from porous silicon,[4,5] significant worldwide interest has been directed toward silicon-based photonics for integrated optoelectronics. An integral part of such systems is a Si-based, power-efficient light emitter. Toward that end, silicon nanocrystals (nc-Si) have been intensively investigated as light sources. In the previous chapter, we observed enhanced photoluminescence intensity, absorbance cross section, radiative decay rate, and quantum efficiency from nc-Si coupled to nanostructured gold. The possibility of obtaining enhanced emission, and, in particular, of achieving enhanced radiative decay rates upon coupling radiative dipole emission to metal nanostructures provides an opportunity to use nc-Si, already an inherently efficient light emitter, as a bright, competitive light source. This increased radiative emission has been attributed to electromagnetic coupling between the semiconductor active dipole emitters and surface plasmons in the metal,[61] an effect that is predicted to be stronger at frequencies near the plasmon resonance. We therefore seek to examine the resonant nature of the enhancement effect introduced

in Chapter 3.

In the present chapter, we report an enhancement of photoluminescence (PL) in systems of nc-Si coupled to silver nanoparticle arrays fabricated by electron-beam lithography. Silver was chosen to give the strongest possible plasmonic effects, because this noble metal suffers the least from Ohmic losses and produces the strongest resonances among all metals with plasmon resonances at visible frequencies. The surface plasmon resonance of arrays of Ag nanoparticles (np-Ag) depends on the particle diameter and the array pitch, and can thus be tuned by adjusting these parameters. When the surface plasmon resonance of the np-Ag arrays is tuned throughout the nc-Si emission spectrum, we observe a significant correlation between the frequency at which the PL emission is enhanced and the surface plasmon resonance frequency. This is a strong indication that the enhancement process is a resonant one. From the observed behavior, we can further conclude that the observed PL enhancement is caused by an enhancement of the radiative decay rate of the nc-Si.

5.2 Theory

The nanoporous gold (np-Au) to which nc-Si was coupled in Chapter 4 has a very broad extinction spectrum, as was shown in Fig. 4.8. That spectrum was the result of the very broad distribution of features in the np-Au film. These shapes range from sphere-like Au particles to elongated rods with aspect ratios of up to $\sim$ 4:1. According to Mie-Gans theory, the broad extinction spectrum in Fig. 4.8 is consistent with absorbances from such a wide distribution.[80] Nanoporous gold is therefore not an ideal material with which to take advantage of resonant effects.

In the present chapter, we therefore make use of arrays of silver nanoparticles. The plasmon resonance frequency of a cylindrical Ag nanoparticle is principally determined by the aspect ratio, i.e., the ratio of the diameter to the height. As the nanoparticle size becomes comparable to the wavelength of light, the particle size also affects the plasmon resonance frequency, although radiative losses and

retardation effects are secondary factors. Finally, as discussed in Chapter 3, when the np-Ag are arranged in arrays, the extent of coupling between adjacent particles strongly influences the plasmon resonance frequency of the array. Such coupling can be tuned via changes in the interparticle spacing.

5.3 Experimental

5.3.1 Sample Fabrication

Silicon Nanocrystal Formation

As in the previous chapter, silicon nanocrystals (nc-Si) were produced by ion implantation of 11 keV Si^+ ions to a fluence of 1.7×10^{16} cm^{-2} into a 1.6 mm thick fused quartz strip (Technical Glass Products). The implanted quartz was annealed in Ar for 20 min at each of 200 and 450 °C, and then for 30 min at 1000 °C to form nc-Si with typical diameters of 3−5 nm.[41] The samples were subsequently heated in a forming gas (10% H_2, 90% N_2) for 30 min at 450 °C to eliminate emission from defect states in the SiO_2 matrix.[42] This protocol was determined in Section 4.4.2 to yield a Gaussian depth distribution of nc-Si in the SiO_2, with a peak concentration at a depth of 19.2 nm. After nc-Si formation, the center of the nanocrystal distribution was brought to a depth, Δ, of 8, 13, or 18 nm from the surface by etching in 2.3% HF(aq). The etch rate was 0.25 nm/s, as determined by spectroscopic ellipsometry (Sentech SE-850) on an analogous sample of SiO_2 on a Si substrate. As was described in Section 4.4.1 of Chapter 4, ellipsometry also indicated that after etching, the surface roughness was less than ± 0.2 nm.

Electron-Beam Lithography Patterning of Silver Nanoparticle Arrays

To investigate resonant plasmonic effects, the nc-Si-doped SiO_2 was coupled to np-Ag arrays. The surface of the nanocrystal-doped quartz was cleaned for 20 min in a 5:1:1 H_2O:H_2O_2:NH_4OH solution at 70 °C. Figure 5.1 illustrates the sequence by which the clean nc-Si-doped silica sample (Fig. 5.1(a)) was patterned by electron-beam lithography. A first layer of 2% in chlorobenzene 495 K molecular weight

(MW) polymethyl methacrylate (PMMA) was spun on the sample surface at 750 rpm for 5 s, then 2500 rpm for 45 s. This layer was polymerized by baking at 175 °C for 90 s, yielding a resist layer 70 nm thick, as verified by profilometry. A second layer of 2% 950 K MW PMMA was spun on top of the first layer. This heavier resist layer was spun at 750 rpm for 5 s, then 4000 rpm for 45 s, and baked at 175 °C for 90 s. Profilometry indicated the total thickness of the two layers to be 145 nm. Such a bilayer resist system has been previously shown to improve liftoff in electron-beam lithography by making use of the different sensitivities of the layers to the electron beam.[95] Following this spinning and annealing, a 17 nm layer of Ge was deposited on top of the PMMA double layer by thermal evaporation to provide a conductive target for the electron beam. The resulting stack is shown in Fig. 5.1(b). An electron beam with current ~ 150 pA was next used to pattern 100 μm $\times$ 100 μm arrays of circles in the Ge-coated PMMA resist, as schematized in Fig. 5.1(c). The top Ge layer was removed by reactive-ion etching (RIE) in a 50% CHF, 50% Ar plasma for 20 s, and the exposed PMMA bilayer was developed in a 1:2 mixture of 4-methyl-2-pentanone (MIBK) and isopropyl alcohol. As illustrated in Fig. 5.1(d), the lower molecular weight PMMA layer on the bottom is more sensitive to the electron beam, and thus upon developing this layer an undercut evolves. In an ultra-high-vacuum (UHV) electron-beam evaporation chamber, a 2 nm Si wetting layer and a 20 nm Ag layer were deposited onto the structure. The resultant sample, in Fig. 5.1(e), was finally exposed to acetone for PMMA liftoff, leaving the np-Ag arrays on nc-Si-doped fused silica shown in cross section in Fig. 5.1(f).

5.3.2 Physical Characterization of the Silver Nanoparticle Arrays

Upon liftoff of the resist bilayer, the resulting structure is composed of cylindrical Ag nanoparticles in arranged a 100 μm $\times$ 100 μm square lattice, as sketched in Fig. 5.2. The electron-beam exposure in Section 5.3.1 was chosen to produce circular arrays with controllable pitch, p, in the range of 200$-$500 nm, and the particle diameters, d, were controlled by adjusting the electron beam dwell time

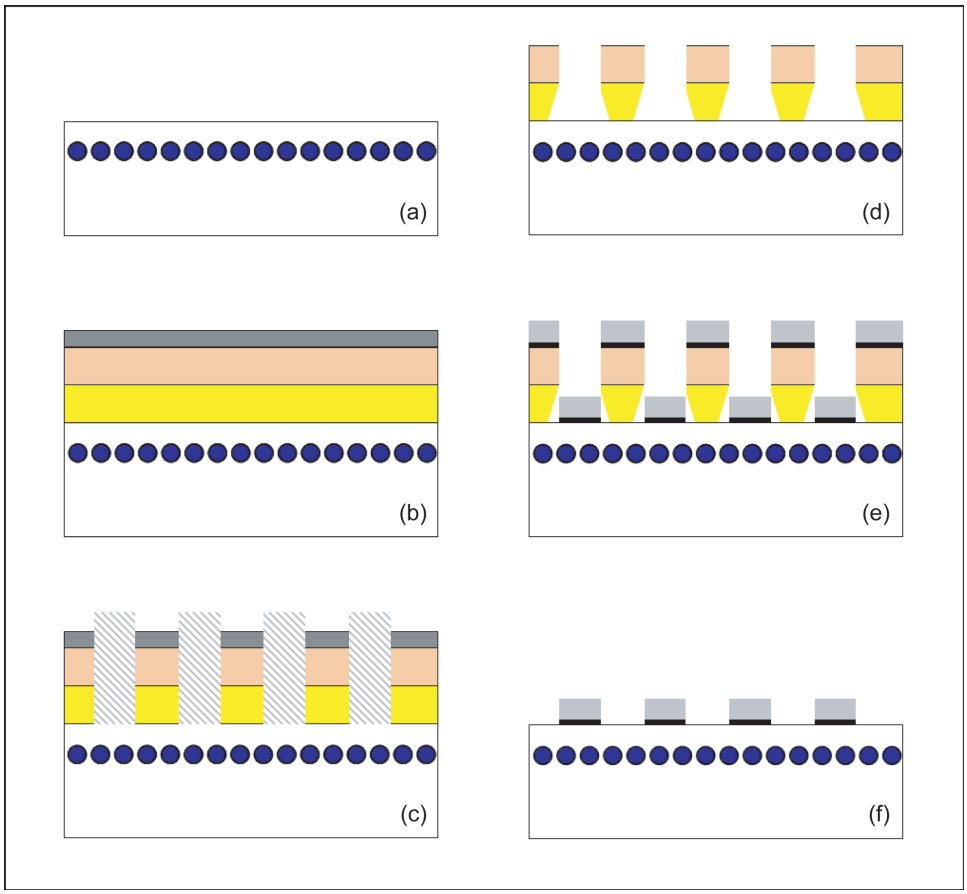

Figure 5.1: Schematic of the electron-beam lithography process for creating silver nanoparticle arrays. (a) Si nanocrystal (nc-Si)-doped fused silica. (b) nc-Si-doped fused silica coated with 70 nm of 495 K MW PMMA, 75 nm of 950 K MW PMMA, and 17 nm of Ge. (c) Exposure of the stack with an electron beam. (d) After removal of the Ge top layer by RIE, the PMMA bilayer is developed in MIBK, and an undercut evolves in the lower molecular weight layer. (e) UHV electron-beam evaporation of 2 nm Si and 20 nm Ag. (f) Liftoff of the resist leaves behind Ag nanoparticles adhered to the nc-Si-doped silica via a 2 nm Si adhesion layer.

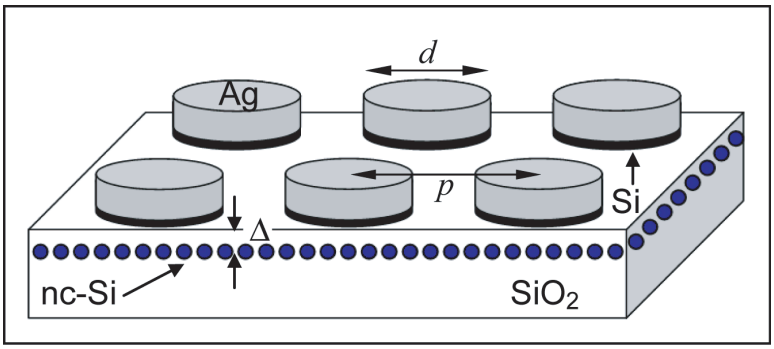

Figure 5.2: Schematic of the sample consisting of Si nanocrystals (nc-Si) separated from arrays of silver nanoparticles (np-Ag) by a distance, Δ. Each Ag nanoparticle has a height, $h = 20$ nm, a diameter, d, and sits on a 2-nm-thick Si adhesion layer. The nanoparticles are arranged in square lattices with pitch, p.

for each array. The diameters could not be predicted accurately, so scanning electron microscopy (SEM) was utilized to determine the exact diameters of the cylinders in each array after fabrication. To compensate for the presence of the insulating silica substrate, a low voltage (2.5 kV) SEM beam was utilized.

5.3.3 Optoelectronic Characterization

Measurements of Array Resonances via Transmission Spectroscopy

Each array of np-Ag with height $h = 20$ nm was characterized by a distinct pitch, p (200−500 nm), particle diameter, d (100−440 nm), and thus particle aspect ratio, $a = d/h$ (5−22). As a consequence of these geometric differences, the arrays had distinct plasmon resonance frequencies,[80] which were determined by measuring the transmission spectrum through each np-Ag array. For the transmission measurements, the arrays were illuminated with a white light source incident through a 60× microscope objective. The lamp used for this purpose provides strong illumination between 400 and 900 nm; its spectrum peaks at $\sim$ 620 nm and has a full-width at half maximum of $\sim$ 200 nm. The transmitted light was collected with a 20× microscope objective.

The spectral transmittance through each array of np-Ag on top of nc-Si-doped fused silica was normalized by the transmittance through a nearby region devoid

of np-Ag. Relative to the np-Ag, the silicon nanocrystals have an extremely limited absorbance cross section. Regardless, any contribution from the nc-Si was explicitly removed by the normalization.

Photoluminescence Spectroscopy to Characterize the Nanocrystal Emission

Photoluminescence (PL) spectra were acquired under excitation from a frequency-doubled Nd:YAG (yttrium aluminum garnet) laser operating at $\lambda_{ex} = 532$ nm focused through a microscope objective to a 10 μm diameter spot. A relatively high pump power of $P_{ex} = 10^5$ mW/mm^2 was used to ensure operation near the saturated pump power regime, where the PL emission is limited by the radiative decay rate and is independent of the quantum efficiency.

The PL intensity was recorded using a thermoelectrically cooled charge-coupled device (CCD) detector (sensitivity range 200−1100 nm) in conjunction with a 30 cm focal length grating spectrograph. A dichroic filter that absorbs wavelengths below 550 nm was used to eliminate incident laser light from the detector. For the sample schematized in Fig. 5.2, Si nanocrystal excitation and PL emission collection were both performed through the "top" (np-Ag array) side and through the "back" (quartz substrate) side of the sample. All combinations of these geometries gave similar results for the enhancement magnitude and spectral dependence, indicating that the Si/Ag system was acting as a coupled entity. Since these different configurations gave no consistent differences in PL, measurements made in the different configurations were averaged to improve the statistics. Reference luminescence spectra were obtained for each array from a nearby region of nc-Si-doped quartz not located under a np-Ag array.

5.4 Results and Discussion

5.4.1 Scanning Electron Microscopy of the Silver Nanoparticle Arrays

Scanning electron microscopy (SEM) was used to examine the Ag nanoparticle arrays of this chapter. The characteristic particle diameter in each sample was determined by finding the average width in SEM of ≥ 25 particles in each image. 1.75 μm $\times$ 1.3 μm subsections of the SEM images of one series of np-Ag arrays are displayed in Fig. 5.3. These micrographs show a progression of arrays with a constant 400 nm pitch and increasing particle sizes. The average diameters in these samples, indicated on each panels of this figure, are 135, 140, 165, 185, 190, 230, 260, and 320 nm, respectively.

From the SEM images, it was also possible to identify series of Ag nanoparticle arrays with constant particle diameters. In Fig. 5.4, we present one such series. Here, the particles all have 165 nm diameters, and the arrays have increasing pitches, $p = 200$, 300, 400, and 500 nm, as indicated on the respective panels.

5.4.2 Measurements of Enhanced Photoluminescence

For the PL measurements in the present chapter, we targeted the high pump power regime, where the PL emission is limited by the radiative decay rate and is independent of quantum efficiency. The PL intensity is in general given by

$$I_{PL} \propto \frac{\sigma\phi}{\sigma\phi + \Gamma_{exp}} \cdot n \cdot \Gamma_{rad} \tag{5.1}$$

where the PL intensity, I_{PL}, depends on the number of nanocrystals, n; the excitation cross section, σ; the pump flux, ϕ; the radiative decay rate, Γ_{rad}; and the experimental decay rate, $\Gamma_{exp} = \Gamma_{rad} + \Gamma_{nr}$. However, in the high-excitation regime, where $\sigma\phi \gg \Gamma_{exp}$, Eq. (5.1) reduces to

$$I_{PL} \propto n \cdot \Gamma_{rad} \quad (\sigma\phi \gg \Gamma_{exp}) \tag{5.2}$$

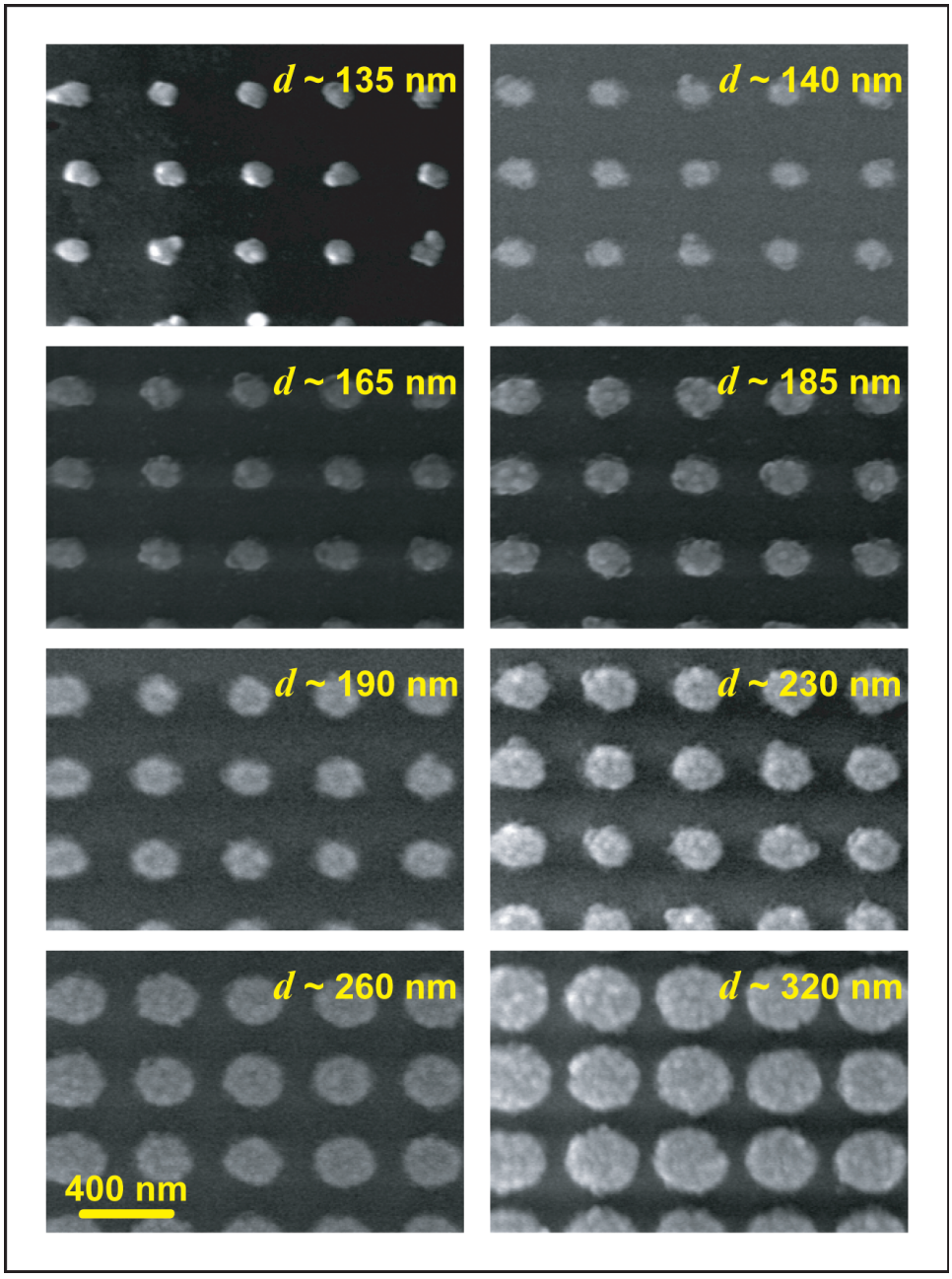

Figure 5.3: 1.75 μm $\times$ 1.3 μm SEM images at 38 400$\times$ magnification of a series of Ag nanoparticle arrays with $p = 400$ nm and $d = 135{-}320$ nm.

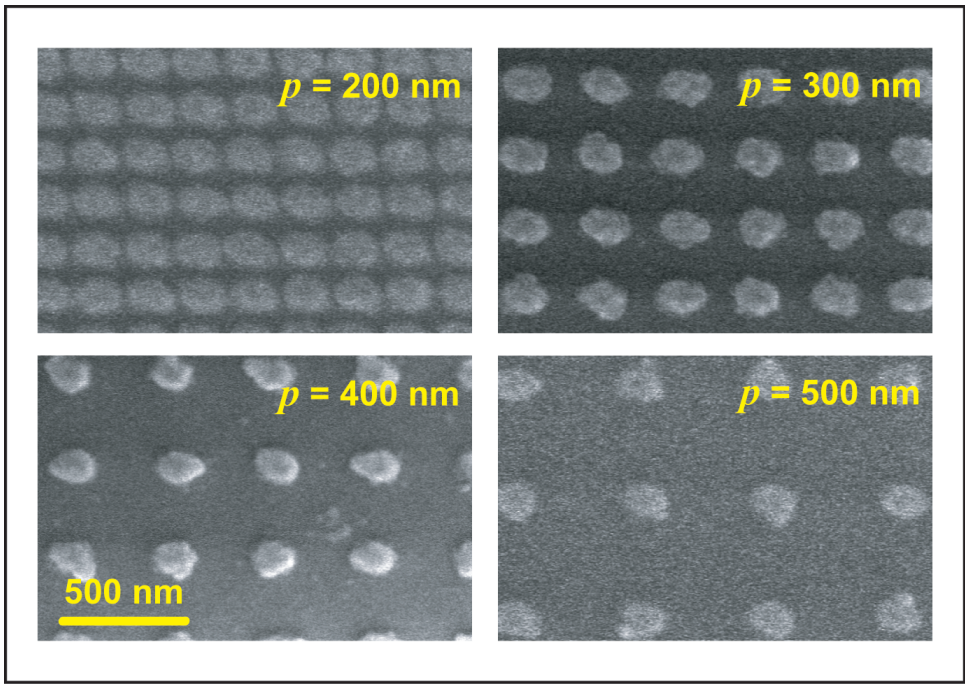

Figure 5.4: 1.6 μm $\times$ 1.2 μm SEM images at 38 400$\times$ magnification of a series of Ag nanoparticle arrays with $d = 165$ nm and $p = 200-500$ nm.

This regime of high excitation powers is also the regime of near-saturated photoluminescence, where increases in pump power have little effect on the intensity of PL emission. We verified that we were in the near-saturated regime by measuring the PL intensity, integrated from $\lambda = 650-950$ nm, as a function of pump power, P_{ex}. The results for the reference sample (no Ag nanoparticles) and a representative coupled nc-Si/np-Ag sample are displayed in Figs. 5.5(a) and (b), respectively. Here, the PL intensity is highly dependent on P_{ex} for low powers, but increases in PL intensity with P_{ex} are more subtle at higher powers. As indicated by the arrow in Fig. 5.5, the pump power used in the present chapter, $P_{ex} = 10^5$ mW/mm^2, falls within the near-saturated emission regime.

To check for PL signal uniformity over the range of the 100 μm$\times$100 μm particle arrays, as well as over the range of the Ag-free reference areas, the samples were mounted on a translation stage and the PL intensity, integrated from $\lambda = 640-950$ nm, was measured in 10-μm steps. Figure 5.6(a) shows a single np-Ag array, as seen

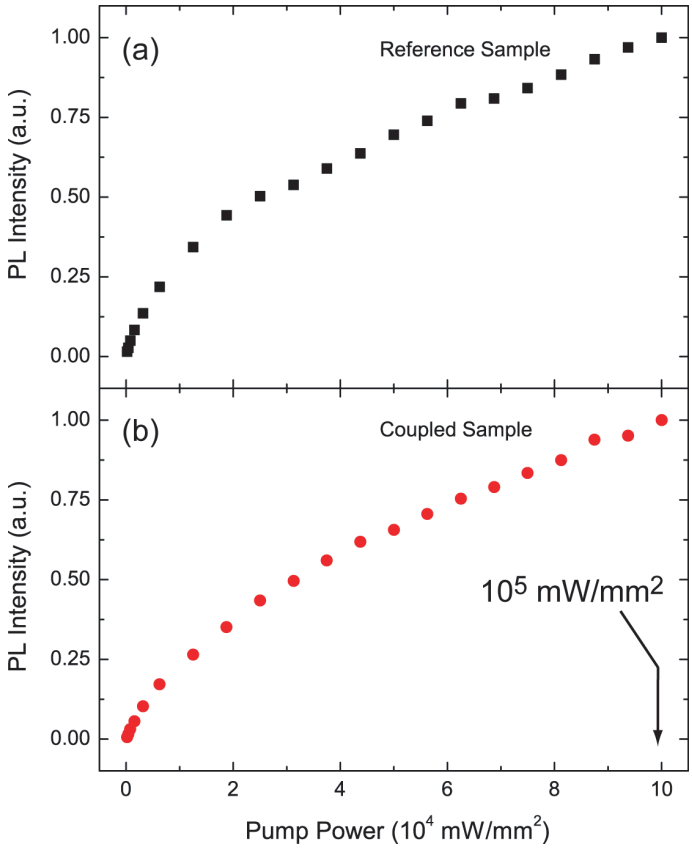

Figure 5.5: Photoluminescence intensity of (a) the reference sample and (b) a representative coupled sample as a function of pump power. The arrow indicates the 10^5 mW/mm^2 pump power at which the experiments in the present chapter were performed.

in the 60× microscope objective used for PL excitation. Here, the array occupies the image center. The results of a two-dimensional PL scan of this sample, which has $d = 320$ nm, $p = 400$ nm, and $\Delta = 8$ nm, is shown in Fig. 5.6(b). The PL intensity emitted from the array region was approximately twice that emitted from the uncoupled nanocrystals in the reference areas, and the PL intensity was essentially constant with position in both areas. The spatial resolution of this measurement was not sufficient to identify differences in PL intensity at length scales smaller than the pitch.

Figure 5.7 shows the correspondence between the spectral position and shape of the nc-Si PL enhancement and the surface plasmon resonance of a typical coupled np-Ag array/nc-Si system ($d = 190$ nm, $p = 400$ nm, and $\Delta = 13$ nm). The normalized transmission spectrum of the array is shown in Fig. 5.7(a). This spectrum exhibits a dip centered at 710 nm that is attributed to extinction due to the resonant excitation of dipole plasmon modes in the Ag nanoparticles. The photoluminescence spectrum was measured for the same sample. As is reported in Fig. 5.7(b), the PL intensity on the array, I_{arr}, was enhanced significantly compared to the nc-Si PL intensity in the reference area, I_{ref}, especially at wavelengths where the plasmon mode is resonant. Figure 5.7(c) shows the PL enhancement spectrum, $\eta_{PL}(\lambda) = I_{arr}(\lambda)/I_{ref}(\lambda)$. The enhancement spectrum features correspond strongly to those in the transmission spectrum; both curves peak at $\lambda = 710$ nm and have similar widths.

5.4.3 Resonantly Enhanced Emission

Figure 5.8 shows the normalized transmission and PL enhancement spectra of six samples with np-Ag arrays of fixed pitch and depth, $p = 400$ nm and $\Delta = 13$ nm. In this figure, the particle diameter increases from top to bottom panel, with $d =$ 165, 185, 190, 230, 260, and 320, respectively. As d is increased, the transmission dip grows larger in magnitude and shifts to larger wavelengths. The decreased transmission may be attributed to an increase in Ag coverage. The shift of the minimum transmission wavelength can be understood qualitatively as resulting

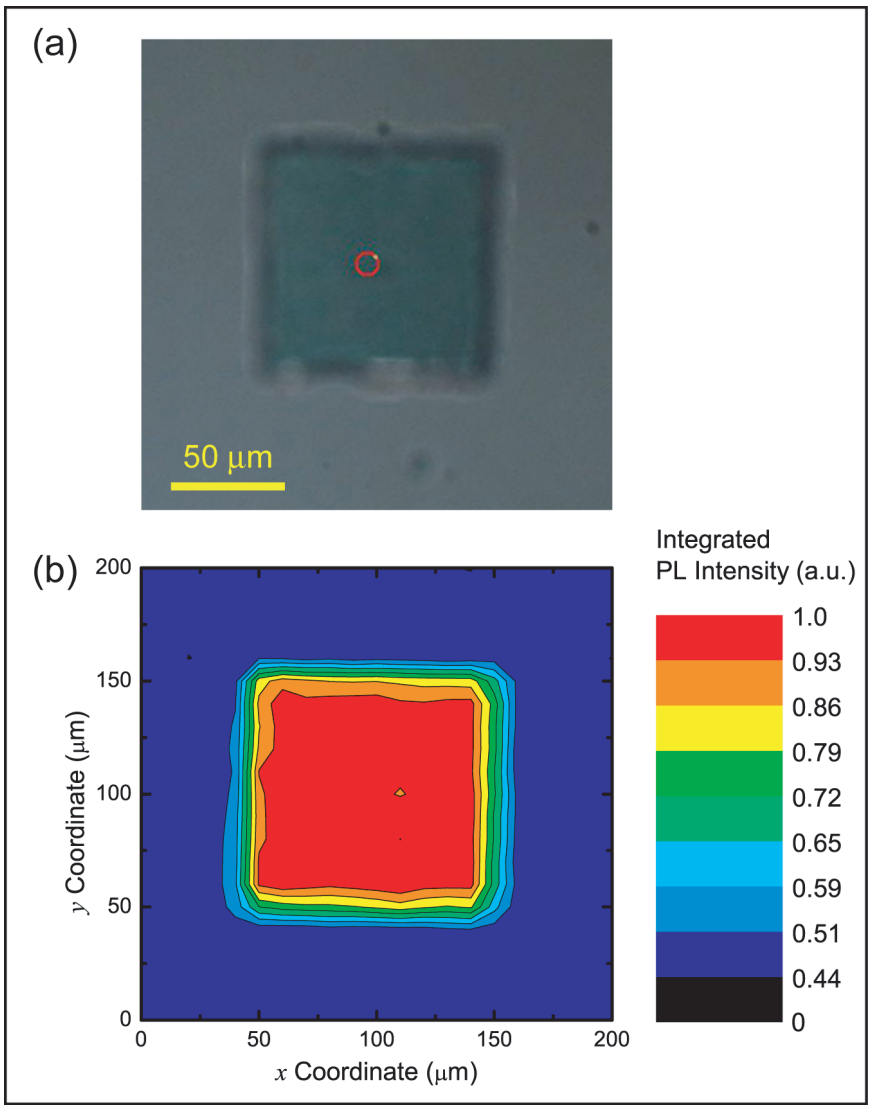

Figure 5.6: Characterization of a representative 100 μm $\times$ 100 μm np-Ag array (center) and the surrounding Ag-free region (periphery). (a) Image of the array through a 60$\times$ optical microscope objective. (b) PL intensity map in 10-μm steps, integrated from $\lambda = 640{-}950$ nm. Here, $p = 400$ nm, $d = 320$ nm, and $\Delta = 8$ nm.

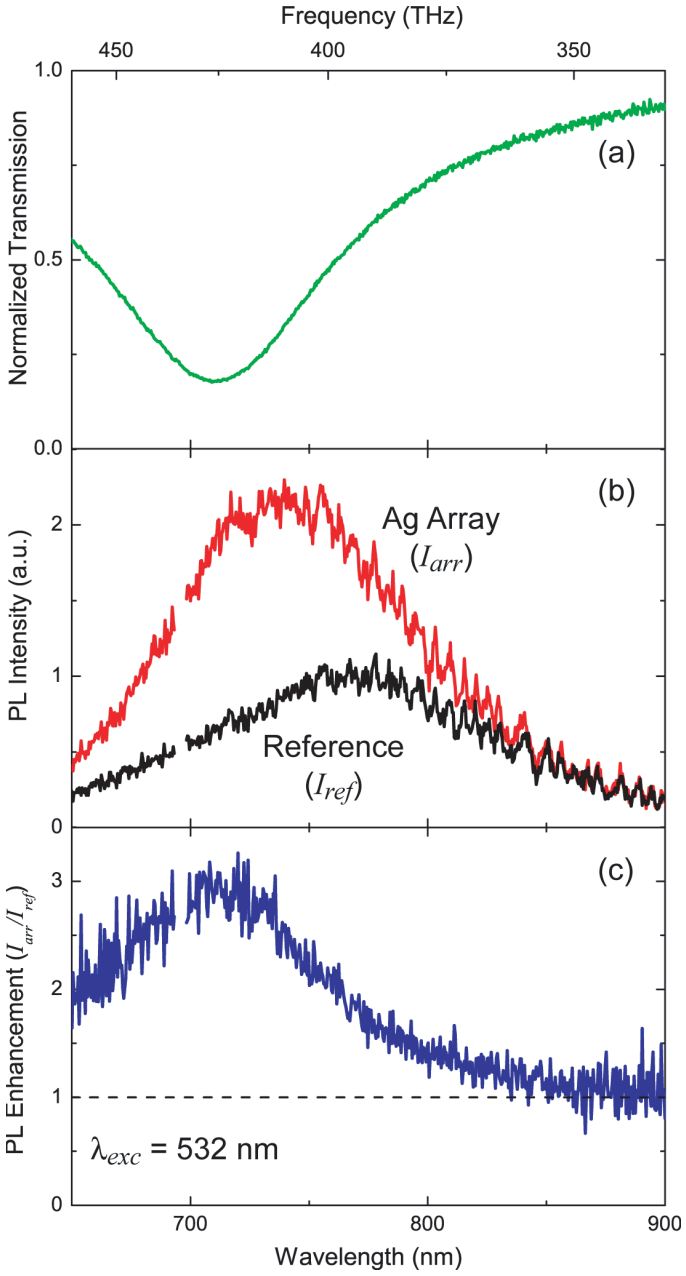

Figure 5.7: Optical characterization of a representative sample (p = 400 nm, d = 320 nm, and Δ = 13 nm). (a) Normalized transmission through the Ag nanoparticle array. (b) PL intensity from nc-Si in the absence (bottom curve) and presence (top curve) of np-Ag. (c) PL intensity enhancement in the coupled system (ratio of the curves in (b)).

from the increases in d (from 165 to 320 nm) and the concomitant increases in the aspect ratio, a (from 8 to 16), both of which are known to cause a red shift of the surface plasmon resonance in the plane of these arrays.[80]

The PL enhancement spectra (Fig. 5.8) exhibit a red shift with increasing d and a that is similar to the trend in transmission dips, establishing a strong correlation between the PL enhancement and the surface plasmon resonance. This correspondence is illustrated for 187 different samples in Fig. 5.9, in which the wavelength of minimum transmission is correlated with the maximum PL enhancement wavelength. The observed trend is well-fitted by a straight line with a slope of 0.97 $\pm$ 0.03 and a y-intercept of 14 $\pm$ 17 nm. Despite variations in Δ, p, and d, the 1:1 spectral correspondence between the nc-Si PL enhancement and the np-Ag array plasmon resonance indicates that the PL enhancement can be consistently ascribed to an increase in radiative decay rate due to the resonant coupling of the nc-Si with the collective surface plasmon dipole modes of the np-Ag. Furthermore, no luminescence enhancements were observed for samples that showed transmission dips resonant with the λ_{ex} = 532 nm excitation source, demonstrating that the increased PL intensity cannot be attributed to an increased absorption of the pump beam.

In the present chapter, we consider samples of nc-Si coupled to arrays of np-Ag. The periodic silver structure acts as a grating for emitted light, so when considering the magnitude of PL intensity enhancement in these samples, the array periodicity must be taken into account. The angle at which diffracted light is emitted depends on the array pitch and the emission wavelength. Thus, to compare samples of different pitches, the collection angle must be limited such that only the zeroth order diffracted beam is collected, or the emitted intensity must truly be integrated over all wavelengths to ensure that all diffracted orders are included. In our experiments, we select the former solution, and use a microscope objective with a limited angle of collection. Still, there is a risk of collecting emission from the first-order diffracted light, especially at small pitches, so the best way to examine PL intensity enhancement magnitudes is to compare the emission

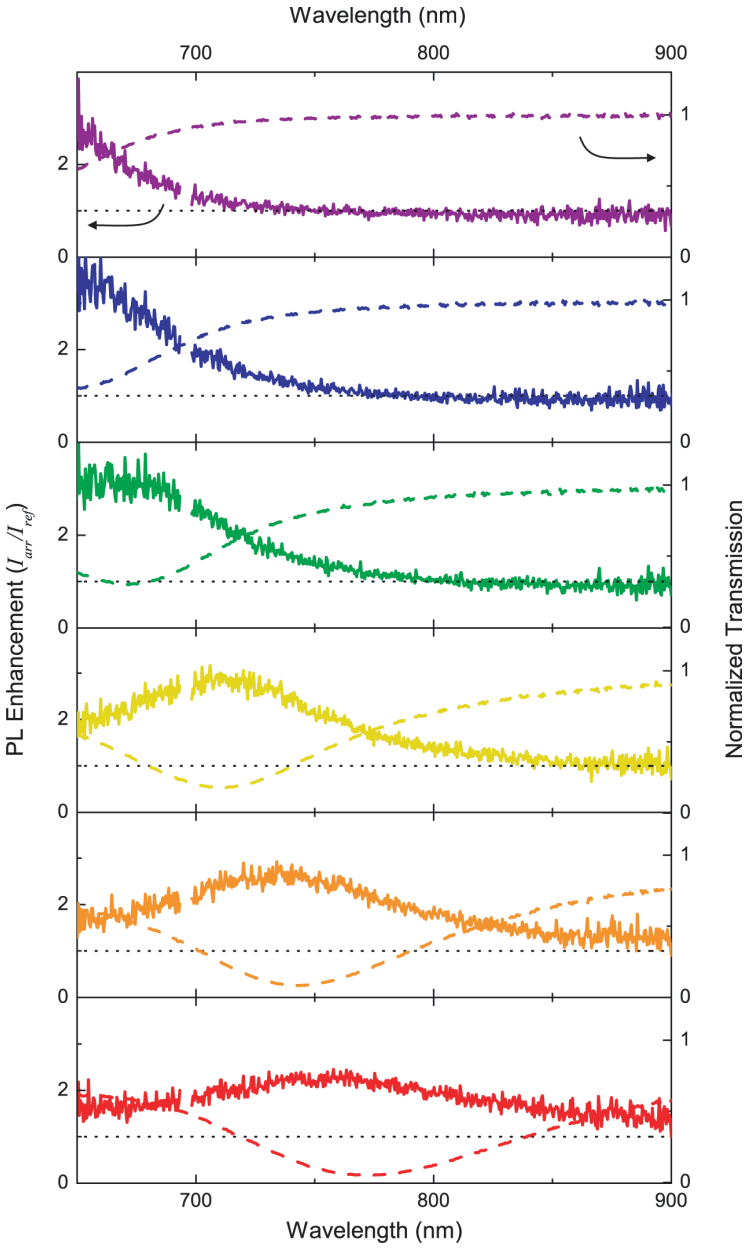

Figure 5.8: PL intensity enhancement (solid lines) and normalized transmission spectra (dashed lines) for samples with $p = 400$ nm and $\Delta = 13$ nm; d increases from the top to bottom panels, with $d = 165$, 185, 190, 230, 260, and 320 nm, respectively.

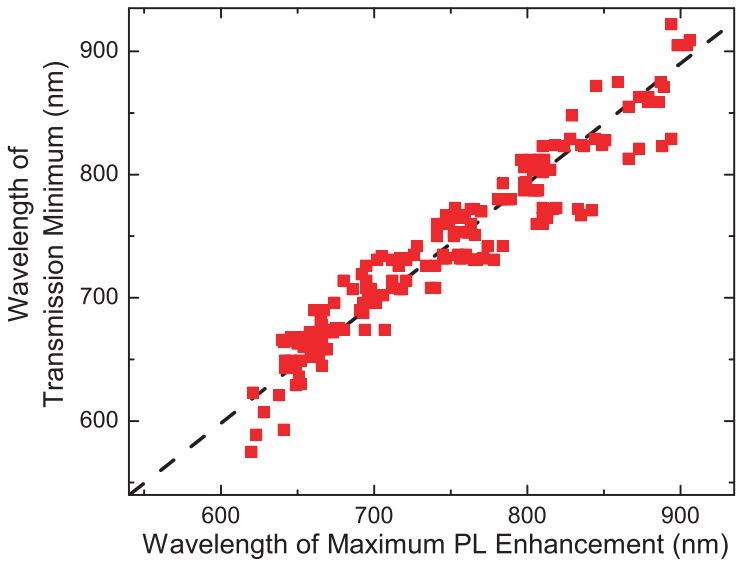

Figure 5.9: Correspondence between the wavelength of minimum transmission and the wavelength of maximum PL enhancement for 187 different samples. The dashed line is a best fit of the data to a straight line, $\lambda_{trans} = (0.97 \pm 0.03)\lambda_{PL} + (14 \pm 17)$.

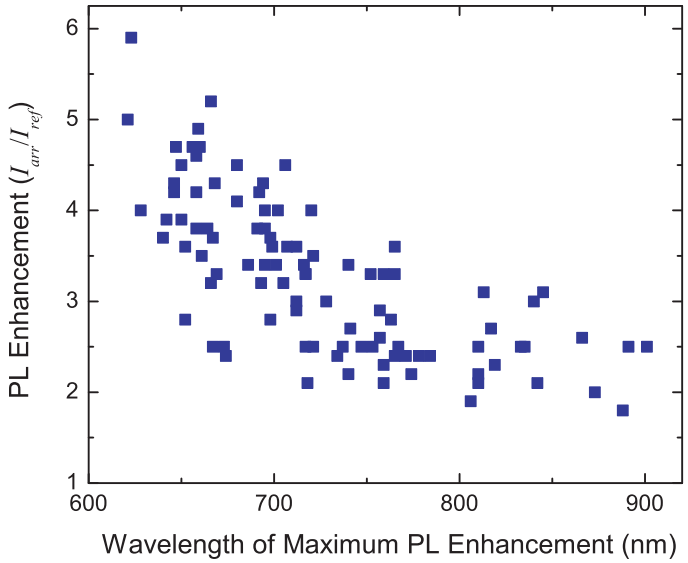

Figure 5.10: Comparison between the maximum magnitude of PL enhancement and the wavelength at which this maximum is reached for 97 different samples with 400-nm pitch.

from a series of samples with a constant pitch. Accordingly, Fig. 5.10 shows the magnitude of the maximum PL intensity enhancement as a function of wavelength for 97 different samples with 400-nm pitch. Coupling nc-Si to Ag nanoparticle arrays produces up to six-fold intensity enhancements. Furthermore, the greatest of these increases are observed at short emission wavelengths, where arrays of smaller nanoparticles are resonant. It is expected that only nc-Si positioned closer to Ag particles than the typical plasmon coupling range of ~ 50 nm will experience an enhanced emission rate.[61] It follows then that the number of Si nanocrystals coupled to Ag nanoparticles increases with particle coverage. The fact that a smaller overall PL enhancement is found for larger particles thus implies that the emission enhancement per Si nanocrystal must be greater near smaller Ag particles. This behavior is consistent both with trends in radiative damping of the excited plasmon mode and with trends in local-field enhancement as a function of particle size; the former, which limits the radiative decay rate enhancement, is more significant for larger nanoparticles,[96] while the local-field enhancement about a metal nanoparticle decreases with decreasing radius of curvature, i.e., with increasing particle size.[81] The samples considered in Fig. 5.10 have $d = 100{-}370$ nm and $\Delta = 8{-}18$ nm, yet the magnitude of enhancement was found to depend most strongly on d. This indicates that, in this regime of loosely coupled particles, the pitch has a more subtle influence, and that effects due to the Si/Ag separation distances were likely obfuscated by the large (~ 14 nm) spread in nc-Si depths about the average depth, Δ. We will explore all of these trends with full-field electromagnetic simulations in Chapter 6.

5.5 Conclusions

In conclusion, we have observed up to six-fold enhancements in the PL intensity of Si nanocrystals upon coupling them to Ag nanoparticle arrays. The enhancement can be spectrally controlled across the emission spectrum of the nc-Si by tuning the surface plasmon resonance frequency of the np-Ag between 600 and 900 nm.

This can be accomplished by varying the nanoparticle diameter and the array pitch. Coupling to engineered plasmonic structures thus provides an interesting approach to controlling the emission rate and the emission spectrum of silicon nanocrystals.

Chapter 6

Full-Field Electromagnetic Simulations of Enhanced Silicon Nanocrystals

6.1 Introduction

The interesting optoelectronic properties of semiconductor nanocrystals have attracted much attention in recent years. The energetics of these zero-dimensional quantum dots are unlike those of their bulk material counterparts, which makes them suitable for diverse and exciting applications ranging from biological sensing to light-emitting devices. Silicon nanocrystals (nc-Si) with dimensions below ~ 5 nm have proven to be efficient light emitters, with emission energies that are size-tunable throughout the visible spectrum. One important advantage of using these silicon light emitters is that they can be fabricated in a CMOS-compatible manner, for example by ion implantation. However, the overall brightness of nc-Si is limited by their slow decay rate, 10^4–10^5 s^{-1}, a result of the indirect band gap in silicon. A method for enhancing the overall brightness is therefore desirable.

As outlined in Chapter 3, an emitter in the intense local field near the surface of a metal particle or rough metal surface will demonstrate a modified radiative decay rate, quantum efficiency, and photoluminescence (PL) intensity.[61–63] Recent experimental studies have shown that increased emission from semiconductor quantum dots can be realized via plasmon enhancement interactions,[35,36] and in Chapters 4 and 5, we confirmed that this technique can be extended to the emission

of silicon nanocrystals by coupling them to nanoporous gold and silver nanoparticles, respectively. Unfortunately, in those studies, the ensemble measurements made using far-field measurement techniques obscured the more subtle details of the enhancement.

In the present chapter, we use full-field finite-integration time-domain studies to examine the near-field physics that give rise to our far-field experimental observations. By simulating systems analogous to those measured experimentally, we verify our interpretations of the three key experimental results of the previous chapter: (*1*) Measurements of transmission through arrays of cylindrical silver nanoparticles show a dip at the plasmon resonance frequency. This frequency depends on the particle diameter and the interparticle spacing, and it can be tuned throughout the nc-Si emission spectrum. (*2*) The $\lesssim$ six-fold enhancements in PL intensity of emitters $\sim$ 10 nm beneath the particles is due to a $\lesssim$ six-fold field intensity enhancement in their plane. (*3*) Given a constant pitch, a greater PL enhancement is observed for nc-Si coupled to smaller particles despite a lower particle coverage; this must result from very large peak local-field intensities about the small particles.

In addition to verifying the experimental results and interpretations (*1*)$-$(*3*), we can use electromagnetic simulations to probe effects that could not be resolved in our experiments. For example, the ion-implantation fabrication technique used to create the nc-Si gave rise to a large spread in their depths. In our computations, we can more precisely monitor how the magnitude of the enhanced field falls off with increased depth. As well, in our calculated results, we can identify the maximum field enhancement and map the field profile, rather than merely detecting the spatial average.

6.2 Theory

6.2.1 Photoluminescence Intensity Manipulations in an Enhanced Local Field

Recent studies have demonstrated enhanced photoluminescence from semiconductor quantum dots and quantum wells in close proximity to noble metal films and nanostructures.[35–37] This phenomenon of plasmon-enhanced light emission demonstrates that, by engineering the near-field coupling between semiconductor and metallic structures, the optically induced emission from semiconductor nanocrystals can be altered and enhanced. Here, we apply the theory of plasmon enhancement, introduced in Chapter 3, to nanocrystal photoluminescence. This analysis is done for the limiting case of high pump flux, the regime in which the measurements of Chapter 5 were made.

The PL intensity, I_{PL}, of a nanocrystal emitter is given by

$$I_{PL} = N\frac{\sigma\phi}{\sigma\phi + \Gamma_{exp}}\Gamma_{rad} \tag{6.1}$$

where N is the number of active emitters, σ is the absorbance cross section, ϕ is the excitation pump flux, Γ_{rad} is the radiative decay rate and the total decay rate, Γ_{exp}, is the sum of the decay rates along both radiative and non-radiative pathways. In the limit of a large pump flux, Eq. (6.1) becomes

$$I_{PL} = N\Gamma_{rad} \quad (\sigma\phi \gg \Gamma_{exp}) \tag{6.2}$$

and in this regime, for a constant population of emitters, N, the enhancement in PL intensity from $I_{PL,0}$ to $I_{PL,enh}$ is equal to the radiative rate enhancement from $\Gamma_{rad,0}$ to $\Gamma_{rad,enh}$, i.e.,

$$\frac{I_{PL,enh}}{I_{PL,0}} = \frac{\Gamma_{rad,enh}}{\Gamma_{rad,0}} \quad (\sigma\phi \gg \Gamma_{exp}) \tag{6.3}$$

In Eq. (3.4) of Chapter 3, we expressed the enhanced radiative decay rate as

$$\Gamma_{rad,enh} = \Gamma_{rad,0} \left| L(\omega_{PL}) \right|^2 \tag{6.4}$$

where $L(\omega_{PL}) = E_{enh}(\omega_{PL})/E_0(\omega_{PL})$ is the field enhancement factor at the PL emission frequency. In the limit of a large pump flux, we therefore expect that, since the experimentally observed PL intensity enhancement is proportional to the radiative rate enhancement, it too will be equal to the enhanced field intensity, $|E_{enh}(\omega_{PL})|^2$, normalized by the incident field intensity, $|E_0(\omega_{PL})|^2$, i.e.,

$$\frac{I_{PL,enh}}{I_{PL,0}} = |L(\omega_{PL})|^2 = \frac{|E_{enh}(\omega_{PL})|^2}{|E_0(\omega_{PL})|^2} \quad (\sigma\phi \gg \Gamma_{exp}) \tag{6.5}$$

6.2.2 Electromagnetic Simulations

As in Chapter 3, the simulations in this chapter were performed by three-dimensional full-field electromagnetic simulations utilizing finite-element integration techniques to solve Maxwell's equations.[86]

The experimental samples of Chapter 5, to which we compared our calculations, consisted of 100 μm $\times$ 100 μm square arrays of cylindrical silver nanoparticles (np-Ag) 20 nm in height and having a range of diameters, $d = 100-500$ nm, and pitches (particle center-to-center spacings), $p = 200-500$ nm. The nanoparticles rested on a 2 mm thick substrate of fused silica doped with nc-Si at a depth $\Delta \sim 10$ nm beneath the base of the np-Ag plane.

Computations were conducted on a system that best emulated the experimental samples given the restrictions of the simulation package.[86] The fabricated 100 μm $\times$ 100 μm arrays were essentially infinite from the perspective of the measurements taken at the center of the array with a beam focused to a ~ 10 μm^2 spot. This was verified in Fig. 5.6, which showed essentially no variation in PL intensity with position over the majority of the array. We therefore simulated the arrays by using von Karman periodic boundary conditions to make a two-dimensional infinite array of np-Ag. The simulation was done over the volume of four particles arranged in

a box $2p$ wide and 300 nm deep. This $1200p^2$ nm^2 volume was divided into $1.25p^2$ grid cells, refined to give the greatest detail in the area about the Ag particles. Similar simulations have previously been shown to correspond well to experiments by Sweatlock et al.[83] The simulated np-Ag were cylinders of height 20 nm. The particle diameters and the pitches in each array were chosen to correspond exactly to those examined experimentally, based on scanning electron microscopy (SEM) of the samples.

The Ag dielectric function was approximated using a modified Drude model fitted to tabulated data over the wavelength range of interest.[87] The dielectric function of silver, ε_{Ag}, as a function of radial frequency, ω, was thus given by the Drude relation,

$$\varepsilon_{Ag}(\omega) = 5.45 - 0.73\frac{\omega_{b,Ag}^2}{\omega^2 + i\omega\gamma_{Ag}} \tag{6.6}$$

where the bulk plasmon frequency is $\omega_{b,Ag} = 1.72 \times 10^{16}$ rad s^{-1}, and the plasmon decay rate is $\gamma_{Ag} = 8.35 \times 10^{13}$ s^{-1}.

Simulations were performed with sample geometries selected to emulate the experimental conditions as accurately as possible. Since our software package does not allow for an interface to lie along a periodic boundary,[86] we replaced the fused silica ($\varepsilon_{SiO_2} = 2.2$) under the nanoparticles, and the air ($\varepsilon_{air} = 1$) around and above the nanoparticles by an effective medium. Figure 6.1 shows a cross-sectional view of the enhanced local field about a silver nanoparticle. Using an iterative technique, we determined that 70% of the field emanating from a resonant Ag nanoparticle lies beside and above the particle, so we chose an effective medium with dielectric constant $\varepsilon_{\text{eff}} = (0.7\varepsilon_{SiO_2} + 0.3\varepsilon_{air}) = 1.36$. The subtle inhomogeneity in the field profile in this figure results from an incomplete subtraction of the plane wave, which is incident along the y-axis.

In the experiments of Chapter 5, the array plasmon resonance was measured by far-field transmission in a microscope. A white light source illuminated the array normal to the surface and the transmitted light spectrum was measured and compared to the transmission through nc-Si-doped SiO_2 without Ag nanoparticles.

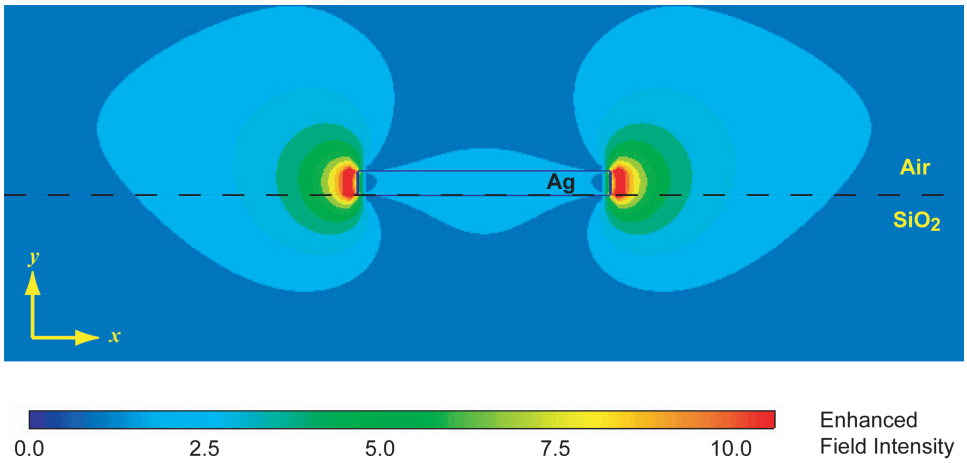

Figure 6.1: Cross-sectional view of the simulated enhanced local field about a silver nanoparticle. 70% of this field lies above the dashed line, which denotes the air/SiO_2 interface of the experimental system, not present in our simulations.

The photoluminescence was also measured experimentally by far-field microscopy. There, the samples were excited normal to the surface by a 532 nm laser line, and emission was collected normal to the surface. The PL enhancement was calculated by comparing the emission spectrum and intensity of nc-Si under each Ag array to that of nanocrystals far away from Ag arrays with all else held constant.

In our simulations, the spectral response of the np-Ag array was determined by illuminating the particle assemblies by a plane wave incident normal to the plane of particles, along the y-axis. The wave was polarized in the x-direction. After 75 fs, the incident plane wave was interrupted. In the absence of an applied external field, the plasmon mode decayed; this ringdown was observed for 100 fs, and a Fourier transform of the time decay behavior gave the characteristic oscillation frequency, or plasmon resonance, of the mode.

The near-field optoelectronic response was subsequently obtained by illuminating the particles at the np-Ag array resonant frequency with a plane wave normal to the sample and allowing the array to store energy for 100 fs. At this point of maximum energy storage, the local-field profile could be investigated. After Eq. (6.5), we expect the photoluminescence enhancement due to plasmon coupling to be proportional to the field intensity, $|E|^2$. Therefore, in the place of modeling

the actual emission from nc-Si embedded in SiO_2 beneath np-Ag, in the present chapter, we monitored the value of $|E|^2$ integrated spatially over the plane of the emitters, i.e., in a plane 10 nm below the bottom of the np-Ag array. This mean field intensity was also integrated over an optical cycle to provide the time-averaged value of the local-field intensity; this is needed for comparison with the experimental measurements, which were acquired over the course of several seconds.

6.3 Results and Discussion

In this chapter, we use finite-integration simulations. These account for finite-size, geometry, and coupling effects, thus permitting us to explore complicated assemblies of large, non-ellipsoidal, interacting nanoparticles whose electromagnetic properties cannot be treated analytically. This technique allows us to determine the plasmon resonance modes and accompanying electric field profiles for the np-Ag arrays. Furthermore, based on the results of our computations, we can apply our analytical understanding of the optical properties of metals to interpret the trends that follow from the calculations.

6.3.1 Plasmon Resonance Modes

A two-step process is used to determine the frequency of the plasmon resonance mode of the silver cylinder arrays. First, the Ag particles are illuminated and allowed to absorb energy. Next, the incident field is switched off and the electric field amplitude is observed as the excited mode decays. The ringdown of a typical np-Ag array, with $d = 155$ nm and $p = 400$ nm, is presented in Fig. 6.2(a). A temporal Fourier transform of the decaying field yields the spectral response of the system, and the plasmon response spectrum corresponding to the time decay in Fig. 6.2(a) is presented in Fig. 6.2(b); this shows a dipolar plasmon resonance at 705 nm.

While holding the pitch constant at 400 nm, the average particle diameter was increased from 135 nm to 320 nm. This corresponds to the eight samples that

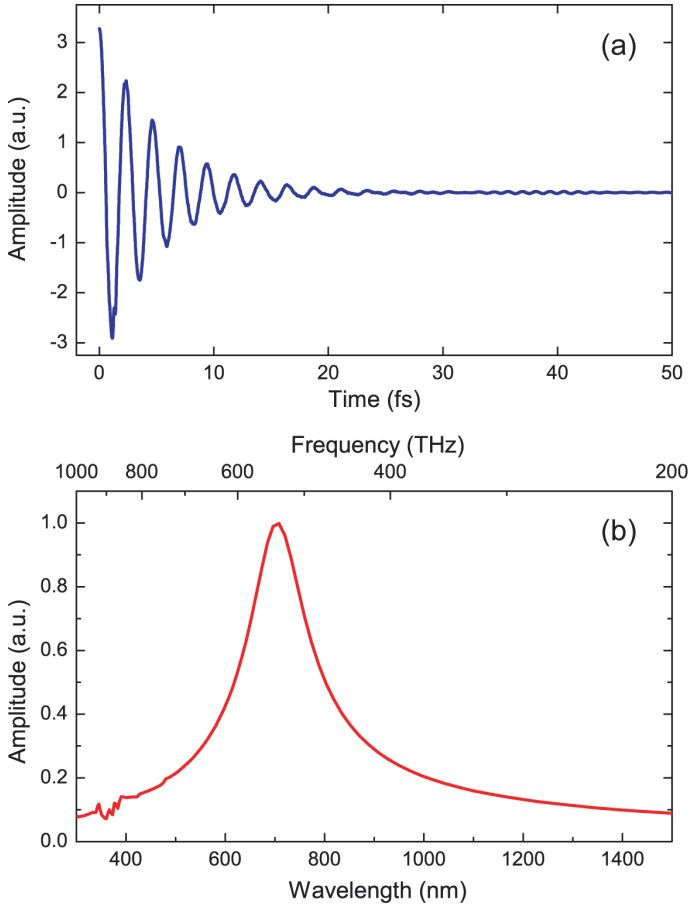

Figure 6.2: Silver nanoparticle array plasmon resonance determination for a characteristic array ($d = 155$ nm, $p = 400$ nm). (a) Electric field ringdown with time. (b) A temporal Fourier transform identifies the dipolar plasmon mode at 705 nm.

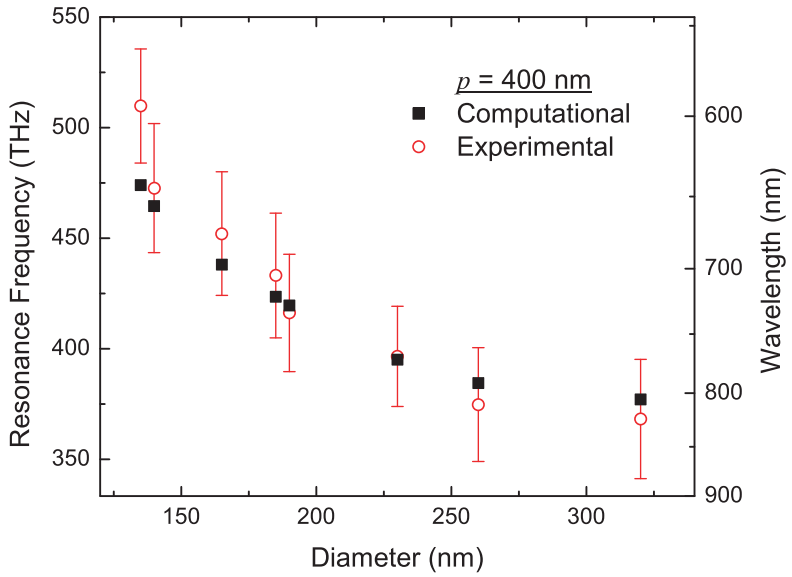

Figure 6.3: Computed and experimentally determined (black squares and red circles, respectively) resonance frequencies for arrays of np-Ag with constant pitch, $p = 400$ nm.

were shown in the series of SEM micrographs in Fig. 5.3. In Fig. 6.3, the experimentally derived resonance frequencies (circles), determined from the frequency of minimum transmission through each array, are compared to the experimentally determined plasmon resonance frequency of such an array (squares). There is a very strong agreement between the two methods, which indicates that the model system considered in our computations is a good analog for the experimental system, and which also confirms that the transmission dips measured experimentally are indeed manifestations of the excitation of a resonant plasmon mode.

At this constant pitch, the resonance frequency decreases with increasing particle size. Here, since we consider a constant particle height, $h = 20$ nm, a larger diameter reflects an increased aspect ratio, $a = d/h$. The decreasing resonance frequency with increasing particle size is consistent with the analytical result for oblate spheroids, which indicates that the resonance frequency is a function of the aspect ratio.[80]

We subsequently considered a set of np-Ag arrays with the diameter held constant at 165 nm, and pitch increasing from 200 to 500 nm, corresponding to the

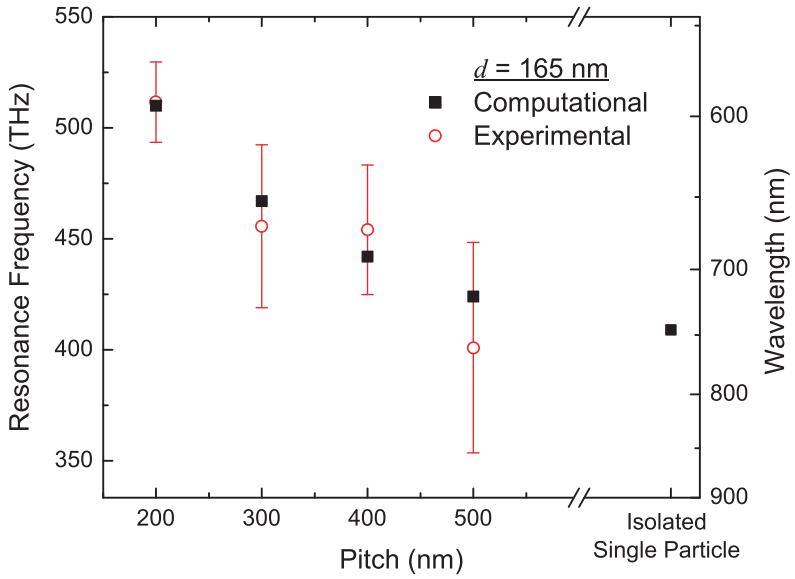

Figure 6.4: Computed and experimentally determined (black squares and red circles, respectively) resonance frequencies for arrays of np-Ag with constant diameter, $d = 165$ nm.

experimental series imaged by SEM in Fig. 5.4. Additionally, we examined the behavior of an isolated Ag nanoparticle of the same size. This last case, which represents an array with infinite pitch, was not accessible experimentally. The plasmon resonance frequencies of the arrays are shown in Fig. 6.4, where the computed resonances (squares) are compared to the experimental values (circles). Here, again, there is good agreement between the computational and experimental results. In this series, the resonance frequency decreases as the interparticle spacing increases, and indeed the isolated single particle has the lowest resonant frequency. This result would be counter-intuitive for very closely spaced, infinitesimally small metal particles, but, as discussed in Chapter 3, it is consistent with previous results for more widely spaced, finite-sized particles where long-range electrodynamic interactions prevail.[85]

The single particle result in Fig. 6.4 further illustrates the necessity of performing computational studies with cylindrical discs, rather than resorting to approximating cylinders with analytically solvable analogs like oblate spheroids. In this figure, a cylindrical particle with a 165 nm diameter and a 20 nm thickness has a

resonance frequency of 409 THz. However, the analytical treatment of an oblate silver spheroid, with a long-axis diameter of 165 nm and a short-axis diameter of 20 nm, using the same Drude model of silver as in Eq. (6.6), yields a resonance frequency of 508 THz.[80]

The experimental and computational resonance frequencies in Figs. 6.3 and 6.4 were determined from the extrema of the measured transmission and the calculated spectral response, respectively. In Figs. 6.5 and 6.6, we compare the spectra from which these peaks were derived. Figure 6.5 displays the experimental transmission measurements (dashed lines) and the computational spectral response curves (solid lines) for arrays with pitch, $p = 400$ nm and diameter, $d = 140-260$ nm. The particle diameters decrease from the top panel to the bottom one, with $d = 260$, 230, 190, 185, 165, and 140 nm, respectively.

In our experiments, the depth of the transmission peak was a measure of both the absorbance and the scattering. Unfortunately, these two effects could not be deconvolved, since the maximum absorbance and scattering frequencies are expected to be approximately equal. The experimental transmission measurements in Figs. 6.5 and 6.6 (dashed lines) are therefore not a direct measure of the plasmon absorption strength and, correspondingly, we noted no correlation between the magnitude of transmission on resonance and the PL intensity enhancement. However, the calculated spectral responses in Figs. 6.5 and 6.6 (solid lines), were obtained from a temporal Fourier transform of the field intensity decay with time. Despite the complexity of the relationship between field intensity and energy in metals, these computed spectral responses still provide qualitative measures of the amount of energy absorbed into the particle, and the amplitude of these curves is related to the particle plasmon mode strength. In Fig. 6.5, the spectral response increases with decreasing particle size. This result of weaker plasmon resonance strength for larger particle size is consistent with our experimental observations of greater PL enhancement effects upon coupling to smaller metal nanoparticles, as will be further discussed in Section 6.3.2.

Figure 6.6 presents the computational and experimental spectra for the case of

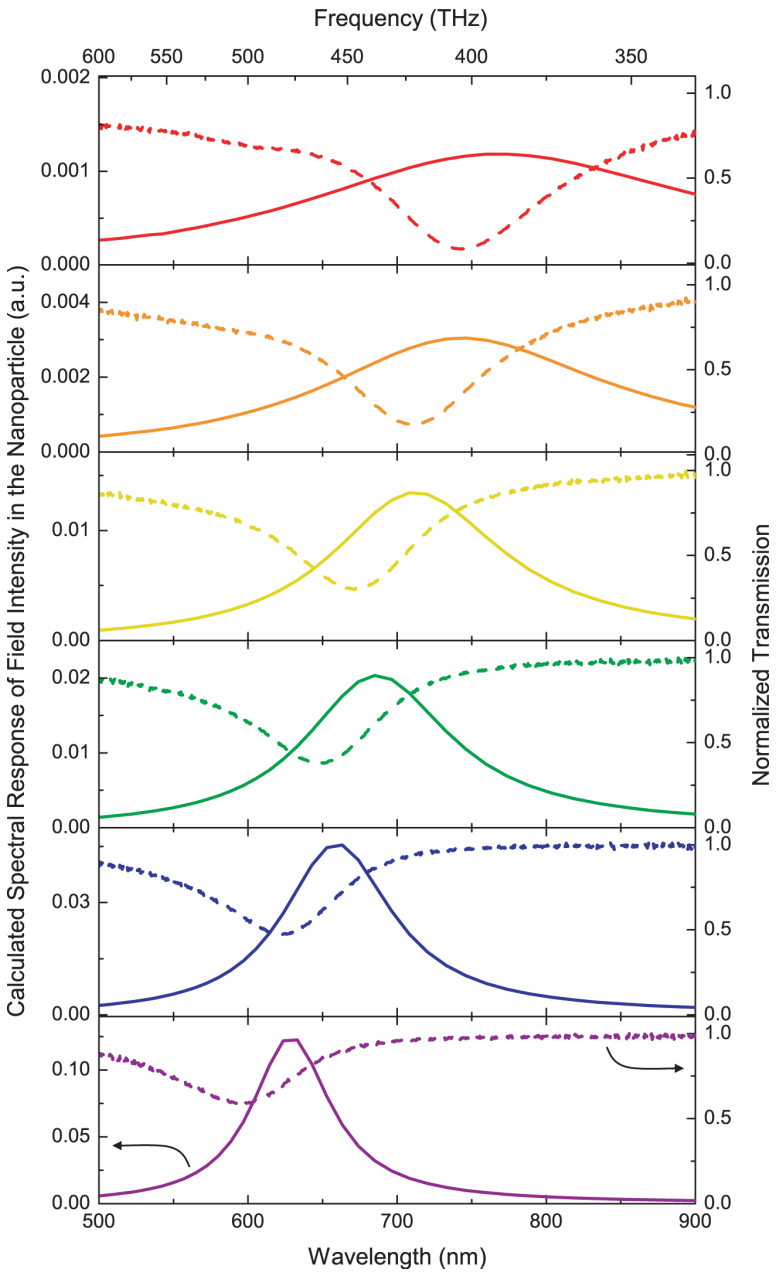

Figure 6.5: Computed field intensity spectral response curves (solid lines) and experimental transmission measurements (dashed lines) for np-Au arrays with $p =$ 400 nm and $d = 260$, 230, 190, 185, 165, and 140 nm (from top to bottom).

a series of arrays with a fixed diameter (165 nm) and variable pitches ($p = 200-500$ nm). Here, the magnitude of the spectral response, and hence the plasmon resonance strength, increases with increasing pitch. This increased field intensity amplitude is also acompanied by a spectral narrowing, which indicates an increase in the plasmon mode dephasing time, T_2. The arrays under consideration have pitches that are on the order of the resonance wavelength. We can therefore attribute the trends in Fig. 6.6 to wavelength-scale interparticle coupling effects. In the top panel, the resonance excitation wavelength of 587 nm has an effective wavelength of 432 nm in the $\varepsilon_{\text{eff}} = 1.36$ medium surrounding the np-Ag. This array has a pitch of 200 nm, and neighboring particles are therefore separated by half a wavelength. Such a spacing has a detrimental effect on the strength on interparticle coupling and thus on the strength of the collective plasmon resonance. Conversely, in the bottom panel of Fig. 6.6, the effective wavelength of the resonance is 534 nm, which nearly coincides with the pitch of 500 nm. Here, interparticle coupling has a constructive effect on the strength of the plasmon resonance.

6.3.2 Enhanced Local Field

In addition to obtaining spectral information, we determined the field intensity throughout the three-dimensional space about each np-Ag array with electromagnetic simulations. We illustrate our results for an array with $d = 135$ nm and $p = 400$ nm, excited at its computed resonance frequency of 633 nm, in Figs. 6.7 and 6.8. Figure 6.7 displays the electric field intensity at a cut along a plane through the center of the Ag particles. The incident light is polarized in the x-direction. Figure 6.8 shows a cut along the plane where, in the experimental case, the nc-Si emitters would reside. This is a plane parallel to the Ag nanoparticle plane at depth, $\Delta = 10$ nm, below the base of the nanoparticles.

In the experiments in Chapter 5, the nc-Si were distributed uniformly across a plane. A measure of the average field intensity experienced by the emitters in this plane was thus found computationally by integrating the field intensities over the area of the plane. For example, the average field intensity felt by a nc-Si emitter

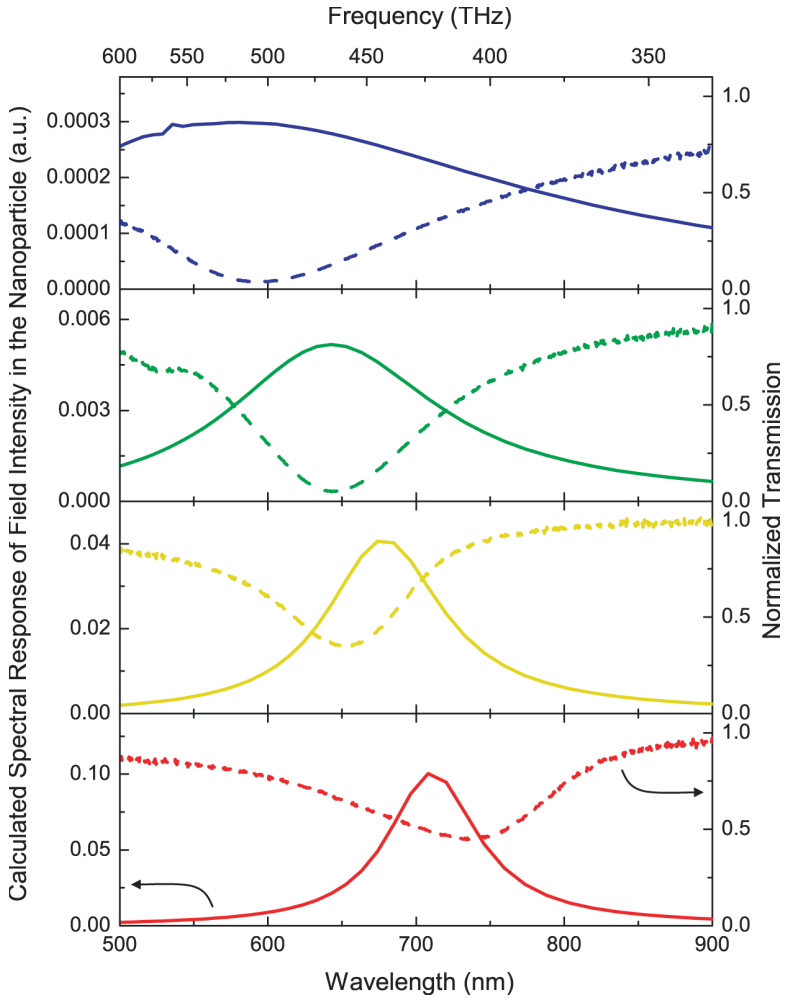

Figure 6.6: Computed field intensity spectral response curves (solid lines) and experimental transmission measurements (dashed lines) for np-Au arrays with $d =$ 165 nm and $p =$ 200, 300, 400, and 500 nm (from top to bottom).

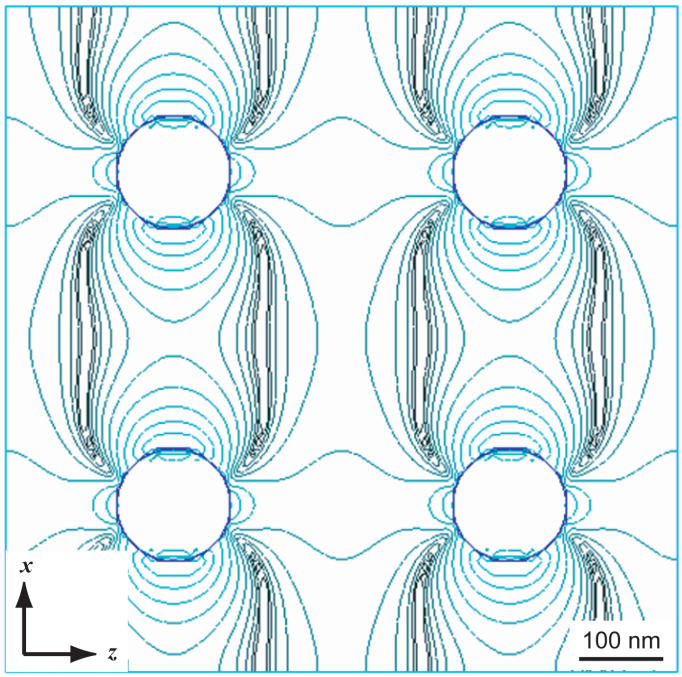

Figure 6.7: Instantaneous enhanced field intensity in the plane of the np-Ag array. Here, four contour lines represent an order of magnitude change in the x-component of the field intensity. $d = 135$ nm, $p = 400$ nm, and $\lambda_{exc} = 633$ nm.

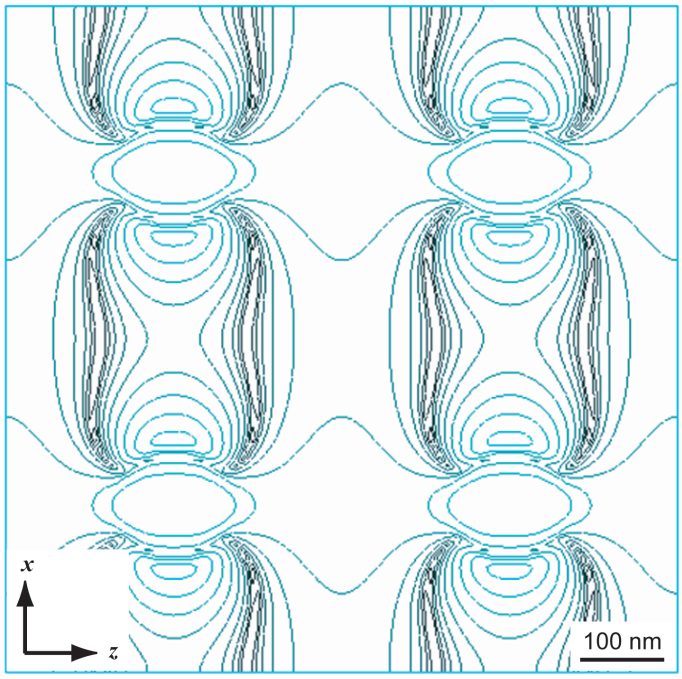

Figure 6.8: Instantaneous enhanced field intensity profile in a plane 10 nm beneath the base of the np-Ag array. Here, four contour lines represent an order of magnitude change in the x-component of the field intensity. $d = 135$ nm, $p = 400$ nm, and $\lambda_{exc} = 633$ nm.

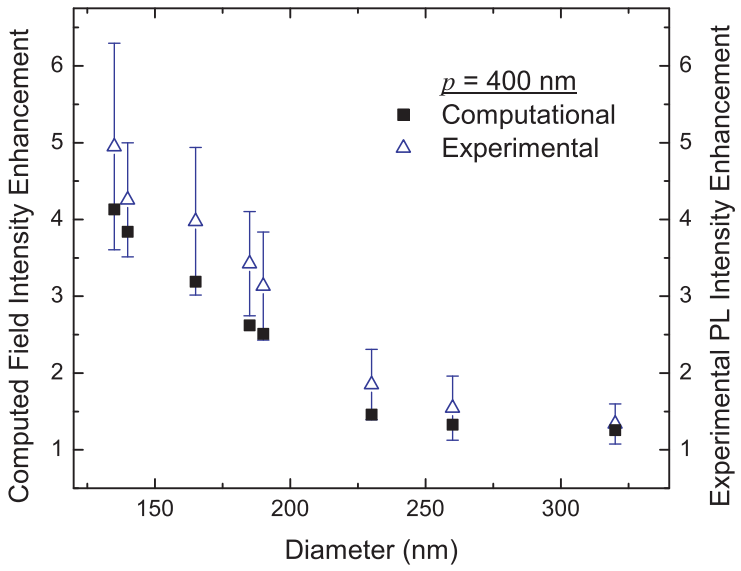

Figure 6.9: Computed and experimentally determined (black squares and blue triangles, respectively) enhancement factors for arrays of np-Ag with constant pitch, $p = 400$ nm.

in the plane beneath an array of $d = 135$ nm, $p = 400$ nm np-Ag was found by integrating the field intensity plotted in Fig. 6.8 over the area of that figure. This intensity was further normalized by the incident field, and time averaged over an optical cycle. For each sample, we expect the average measured PL enhancement to be equal to the normalized average computed field intensity, as predicted by Eq. (6.5).

Figure 6.9 compares the computed time-averaged field intensity enhancement in the nc-Si plane (squares) to the measured PL intensity enhancement of the nc-Si emitters (triangles) for np-Ag arrays with a 400 nm pitch. The two quantities agree, and our electromagnetic simulations of the field intensity are therefore good predictors for the PL enhancement effect of Chapter 5.

Figure 6.10 compares the measured PL intensity enhancement for nc-Si emitters (triangles) to the computed time-averaged field intensity enhancement in their plane (squares) for np-Ag arrays with $d = 165$ nm and $p = 200-500$ nm. Here, there is a very poor agreement between the experiments and the calculations. We ascribe this lack of correspondence to the unrealistic perfect symmetry in

the simulated samples. In our discussion of Fig. 6.6, we stated that due to the relationship between resonance wavelength and pitch in the different arrays, the strength of the plasmon mode in the $p = 500$ nm array benefits from nearly perfect constructive interference, while that of the $p = 200$ nm array suffers from almost complete destructive interference. From Fig. 6.10 then, it appears that as a result of the unrealistic perfect symmetry, the simulations overestimate these long-range coupling effects, leading in the present case to an undershooting at small pitches and an exaggeration at large pitches. The red circles in Fig. 6.10 show the calculated field intensity enhancement in the plane beneath isolated Ag nanoparticles. Here, interparticle coupling is explicitly removed, and the variation in field intensity with pitch is due solely to differences in np-Ag coverage. Except for at the smallest pitches, these calculations agree much more strongly with the experimental results, indicating that the experimental configuration destroys the symmetry of the system. The experimental results of Chapter 5 can be primarily ascribed to the effect of uncoupled Ag nanoparticles.

The spatially averaged field intensity is a good metric for comparison with ensemble measurements. However, the field intensity profiles in Figs. 6.7 and 6.8 also provide further insight into the design of a more ideal system. For instance, the field intensity map of the nc-Si plane in Fig. 6.8 indicates that the field is lowest directly under the Ag nanoparticles, and that it also decreases from the particle edges outward toward the spaces between the particles. Given the geometry of nc-Si in a plane beneath the np-Ag, it would thus be ideal to limit the Si nanocrystals to a ring around the Ag nanoparticle circumferences. This could be achieved by using the metal particles as a shadow mask for the removal of silicon nanocrystals in less favorable positions.

A further understanding of the np-Ag arrays is gained by integrating successive planes in depth to obtain the average field intensity at each depth. Figure 6.11 shows the decay of the integrated field intensity as a function of depth for arrays with $p = 400$ nm and $d = 135$, 185, and 320 nm. For all diameters, the field intensity decrease with depth is well fitted by an exponential with a $1/e$ decay

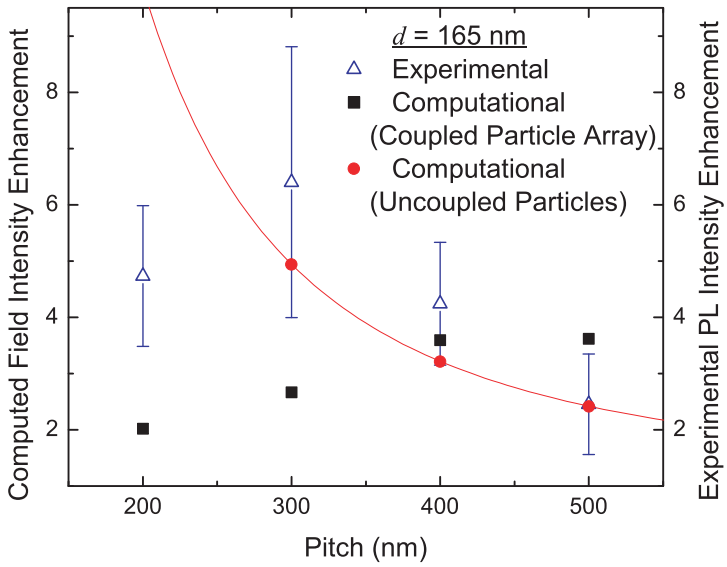

Figure 6.10: Computed (squares and circles) and experimentally determined (triangles) enhancement factors for arrays of np-Ag with constant diameter, $d = 165$ nm. As discussed in the text, due to the unrealistic perfect symmetry in the simulated samples, the experimentally observed enhancement agrees more strongly with computations for uncoupled Ag nanoparticles (red circles) than with the computed enhancement factors for coupled arrays of Ag nanoparticles (black squares).

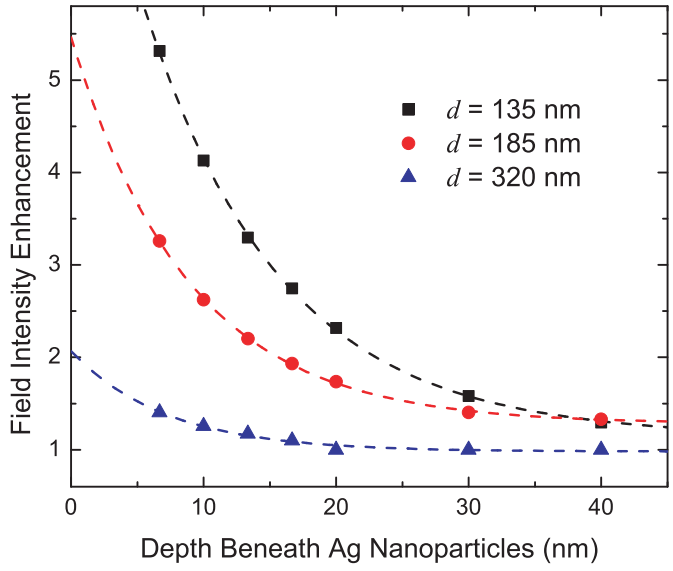

Figure 6.11: Decay of the integrated field intensity enhancement as a function of depth from the base of the np-Ag array for $p = 400$ nm and $d = 135$ nm (black squares), 185 nm (red circles), and 320 nm (blue triangles).

length of 8 ± 2 nm (dashed lines). This result implies that in designing an ideal experimental system, though it is best to place the nc-Si reasonably close to the Ag nanoparticles, some spatial separation can be tolerated. Additionally, it is not imperative that the emitters be perfectly aligned; a 2−4 nm distribution of depths would have only minor effects.

6.4 Conclusions

The electromagnetic simulations presented in this chapter verified an important assumption of Chapter 5, that the energy of minimum transmission through np-Ag arrays, at which a maximum nc-Si PL enhancement was observed, is the plasmon resonance frequency of these arrays. From our calculations, we also determined that the maximum field intensity about a small particle is indeed much greater than that about a larger particle; this effect is strong enough to compensate for the low surface coverage in small particle arrays. Finally, we showed that the field intensity decays exponentially with increasing depth beneath the plane of the metal nanoparticles. This suggests further experiments with carefully controlled emitter depths to probe this relationship.

Accurate simulations have a great predictive power. In designing future experiments, we can now foretell the resonance frequency of a nanoparticle array *a priori*, which could be important when coupling metals to emitters with sharp emission spectra, for instance dyes and direct band gap semiconductor materials. In such situations, resonant coupling could only occur if the metal array was carefully designed to have a plasmon resonance spectrum that overlapped the precise emission spectrum.

Finally, the results in this chapter give insight into the local-field intensity as a function of position on a scale smaller than that which we measure with far-field optics. This suggests the possibility of using near-field scanning optical microscopy (NSOM) to map the field lines experimentally, but as well, this indicates that simulated field intensity maps can be used to gain the understanding needed to

design optimized optical devices, in which the emitters reside in areas of high field concentration.

Chapter 7

Enhanced Electroluminescence

7.1 Introduction

From the experimental and computational studies in the previous three chapters, it is clear that coupling to plasmonic metal nanostructures holds much promise for enhancing the photoluminescence intensity and radiative rate of silicon nanocrystal (nc-Si) emitters. Within the context of this project, the ultimate application of plasmon enhancement effects is one that incorporates the benefits of metal nanoparticles into CMOS-compatible, nc-Si-based light-emitting diodes (LEDs). Consequently, we have paired silicon nanocrystals in field-effect light-emitting diodes (FELEDs) to silver nanoparticle arrays and rough silver films.

The emission of such coupled devices, which can be excited electrically as well as optically, displays the first evidence of enhanced electroluminescence (EL) from nc-Si coupled to nanostructured silver. The properties of plasmon-enhancement in nc-Si FELEDs are discussed in the present chapter.

7.2 Experimental

7.2.1 Fabrication of a Metal-Coupled FELED

The metal-coupled light-emitting devices studied in this chapter build upon the nc-Si FELEDs introduced by Walters et al.[9] In the present study, we modify such

basic nc-Si FELED devices for the specific purpose of metal nanoparticle coupling.

The initial FELEDs are MOS ring gate transistor structures that were fabricated at a 300 nm wafer fabrication facility at Intel Corporation in Hillsboro, OR;[97] they are therefore fully compatible with CMOS fabrication technology. In this process, a 15 nm thick dry thermal oxide was grown on a *p*-type silicon wafer at 900 °C. Si^+ ions were then implanted into the oxide to an average depth of 10 nm and to a peak excess silicon concentration of 20%, according to Monte Carlo simulations performed using the SRIM package.[40] The implanted wafers were annealed for 5 min at 1050 °C in 2% oxygen in argon to nucleate and grow silicon nanocrystals (nc-Si) in the SiO_2 layer. Following nc-Si formation, a 40 nm polysilicon layer was deposited above the nc-Si-doped SiO_2 by low-pressure chemical vapor deposition at 600 °C. Subsequently, the ring gate MOS transistor pattern was created in this stack using standard photoresist patterning and reactive ion etching techniques to remove both the polysilicon gate and the nc-Si-doped SiO_2 from the source and drain regions in a single-mask process. Finally, the sample was implanted with a blanket deposition of P^+ and As^+ to dope the source, drain, and gate regions degeneratively.

The samples fabricated as above provided a good starting point for constructing metal-coupled nc-Si FELED devices. However, in this initial structure, there was a 50 nm gap between the mean nc-Si position and the device surface; some post-processing modifications were therefore necessary to lessen the gap and permit the near-field coupling of Ag nanoparticles and silicon nanocrystals. Consequently, we developed a controllable chemical etch procedure to thin the top polysilicon gate. First, the native oxide was removed from the silicon surface with a 5 s etch in buffered hydrofluoric acid (7.2% HF(aq), 36% NH_4F(aq) v/v). Then, following a rinse in 18 MΩ·cm resistivity water, the silicon was etched for 10 s in a solution of 1 mL HF and 150 mL nitric acid (HNO_3). This solution etches polysilicon at a rate of $\sim$ 2 nm/s, and may also slightly roughen the surface in the process.[98] We thus reduced the top gate thickness from 40 to 17 nm, a thickness that was later characterized by spectral ellipsometry over the range of 300−820 nm using a

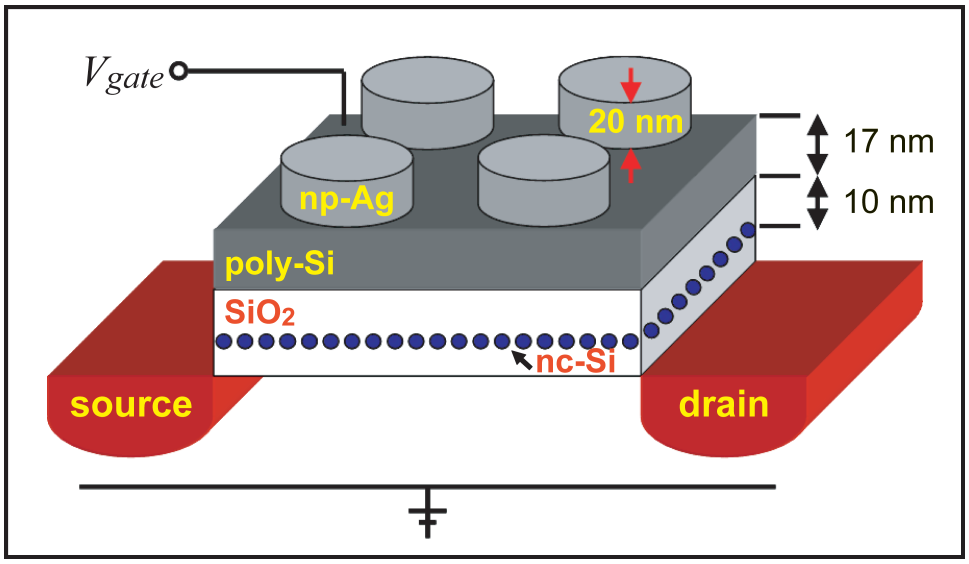

Figure 7.1: Schematic of the metal-coupled silicon nanocrystal FELED. Arrays of 20 nm thick Ag nanoparticles sit on a 17 nm polysilicon gate. Under the gate, a 15 nm thick SiO_2 film contains nc-Si emitters at an average depth of 10 nm. The gate is biased with a voltage, V_{gate}, relative to the p-type Si back contact.

Sentech SE-850 ellipsometer.

An Ohmic contact to the gate was subsequently made by photolithographical patterning and the thermal evaporation of a 10 nm thick chrome wetting layer and a 200 nm gold pad. The p-type silicon backside of the device was metalized by the thermal evaporation of a 200 nm thick aluminum layer, followed by a 12 h anneal at 100 °C.

The thinned devices were covered with Ag nanostructures using an electron-beam lithography procedure very similar to the protocol described in Chapter 5. Briefly, the samples were coated with two layers of PMMA and exposed to an electron beam to pattern 50 μm $\times$ 50 μm square arrays of circles on the surface, where each array had a predetermined pitch (center-to-center separation distance) and circle diameter. In the limiting case where we selected very large diameters, the entire 50 μm $\times$ 50 μm area was exposed. Following the development of the exposed PMMA, 20 nm of Ag was deposited on the sample by thermal evaporation, and after a gentle liftoff in acetone, arrays of cylindrical Ag nanoparticles 20 nm

in height, or a continuous, 20 nm thick Ag film in the case of the highest electron-beam exposures, remained on the surface.

This final sample is schematized in Fig. 7.1. Here, the top gate is biased relative to the p-type Si back contact with a voltage, V_{gate}. As has been previously described, the heavily doped source and drain regions provide electrons for charge injection and subsequent exciton formation in the nc-Si.[9]

7.2.2 Optoelectronic Characterization

The photoluminescence (PL) and electroluminescence (EL) of the coupled nc-Si were measured in an inverted microscope. For this purpose, the devices were mounted on a homemade package to which the gate contacts were connected using gold wires adhered with a wedge bonder. An image of the sample thus prepared is shown in Fig. 7.2(a). The np-Ag arrays on top of this sample are seen through a 10× microscope objective in Fig. 7.2(b).

The optical excitation for PL spectroscopy was provided by the 488 nm line of an Ar^+ laser at low pump power ($P_{ex} < 10$ mW/mm^2). For EL, the sample was driven electrically with a square wave from a 20 MHz arbitrary function generator with a 10 MΩ output termination. The EL measurements in this chapter were made with an electrical signal frequency of 5 kHz and wave amplitudes of $5-9$ V_{rms}.

Emission was collected in the microscope through a 50× objective, and the field of view was limited to 20 μm × 20 μm with 2000-μm slits downstream of the objective. The signal was detected using a rectangular silicon charge-coupled device (CCD) detector array (sensitivity range $20-1100$ nm) cooled with liquid nitrogen to $-132\,^{\circ}$C, in conjunction with a 27.5 cm focal length grating spectrograph. For PL, an additional dichroic filter was used in front of the monochromator entrance to cut off scattered laser illumination. Luminescence enhancements were calculated by comparing the photo- or electroluminescence of nc-Si coupled to nanostructured Ag to the emission of nearby nc-Si in a region devoid of Ag, where the reference spectrum was acquired under identical excitation and collection conditions.

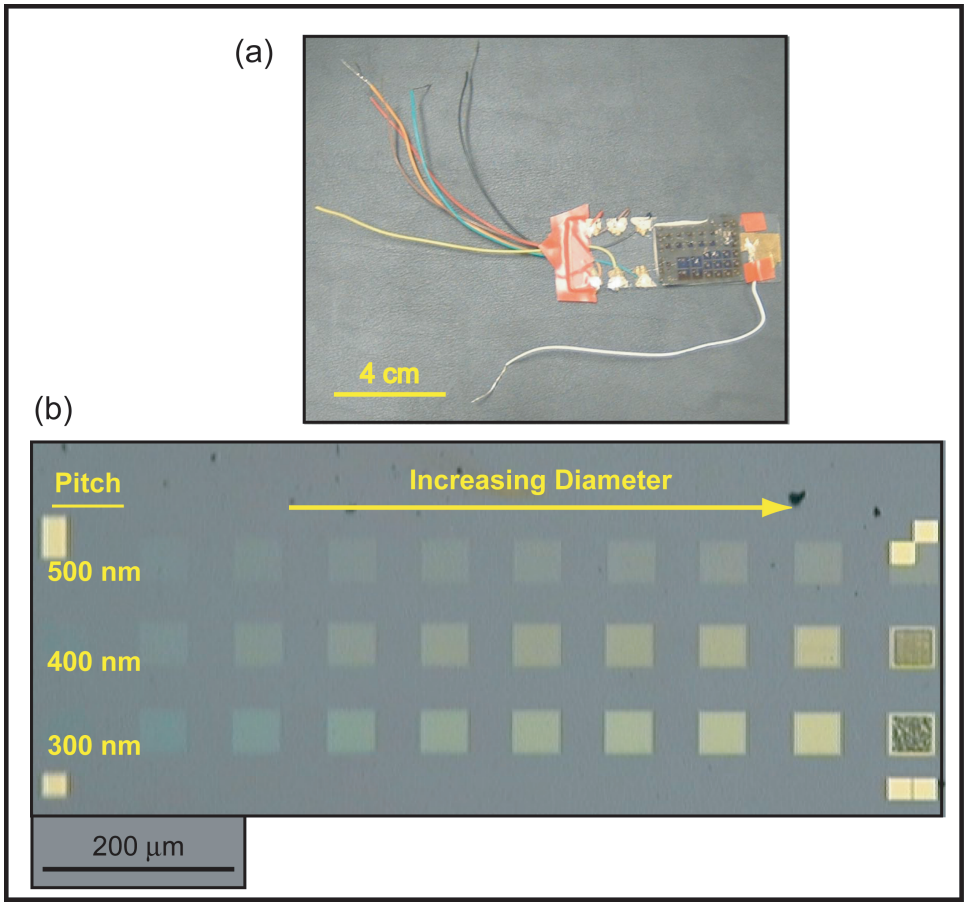

Figure 7.2: (a) Image of the packaged plasmon-coupled nc-Si FELED device, and (b) 10× microscope image of the np-Ag arrays on its surface.

7.3 Results and Discussion

The arrays of Ag nanoparticles (np-Ag), fabricated as described above, were imaged by scanning electron microscopy (SEM). Figure 7.3 shows micrographs of six arrays of isolated np-Ag with different diameters and pitches. Both under optical and under electrical pumping conditions, the nc-Si emission was strongly affected by the presence of np-Ag arrays. The black curve in Fig. 7.4(a) shows the PL intensity spectrum of the nc-Si in the absence of Ag (black curve). The introduction of np-Ag arrays produces an enhancement in the PL intensity, and, for a fixed 400 nm pitch, this enhancement increases with particle diameter to a maximum enhancement of 1.25.

For the same samples, the electroluminescence spectra are displayed in Fig. 7.4(b). This emission was obtained upon biasing the sample with a 5 kHz, 7 V_{rms} signal. As was true for the PL results, coupling nc-Si to np-Ag arrays gives rise to an enhancement in the EL intensity of the Si nanocrystals, and this effect grows with increasing particle diameter. Here, a maximum enhancement of 1.75 is found for nc-Si paired with the largest-diameter np-Ag arrays.

The trend of increasing luminescence with nanoparticle size is opposite to the effect that we observed upon coupling nc-Si in SiO_2 to very similar np-Ag arrays in Chapter 5. There, the greatest PL enhancements were seen for the smallest Ag nanoparticles. However, one important difference between those nc-Si-doped SiO_2 samples and the nc-Si FELEDs in the present chapter is the texture of the surface onto which Ag is evaporated. Figure 7.5 shows a 25×25 μm^2 atomic force microscopy (AFM) scan of the Si surface. This figure indicates that thinning the FELED gate in a HF/HNO_3 solution produces surface roughness on the scale of $\lesssim 5$ nm. As a result, there are two levels of metal features in the np-Ag arrays on the FELED surface: the Ag nanoparticles, with diameters on the order of 100 nm, and the nanometer-scale roughness at the particle/gate interface. We therefore attribute the nc-Si electroluminescence enhancements in the present chapter to local-field concentration about the nanoscale roughness on the nanoparticle sur-

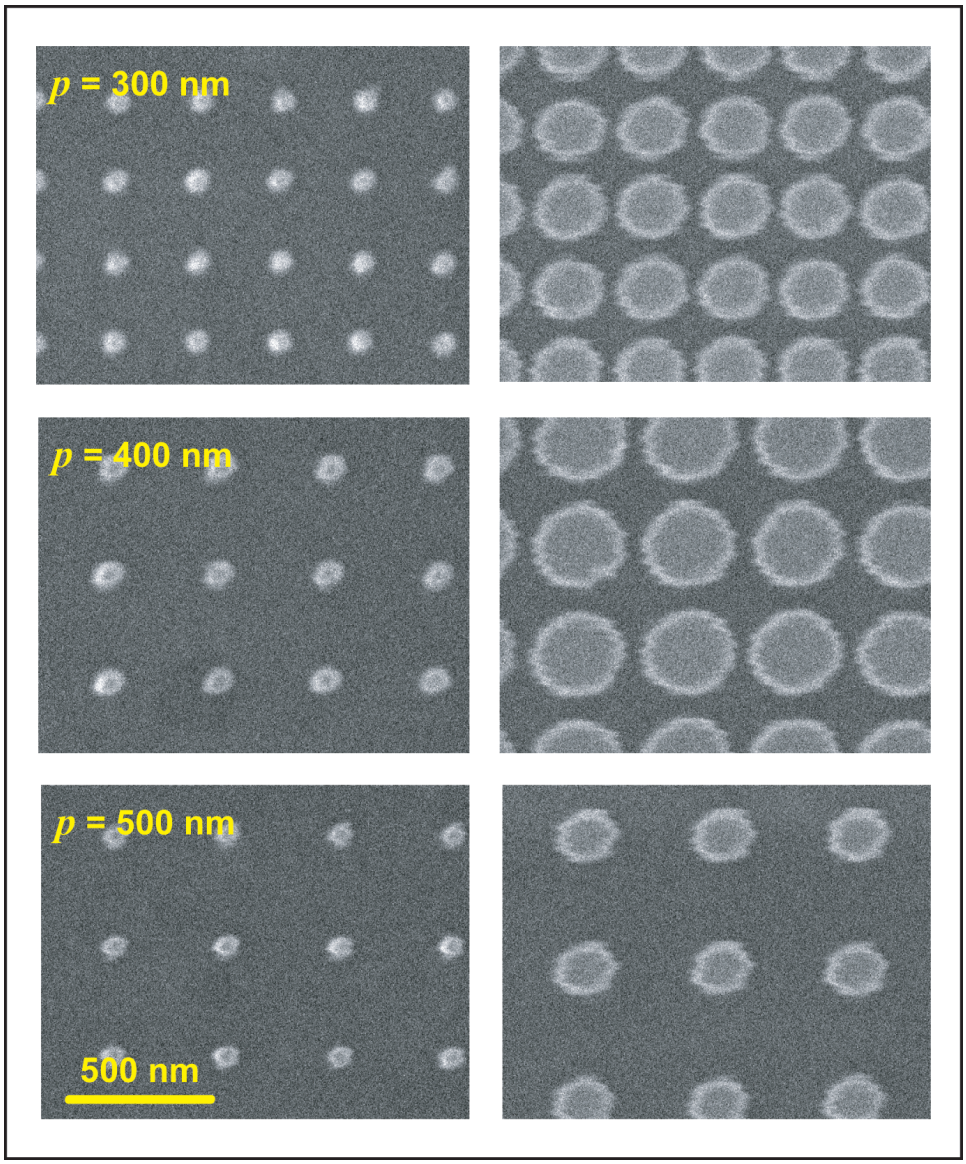

Figure 7.3: 1.5 μm $\times$ 1.2 μm SEM images at 60 000$\times$ magnification of isolated Ag nanoparticle arrays on top of a nc-Si FELED top gate.

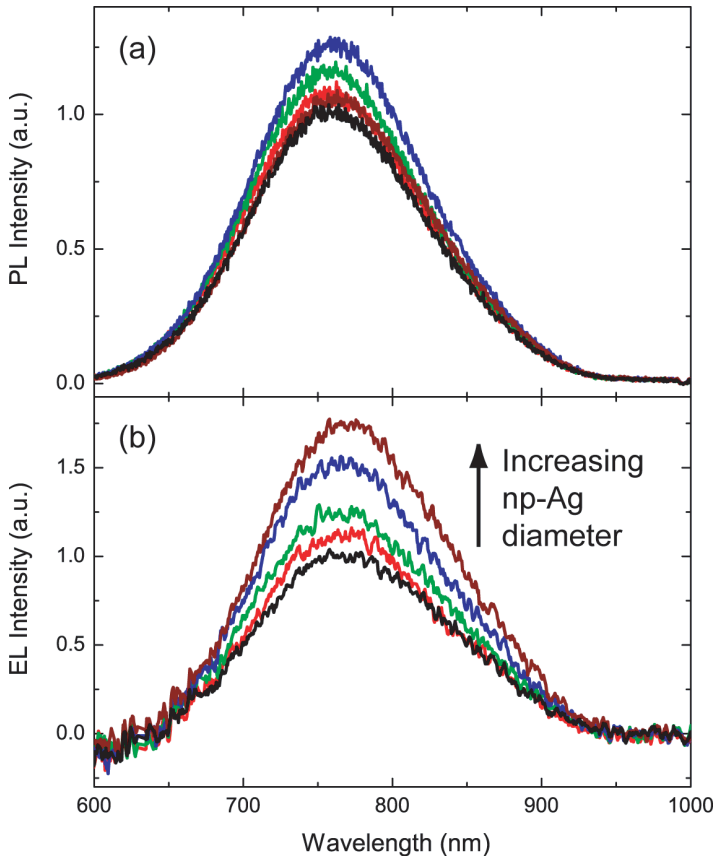

Figure 7.4: (a) Photoluminescence and (b) electroluminescence from nc-Si. Upon coupling to arrays of isolated Ag nanoparticles, the emission intensity increases from that of the reference sample (black curve). For these arrays with fixed 400 nm pitch, the PL and EL emission intensities both increase with increasing particle diameters.

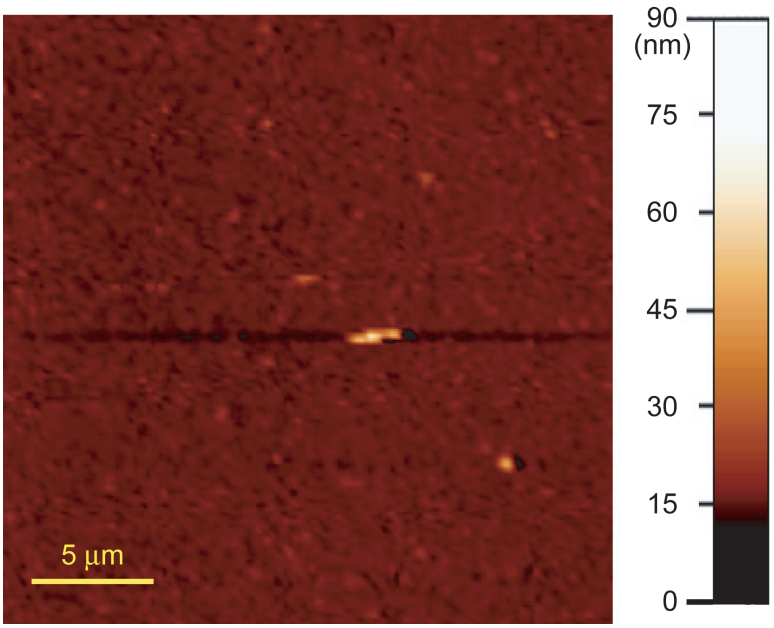

Figure 7.5: 25 μm $\times$ 25 μm atomic force microscope image of the rough poly-Si surface onto which the Ag particles are evaporated, showing an rms surface roughness of $\lesssim$ 5 nm.

face, and not to the metal nanoparticles themselves. Accordingly, we ascribe the phenomenon of increased enhancement with increased diameter to the concomitant increase in surface coverage that is achieved with larger particles.

If increased surface coverage is predicted to yield greater emission enhancements, then coupling nc-Si to a continuous rough Ag film should provide the greatest enhancements. We therefore examined the effect of coupling nc-Si emitters to a 50 μm $\times$ 50 μm continuous Ag film. Figure 7.6(a) shows the EL emission spectra of nc-Si in the absence of Ag (black curve) and when coupled to the 20 nm thick Ag film (red curve). This emission was measured while biasing the FELED with a 5 kHz, 9 V_{rms} signal. The magnitude of enhancement, determined from the ratio of the red and black curves in Fig. 7.6(a), is plotted in Fig. 7.6(b). Here, the EL intensity is enhanced by a factor of up to 2.4, a more important enhancement than was seen for coupling nc-Si to any array of isolated Ag nanoparticles.

To check for EL signal uniformity over the area of the 50 μm $\times$ 50 μm Ag film, as well as over an area where nc-Si is not coupled to Ag, a map of the EL

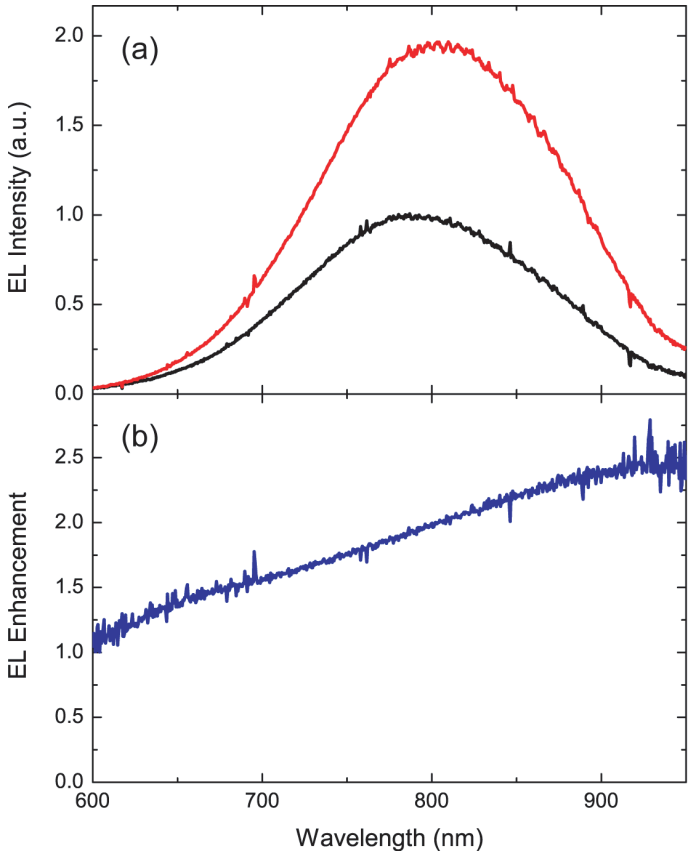

Figure 7.6: (a) Electroluminescence spectrum from nc-Si in a region devoid of Ag (black curve) and coupled to a 20 nm thick continuous rough Ag film (red curve). (b) Magnitude of electroluminescence enhancement, given by the ratio of the red and black curves in (a).

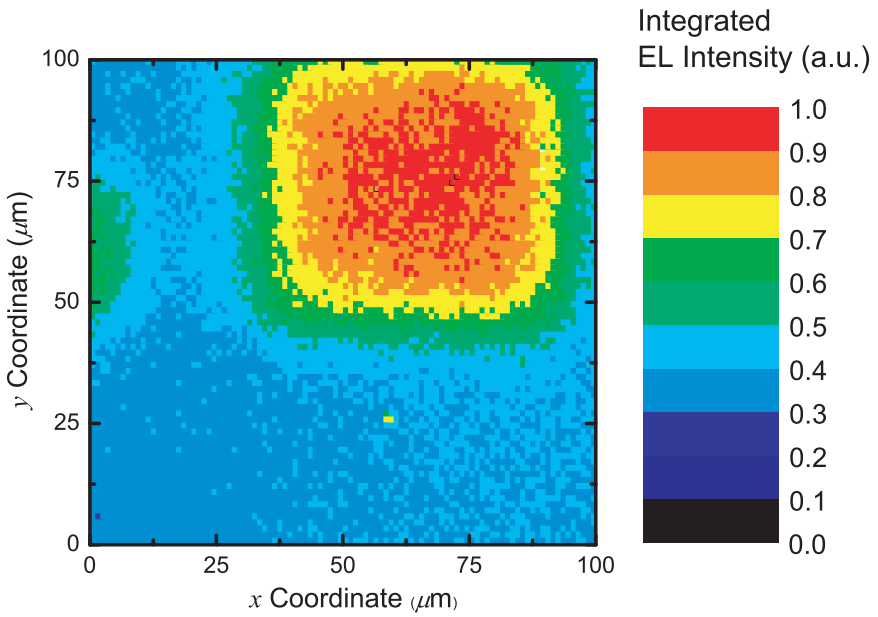

Figure 7.7: EL intensity map over a 100 μm $\times$ 100 μm region of the nc-Si FELED, including a 50 μm $\times$ 50 μm area (top right) where the nc-Si are coupled to a rough Ag film. The emission is integrated from λ = 600-1100 nm.

emission was acquired using the 1340 $\times$ 100 pixel CCD detector in imaging mode. Figure 7.7 shows this map of EL emission intensity, integrated from 600$-$1100 nm. The intensity is constant over the array and roughly double the intensity of emission from nc-Si in the reference region. From this measurement, we infer that the coupled nc-Si emission occurs through the 20 nm thick Ag film.

In the FELED, nc-Si electroluminescence is observed due to the radiative recombination of excitons that are created by the sequential injection of charges into the nanocrystals via Fowler-Nordheim tunneling.[99] The field in the nc-Si-doped SiO_2 tunnel layer depends on the applied gate voltage, so, at greater voltages, Si nanocrystals farther from the source and drain regions can be excited. The EL intensity thus increases with voltage.

An EL enhancement effect that results from the near-field coupling of nc-Si with surface plasmon modes should depend on the separation distance between the nanostructured metal and the Si emitter, as discussed in Chapter 6. The nc-Si attained with higher gate voltages are closer to the top gate and thus nearer

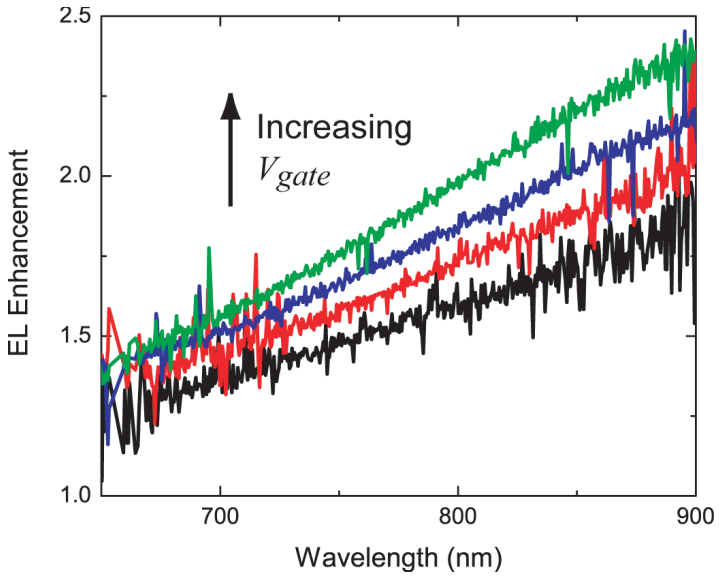

Figure 7.8: EL enhancement as a function of applied gate voltage. The RMS gate voltages are 6, 7, 8, and 9 V (from bottom to top).

to the Ag above that gate. EL enhancements from coupling to plasmonic modes in the rough metal film should therefore increase with voltage. Such a trend was indeed observed for the nc-Si FELEDs. In Fig. 7.8, the EL enhancement is plotted for four different gate voltages between 6 and 9 V_{rms}. Here, the EL enhancement increases with increasing applied voltage, and thus with decreasing Ag/nc-Si separation distances. This effect must therefore be the consequence of near-field electromagnetic coupling.

We finally comment on the nature of the enhancements measured in the present chapter for nc-Si emitters in FELED devices coupled to nanostructured Ag. Unlike the PL enhancements observed in Chapter 5, which were characterized by strong spectral features, in Fig. 7.6, we see only a weak dependence of EL enhancement on emission wavelength. We attribute the weakness of this relationship to the absence of a sharp plasmon resonance in the rough metal film in the wavelength range over which the nc-Si emits. The lack of sharp plasmon resonances may be due to a large spread of feature sizes and shapes in the rough surface, as was the case for the nanoporous gold films of Chapter 4. However, it is equally possible that the rough Ag surfaces that give rise to EL enhancements do have a sharp

plasmon peak, but that the frequency of this peak does not overlap with the emission spectrum. These possibilities deserve further investigation, and future experiments should be designed based on different sample geometries in order to attain resonant enhancements.

7.4 Conclusions

In conclusion, by coupling nc-Si emitters to nanostructured silver, we have observed enhancements in the electroluminescence intensity of nc-Si FELEDs. The voltage dependence of this enhancement indicates that the enhancement is a function of the Ag/nc-Si separation distance. It is therefore consistent with near-field electromagnetic coupling between nc-Si emitters and the enhanced local field about the silver. Because the enhancement increases with increasing Ag nanoparticle diameter, and is greatest for the limiting case of a continuous Ag film, we ascribe the plasmonic effects to features on the rough surface of the Ag nanoparticles and films.

The enhanced electroluminescence demonstrated in this chapter is an exciting and promising result. With improved device design, we can expect resonant interactions between the nc-Si emitters and the Ag plasmon modes, leading to an even greater increase in the EL emission intensity. This is an important step toward fabricating very bright nc-Si LEDs for device integration.

Chapter 8

Conclusions and Outlook

The aim of this thesis was to further our understanding of the photophysics of silicon nanocrystals (nc-Si), a goal which we achieved by a combination of experimental and computational studies. In this work, we began by exploring the role of surface states in the electronic structure of nc-Si, and then we moved on to a thorough investigation of the enhancement of nc-Si emission via near-field coupling to the surface plasmon modes of metal nanostructures.

The most important conclusions that can be drawn from this thesis are the formation of a theoretically predicted, oxygen-related interband surface state on nc-Si, the demonstration of enhanced photoluminescence and electroluminescence from nc-Si in the presence of nanostructured gold and silver, and the ability to predict luminescence enhancement effects with electromagnetic calculations.

8.1 Summary

The surface-state studies are described in Chapter 2. Working with nc-Si made by ion implantation, we developed a selective etching procedure that gave us access to the surface of nanocrystals that are generally protected by an embedding oxide matrix. This process yielded freestanding nc-Si that could be subjected to ambient oxidation. By analyzing the responses of nanocrystals with different sizes to air exposure, we identified that in nc-Si with diameters less than ~ 2.8 nm, oxidation concomitant with a decrease in particle size does not lead to an increase in emission

energy. In this small-nanocrystal size regime, excitonic radiative recombination therefore occurs from a surface state. These experimental results confirmed several theoretical predictions about oxygen-related intergap states. Unfortunately, our investigations of nc-Si surfaces suffered from weak photoluminescence intensities that ultimately limited the measurement signals. This disadvantage motivated the second half of the thesis, which involved an investigation into the plasmon enhancement of nc-Si emission.

Many important results and insights came out of our exploration of plasmon-enhanced emission. The photoluminescence experiments in Chapters 4 and 5 are the first demonstrations of enhanced luminescence from nc-Si. These studies proved that increased emission can be realized in many different experimental configurations; while a thick and rough nanoporous gold film was used to enhance nc-Si emission in Chapter 4, the same effect was achieved by coupling nanocrystals to well-defined arrays of cylindrical silver nanoparticles in Chapter 5. Through the two sets of experiments described in those chapters, we identified many features of plasmon-enhanced luminescence.

Firstly, the enhancement of photoluminescence intensity upon coupling to the plasmon modes of metal nanoparticles is caused by changes in several properties that collectively determine the dynamics of nc-Si emitters. These attributes include the radiative decay rate, the absorbance cross section, and the quantum efficiency. The electromagnetic coupling of nc-Si to metal nanoparticles also leads to an enhancement of the non-radiative decay pathways of the emitter, inducing an increased non-radiative decay rate that can decrease the overall emission. Fortunately, it is possible to access a regime where the beneficial enhancements overcome this adverse consequence. By varying the separation distance between nc-Si and metal nanostructures, we also determined that there is a strong distance dependence to the plasmon enhancement effect; it is therefore readily attributed to near-field electromagnetic coupling. Finally, plasmon enhancement is a resonant process that is strongest at frequencies near the characteristic oscillation frequency of the plasmon mode supported by the metal nanoparticle or nanostructure.

Studying the experimental system with a computational implementation of Maxwell's equations in Chapter 6 further elucidated the electromagnetic interactions that give rise to plasmon-enhanced emission. From this investigation, we found a strong correlation between the local electric field concentration and the extent of plasmon enhancement. As outlined in Chapter 3, previous theoretical treatments of plasmonic interactions have predicted that the radiative decay rate enhancement is proportional to the increase in local field intensity; in this thesis, a comparison of our experimental observations to the results of our computational analysis led us to the same conclusion.

One overarching goal of this project was to demonstrate a bright, silicon-based emitter for integrated optoelectronics. This was only possible after attaining a strong understanding of plasmon-enhanced nc-Si photoluminescence. Following that exploration, in Chapter 7, we applied the notion of plasmon enhancement to nc-Si that were electrically excited via a field-effect mechanism. The nc-Si field-effect light-emitting diodes showed enhanced electroluminescence upon coupling to silver nanostructures. A distance dependence was inferred from the dependence of this enhancement on voltage; this relationship points toward a near-field electromagnetic coupling effect.

8.2 Future Outlook

Though some very exciting new physics were explored in the course of this project, enhancements of more than an order of magnitude were never achieved, even from resonantly tuned systems. This can be attributed to ensemble averaging; unlike surface-enhanced Raman spectroscopy (SERS), which derives from highly non-linear enhancement effects, plasmon-enhanced emission is a linear process, and it therefore depends on the response of the average emitter. In our systems, though some of the nanocrystals were located at positions of high field concentration, the average emitter experienced only a subtly enhanced local electric field. The ensemble analysis done for the results of Chapter 4 and the field profile maps

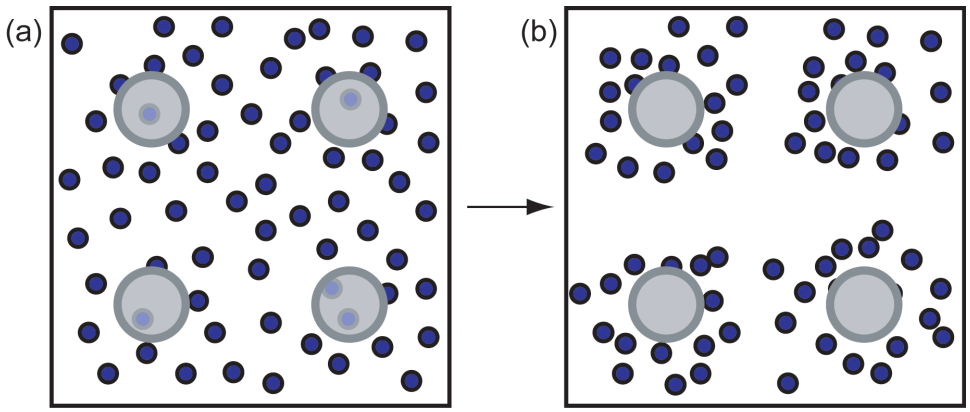

Figure 8.1: A strategy for increasing plasmon enhancements: replacing (a) the layer of randomly distributed nc-Si with (b) a layer in which the nanocrystals are concentrated beneath the metal nanoparticle periphery.

computed in Chapter 6 showed that the variation of enhancement with position can depend on the separation distance between the nanocrystal and the metal surface or the proximity of the emitter to a specific feature, such as a curved particle edge. Additionally, as has been found to be true for SERS, a further analysis of less well-ordered systems would likely demonstrate that large enhancements can be expected for emitters in the near field of "hot spots" like bumps and bends in a rough film.

To observe the greatest effects from the plasmon enhancement of nc-Si luminescence, it will be necessary to improve the metal-semiconductor sample design to more precisely control the relative positions, shapes, and orientations of the components. In this Section, we present several strategies for improving system architecture in order to increase emission from nc-Si.

The simulations in Chapter 6 yielded the field profiles about excited arrays of silver nanoparticles. For example, Fig. 6.8 showed the field profile in the plane of nc-Si 10 nm beneath an array of Ag particles with 135 nm diameter and 400 nm pitch. From this map, it was clear that the field intensity is greatest under the periphery of the nanoparticles, and lowest both far from the nanoparticles and directly beneath the nanoparticles. It is therefore important to let the simulation results guide the design of a new structure. As illustrated in Fig. 8.1(a), in the

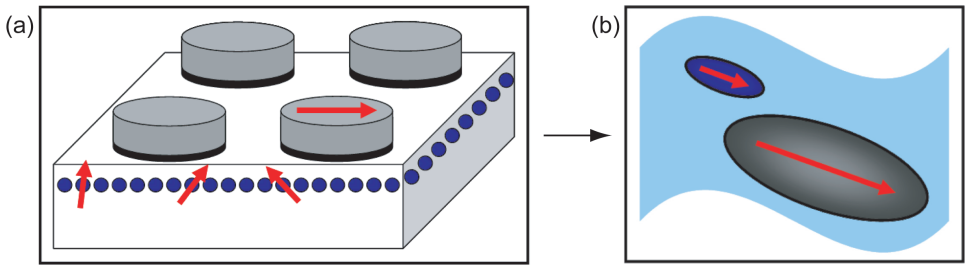

Figure 8.2: A strategy for increasing plasmon enhancements: replacing (a) the current samples, where the nc-Si dipole emitters are randomly oriented with respect to the Ag nanoparticles, with (b) a system of aligned nc-Si and Ag nanoparticles.

present samples, the nc-Si are randomly dispersed throughout their plane. Even while maintaining the structure of Chapter 5, which is composed of coplanar layers of nc-Si and Ag nanoparticles, subtle variations in sample design can yield large improvements in the net extent of plasmon coupling. The simulations of Chapter 6 indicate that a better design is the one schematized in Fig. 8.1(b), where the nc-Si are concentrated beneath the circumference of the metal nanoparticles. Such a structure could be accomplished by invoking an additional lithography step to selectively implant Si^+ in prefered locations, by using metal nanoparticles as a shadow mask for Si^+ implantation, or by using the known effect of locally enhanced heating about metal nanoparticles[100] to selectively nucleate nc-Si only in close proximity to the Ag nanoparticle.

The nc-Si in the present samples are spherical nanocrystals embedded in a homogeneous environment. Therefore, in addition to being located at a distribution of positions relative to the metal nanoparticles, the dipole moments of the nc-Si in the present samples have arbitrary orientations. As indicated in Fig. 8.2(a), at optical frequencies, the metal nanoparticles will be polarized in their plane, while each nc-Si dipole will emit in a different direction. As a result, only a subset of the Si nanocrystals are aligned to experience maximum plasmon enhancement effects. To optimize the coupling between nc-Si and metal nanoparticles, it is desirable to replace this distribution of polarization directions with the case illustrated in Fig. 8.2(b), where the dipole moments of the nc-Si and the metal nanoparticles are all

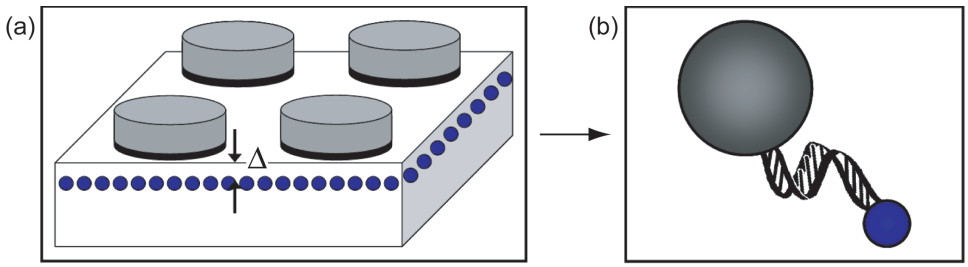

Figure 8.3: A strategy for increasing plasmon enhancements: replacing (a) ensemble averaged measurements with (b) a collection of Si nanocrystals joined to individual Ag nanoparticles at fixed separation distances.

aligned. This could be accomplished by creating systems of aligned anisotropic Si and Ag nanorods, perhaps by the ion irradiation of samples, which has been previously shown to deform metallo-dielectric core/shell colloids.[101] Alternatively, this prefered dipole orientation might be achieved by embedding spherical nc-Si and Ag nanoparticles in a medium with a graded dielectric constant.

Ultimately, to circumvent ensemble averaging, the ideal system for plasmon enhancement is one where each nanocrystal is carefully positioned relative to the metal nanostructures. As schematized in Fig. 8.3, it is desirable to shift from the present case (Fig. 8.3(a)), where the nanocrystals are randomly positioned at an average depth, Δ, to a case in which individual nanocrystals are linked to individual metal nanoparticles (Fig. 8.3(b)) . Strategies for selectively coupling a nanocrystal to a metal particle in a specific position and at a fixed distance can be found in biology.[102] Indeed, the marriage of nano-optoelectronics and biology holds much promise for addressing this challenge; we stand to gain a lot by incorporating biological linker groups such as DNA, which are naturally nanoscale objects, into the design of semiconductor systems.

8.3 Conclusions

The technique of plasmon enhancement is by no means a new one, but it is still a recent arrival in the community of semiconductor quantum dot emitters. It is our hope that the present work, which has explored plasmon-enhanced emission

from nc-Si, predicted potential enhancements of up to two orders of magnitude, and demonstrated plasmon-enhanced nc-Si electroluminescence, will generate more enthusiasm about using plasmonics to enhance the performance of semiconductor emitters. In particular, nc-Si, which are plagued by extremely long radiative lifetimes, have much to gain from these electromagnetic enhancement techniques.

Furthermore, we believe that plasmon enhancement is a powerful and general phenomenon. While the present work may one day lead to the incorporation of a plasmon-enhanced nc-Si light-emitting diode as the optical emitter in a microdevice, it is likely that plasmon enhancement has not yet found its ultimate applications. Some very important advances are yet to come in the field of plasmon-enhanced silicon photonics. One intriguing possibility is the actualization of a plasmon-enhanced solar cell in which nc-Si absorbers are enhanced by the presence of metal nanostructures that double as electrical connectors. Given the current advanced level of nanofabrication, which takes advantage of lithography, self-assembly, and other patterning techniques, and the existing infrastructure for silicon device fabrication, now is the perfect time to further develop plasmon-enhanced silicon photonics. Then, the tools of plasmon enhancement that we have developed in this thesis can bring a new level of sophistication to the field of semiconductor nanocrystal optoelectronics and shine a new light on nc-Si emitters.

Appendix A

Physical and Chemical Manipulations of Freestanding Silicon Nanocrystals

A.1 Introduction

In Chapter 2, freestanding silicon nanocrystals (nc-Si) were deposited on a solid substrate by etching away the SiO_2 matrix in which they were created. The procedure that we developed for the purpose of the oxidation studies in Chapter 2, which involves the implantation of Si^+ ions into SiO_2 followed by a high-temperature anneal before a careful etch in buffered hydrofluoric acid, is outlined in Section 2.2.1. Relative to the embedded nc-Si samples, etched nc-Si turned out to be difficult samples for optical characterization due to their reduced photoluminescence emission, and to the fact that their emission bleaches when photoexcited in air. However, as the etching produces samples of Si nanocrystals adhered by van der Waals forces to a bulk silicon substrate, these supported nanocrystals provide a very flexible system for physical and chemical manipulations using conventional surface science methods. In this appendix, we summarize some of the manipulations that we were able to perform.

A.2 Physical Manipulations of Silicon Nanocrystal Surface Density

The silicon nanocrystals were made by ion implantation of Si^+ ions into a thermal oxide layer on Si(100). The effect of various implantation energies and fluences were determined by the Monte Carlo simulation program SRIM.[40] The average implantation depth is determined by the energy, and the quantity of nanocrystals is determined by the dose. Results for simulations of the implantations used in Chapter 2 and the present appendix are shown in Fig. A.1. By controlling the implantation producing the embedded nanocrystal sample, the structure of the etched sample is determined. The submonolayer coverage etched samples in Chapter 2 were made by implanting 5-keV Si^+ ions to a fluence of 1.3×10^{16} cm^{-2} into 15 nm thick silicon dioxide films (Fig. A.1(a)). Alternatively, we were able to produce samples of many monolayers of nc-Si by beginning from the implantation of 35-keV Si^+ ions to a fluence of 4.0×10^{16} cm^{-2} into 100 nm thick silicon dioxide films.

Figure A.2 shows a non-contact atomic force microscope (AFM) image of the 35-keV Si^+ sample after etching in buffered HF. In contrast to the AFM of the 5-keV Si^+ sample in Fig. 2.2, this AFM shows a high coverage many monolayers thick of silicon nanocrystals with heights $\lesssim$ 5 nm. In order to verify that the nanocrystals were not sintered to the Si substrate, as well as to test the possibility of altering the surface density of nanocrystals, the sample in Fig. A.2 was sonicated in 18 MΩ·cm resistivity water for 5 s and then rinsed in water. Figure A.3 shows the non-contact AFM scan of this sonicated sample: the nanocrystal size remains the same, but their coverage is reduced to less than a monolayer. This result indicates that fine-tuning of nanocrystal density is possible, and that the nanocrystals are physisorbed, not chemically bound, to the surface.

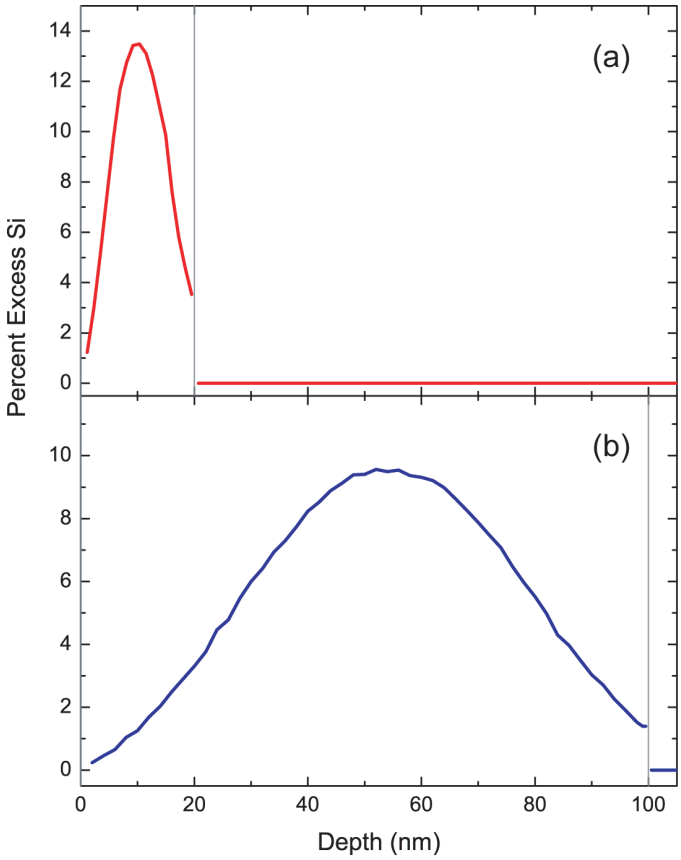

Figure A.1: Simulated ion implantation profiles of Si^+ into a thermal oxide film from Monte Carlo calculations. (a) 5-keV Si^+ ions implanted into 15 nm of SiO_2 18 MΩ·cm resistivity water to a fluence of 1.3×10^{16} cm^{-2}. (a) 35-keV Si^+ ions implanted into 100 nm of SiO_2 to a fluence of 4.0×10^{16} cm^{-2}.

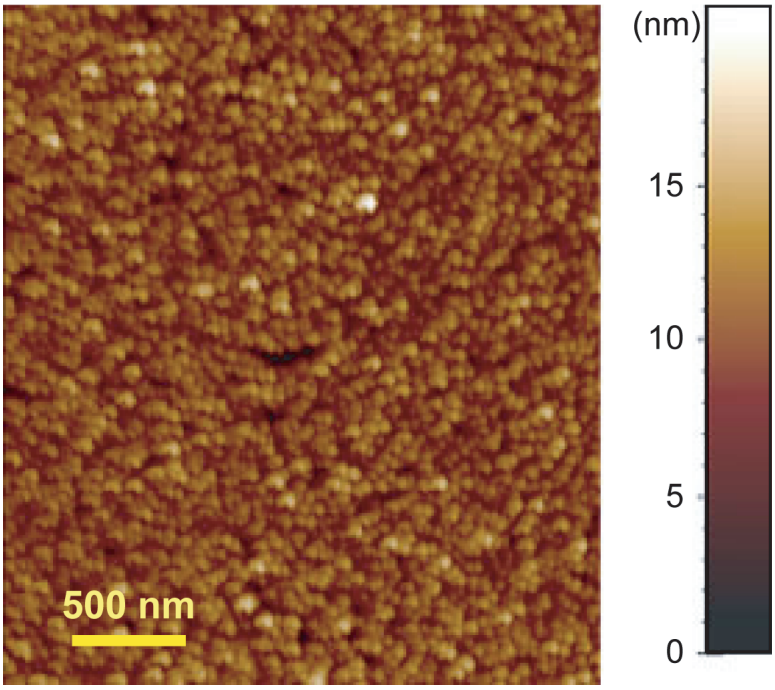

Figure A.2: 2.5 μm $\times$ 3.0 μm non-contact AFM image of nanocrystals made by implanting 35-keV Si^+ ions to 4.0×10^{16} cm^{-2} into 100 nm of SiO_2 and then etching in buffered HF.

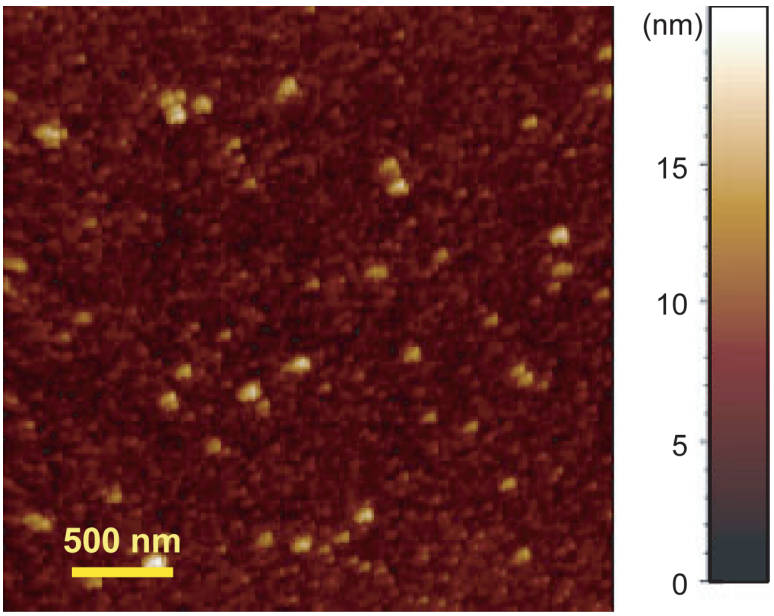

Figure A.3: 3.0 μm $\times$ 3.0 μm non-contact atomic force microscope image of the sample in Fig. A.2 after sonicating for 15 s in acetone and rinsing in 18 MΩ·cm resistivity water.

A.3 Chemical Surface Modifications of Silicon Nanocrystals on a Silicon Support

In samples of silicon nanocrystals created by nucleation and growth in a SiO_2 matrix, the surface Si atoms are generally bound to oxygen. Freshly etched nc-Si surfaces, on the other hand, are terminated by hydrogen atoms, but these systems are not stable toward oxidation in air. Thus, the majority of experimental investigations into the photophysics of nc-Si have focused on oxygen-terminated samples. In order to gain insight into the fundamental properties of indirect band gap semiconductor nanocrystals, as well as to understand experimental results including reports of optical inversion, a reference system that is free of oxygen-related surface states is desired. Bansal et al. and Royea et al. showed that fully methylated bulk silicon surfaces demonstrate enhanced resistance toward oxidation in air, while exhibiting electrochemical properties that are very similar to those of their hydrogenated counterparts.[103–105] We can expect the oxidation rate of well prepared methyl-terminated nc-Si to be similarly slowed, and thus such samples would be conducive to studies in air. This stable system could serve as a substitute for hydrogen-terminated particles in optical measurements, and allow the optical effects intrinsic to the crystal to be studied in an environment free of deep surface states. Methylated nc-Si would also be suitable for device applications where the existence of an insulator such as SiO_2 is undesirable. Finally, synthesizing methylated particles would be a first step toward producing an array of silicon nanocrystals with different surface groups and therefore tailored band gaps for optoelectronic applications.

A.3.1 Surface Chemistry of Silicon Nanocrystals

The exposed surfaces of the etched nanocrystal samples described in Chapter 2 provide a platform not only for the ambient air oxidation studies described in that chapter, but also for preliminary studies of solution chemistry surface modifications. The surface chemistry used for this purpose was adapted from the bulk sur-

face halogenation/Grignard method developed by Bansal et al.[103–105] One important modification from the bulk surface procedure is that the nanocrystal/substrate samples could not be sonicated for cleaning purposes since, as indicated by the change in surface coverage between Figs. A.2 and A.3, such a procedure would remove nanocrystals from the silicon surface. The sonication processing typically used for reactions on bulk silicon surfaces was therefore replaced by a thorough rinsing. Also, care was taken to keep the sample horizontal and face-up in the solution, especially when removing it from a liquid through the meniscus.

The chemical modifications begin as described in Section 2.2.1. Briefly, a sample of nc-Si embedded in 15 nm of SiO_2 is cleaned in a 5:1:1 H_2O:H_2O_2:NH_4OH solution at 80 °C for 10−20 min followed by a rinse in 18 MΩ·cm resistivity water. The nanocrystals are subsequently removed from the SiO_2 and deposited onto the silicon substrate with a 40 s chemical etch in buffered hydrofluoric acid (7.2% HF(aq), 36% NH_4F(aq) v/v), with great care taken to hold the samples horizontally as they are removed from the etching solution. This first step produces hydrogen-terminated silicon nanocrystals on a H-terminated silicon (100) substrate.

The H-terminated nc-Si are then introduced into a nitrogen-purged glove box for the subsequent processing steps. In this oxygen-free environment, the surfaces of nc-Si supported on the Si substrate are chlorinated by heating in a saturated solution of PCl_5 in chlorobenzene with a few grains of the radical initiator benzoyl peroxide, at 90−100 °C for 45 min. This produces chlorine-terminated nc-Si on a Si substrate, which are cleaned by rinsing in anhydrous tetrahydrofuran (THF) and anhydrous methanol, and dried under flowing N_2 gas. Still in the nitrogen-purged environment, the chlorine-terminated sample is immersed in a 3.0 M solution of CH_3MgBr in diethyl ether. The reaction solution is heated at 70−80 °C for 2.5 h. The methyl-terminated nanocrystals on a methyl-terminated Si(100) surface are cleaned by rinsing in anhydrous THF and anhydrous methanol.

A non-contact AFM scan of a sample after this chlorination/methylation sequence is shown in Fig. A.4. This scan shows that silicon nanocrystals remain on

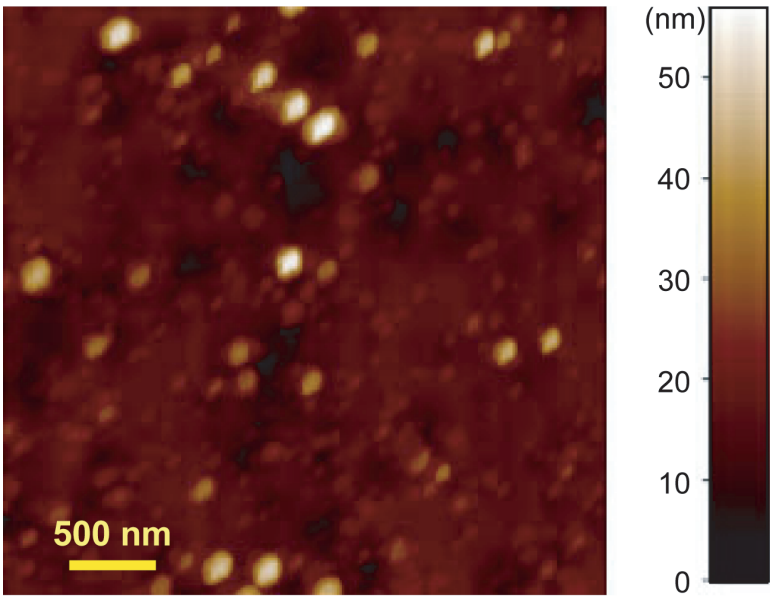

Figure A.4: 3.5 μm $\times$ 3.5 μm non-contact atomic force microscope image of silicon nanocrystals on a silicon substrate after the chlorination and methylation reactions.

the surface despite the numerous reaction and rinsing steps involved. However, the sample appears dirtier than prior to chemical reactions. Still, AFM indicates that there is some potential for using substrate-supported nc-Si in chemical reactions, since nanocrystals remain on the surface despite exposure to harsh reagents, high temperatures, and multiple rinses.

A.3.2 X-Ray Photoelectron Spectroscopy

Given that the chemically modified samples consist of a submonolayer coverage of silicon nanocrystals on a silicon substrate, it was impossible to use X-ray photoelectron spectroscopy (XPS) to probe the nanocrystals alone; XPS is unable to discern the surface chemistry of the nc-Si from that of the Si(100) base on which they were deposited. However, we could still use XPS to monitor the surface chemistry of the Si substrate/Si nanocrystal combination. Previous studies on bulk (111) and (100) silicon have determined that, though a hydrogen-terminated silicon surface will oxidize in air within minutes, surface methylation confers resistance to such oxidation.[103–105] We therefore used XPS to probe whether the same

behavior could be observed in the methylated Si substrate/Si nanocrystal sample.

The Si(2p) region of the XP spectrum shows up at 99−105 BeV, and we look for signatures of the surface chemistry in core level shifts in this signal. The Si (2p) binding energy increases steadily with oxidation state, from 99.3 BeV for Si^0 to 103.3 BeV for the Si^{4+} oxidation state.[45] As was shown in Fig. 2.5, upon removal from the buffered HF etching solution, the XP spectrum of Si substrates with Si nanocrystals contains a single peak at 99.5 BeV, demonstrating that the nanocrystals and the Si surface were oxide-free. However, left in air, these samples oxidized within minutes. Fig. A.5(a) shows the XP spectrum of a sample of Si nanocrystals on Si(100) one week after hydrogen-termination by etching in BHF. This Si(2p) signal has two components: a peak centered at 99.5 BeV from unoxidized Si, and a peak at 103.5 BeV indicating a large degree of surface oxidation. Since a monolayer of silicon is $\sim$ 0.6 nm thick and the XPS escape depth is $\sim$ 3.0 nm, this spectrum is consistent with the growth of a full monolayer of native silicon oxide on the surfaces of the nanocrystals and the substrate . In contrast, Fig. A.5(b) shows the XPS spectrum of a sample of methylated silicon nanocrystals on silicon after one week in air; a comparison of this scan to the one in Fig. A.5(a) shows no evidence of oxidation. This is consistent with the methylation reaction being a successful way to prevent the oxidation of the surface of silicon nanocrystals.

A.3.3 Photoluminescence Spectroscopy

Optoelectronic characterization by photoluminescence (PL) spectroscopy was used to monitor the effect of the surface modifications on the silicon nanocrystals. This technique can indicate the presence or absence of covalently bonded groups on the surface of defect-free nanocrystals as described in Chapter 2. It is also a good indicator of the quality of the nanocrystal, since defects such as dangling bonds will quench the band-to-band PL and themselves luminesce at 500−600 nm.[42] Figure A.6 shows the PL spectra of samples at different stages of the methylation sequence. All of the unembedded samples were examined one week after chemical treatment, by which point we expect the hydrogen- and chlorine-

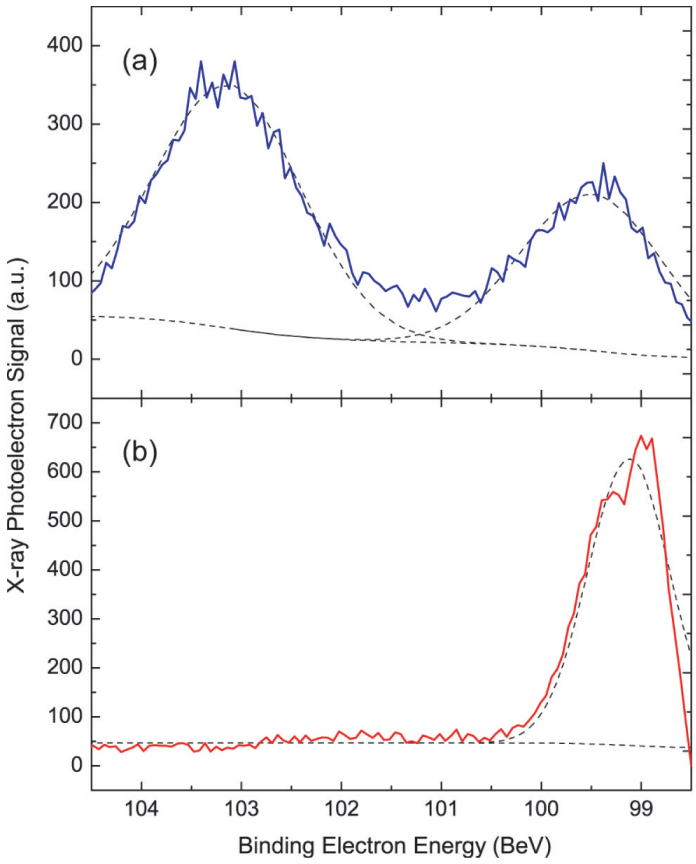

Figure A.5: XP spectra of Si nanocrystals on Si(100) substrate (a) one week in air after hydrogen termination by etching and (b) one week in air after methylation.

terminated samples to be oxidized. The PL spectrum from the initial sample of silicon nanocrystals embedded in SiO_2 is given in Fig. A.6(a). This sample emits with a peak at 775 nm, consistent with the radiative recombination of quantum confined excitons of Si nanocrystals in the 3 to 4 nm diameter size regime. Figure A.6(b) shows the PL spectrum of a similar sample that was stored in ambient air for one week after it was etched and H-terminated. This sample emits with a peak at 725 nm, consistent with radiative recombination of quantum confined excitons of Si nanocrystals that are smaller than the nanocrystals in Fig. A.6 due to the etching process.

Figures A.6(c) and (d) show the PL spectra of samples one week after chlorine-termination and methyl-termination, respectively. Unfortunately, though AFM indicates that there are indeed nanocrystals present in these samples, we see no emission from quantum-confined excitons in Figs. A.6(c) and (d), only emission at ~ 550 nm, with a PL decay lifetime of < 400 ns, that is characteristic of defect state emission. The chlorination and methylation procedures clearly damage the nanocrystals to the point where their emission was no longer observed and a less harsh variation on the techniques described in this appendix must be developed to produce defect-free surface-functionalized silicon nanocrystals.

A.4 Silicon Nanocrystals on Fused Silica Substrates

It is convenient to utilize the well-developed method of creating silicon nanocrystals in silicon dioxide via Si^+ ion implantation and annealing. However, it is difficult to characterize silicon nanocrystals on a silicon substrate by XPS, and impossible to measure the UV-visible absorption of nanocrystals on such opaque samples. As an attempt to circumvent such challenges while still taking advantage of using a Si-doped SiO_2 precursor, we examined the possibility of creating samples of silicon nanocrystals supported on fused silica rather than silicon. For this purpose, fused silica substrates were implanted with Si^+ ions. Annealing such samples in Ar at 1100 °C as was done with the SiO_2-on-silicon samples did not yield photo-

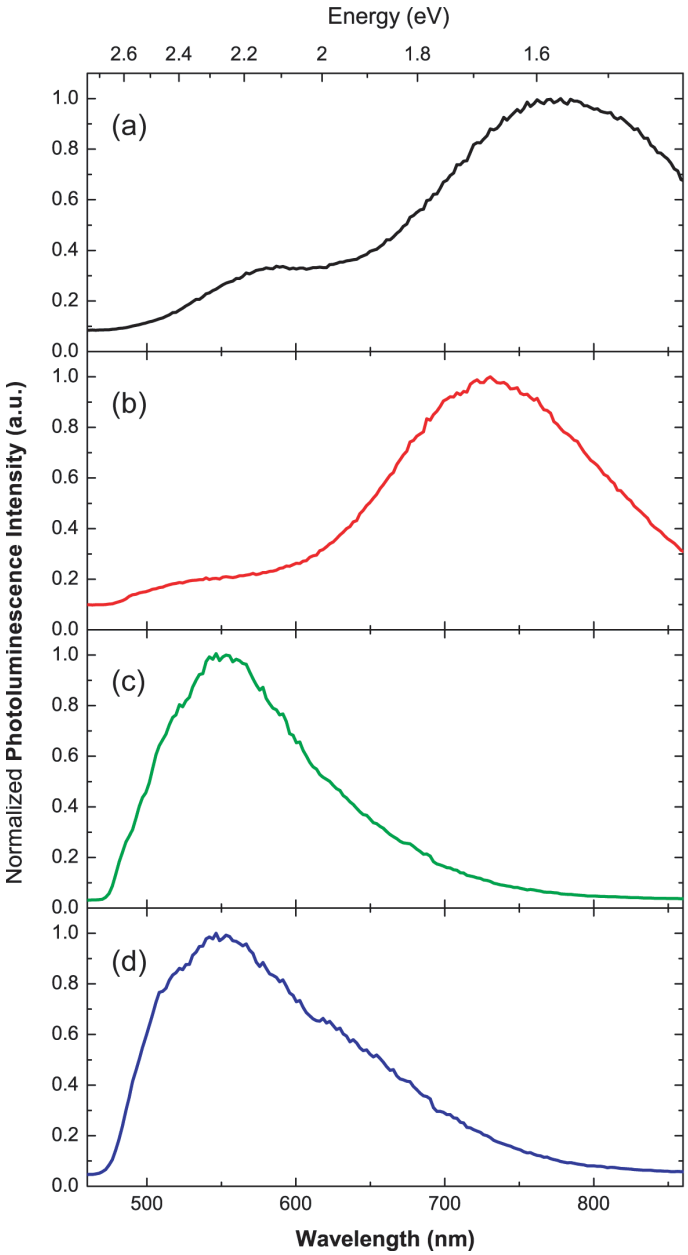

Figure A.6: Photoluminescence spectra at samples at various stages of chemical manipulations. (a) Silicon nanocrystals embedded in SiO_2. (b) One week in air after silicon nanocrystals have been removed from SiO_2 and hydrogen-terminated through etching. (c) One week in air after hydrogen-terminated samples have been chlorine-terminated in PCl_5 with benzoyl peroxide. (d) One week in air after chlorine-terminated samples have been methyl-terminated in methyl magnesium bromide.

luminescent samples, implying that no nanocrystals were formed in the silica. We attribute this to the complete oxidation of the implanted silicon, presumably due to the increased wetting of fused silica relative to that of a thin oxide on Si, and develop some small modifications to address this difference. In particular, rather than annealing the Si^+-doped silica in Ar at 1100 °C for 5 min, the fused silica samples were annealed in Ar at 250 °C for 20 min, then 450 °C for 20 min to dry the samples, and subsequently annealed in Ar at 1000 °C for 30 min to nucleate and grow nanocrystals. According to PL spectroscopy, this produced embedded silicon nanocrystals in the silica.

Due to the high surface sensitivity of the XPS technique, the Si(2p) region of such a sample (not shown) shows only a Si^{4+} peak at 104 BeV from the fused silica; the embedded nanocrystals are hidden from the X-ray beam and cannot be detected. Etching away the surface SiO_2 in these samples would be expected to leave silicon nanocrystals supported by an all-SiO_2 base, and in an XPS measurement of this combination, any unoxidized Si signal can be attributed to the silicon nanocrystal cores. The XP spectrum of this sample after 30, 60, or 90 s of etching in buffered HF (BHF) are displayed in Fig. A.7, and the insets of this figure show a schematic of our interpretation of the evolution of the sample with etch time. Etching for 30 s in BHF gave rise to a partially etched sample with silicon nanocrystals mostly uncovered but not making up the entire surface. Figure A.7(a) shows the XP spectrum of the Si(2p) region of such a sample; there is a large bulk Si^0 peak at 100 BeV and a small Si^{4+} peak from SiO_2 at 104 BeV. Figure A.7(b) shows the same region for a sample that has been etched for 60 s; here, the Si(2p) region shows only a Si^0 peak at 100 BeV, implying that the entire surface consists of silicon nanocrystals. Finally, after a 90 s etch in buffered HF, the nanocrystals are entirely washed off the surface of the fused silica; the XP spectrum of such a sample in Fig. A.7(c) has a signal that originates only from the oxidized Si^{4+} of SiO_2.

The differences in hydrophobicity between silicon and SiO_2 decrease the likelihood that nanocrystals will remain on the SiO_2 substrate when immersed in a

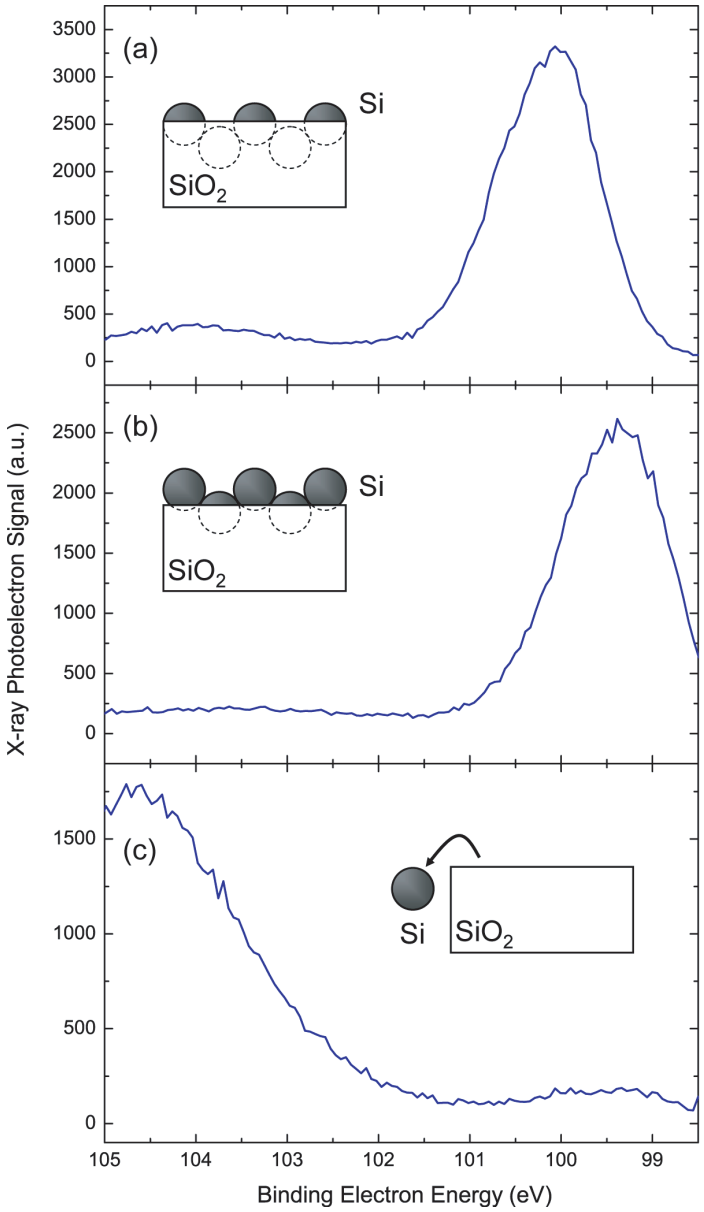

Figure A.7: XP spectra of a sample of silicon nanocrystals in fused silica immediately after (a) 30 s immersion in buffered hydrofluoric acid (BHF), (b) 60 s immersion in BHF, (c) 90 s immersion in BHF. The insets are schematics of sample configurations consistent with the XP spectra.

solution. Indeed, it seems that only partially embedded nc-Si remain on the surface at all; fully freestanding nanocrystals are washed away. This makes silicon nanocrystals on a silica substrate unsuitable for chemical modifications, during which it is desirable to have access to the entire nanocrystal surface.

A.5 Conclusions

This appendix summarized the various physical and chemical manipulations we attempted during the course of our investigations of freestanding silicon nanocrystals prepared by the selective etching of nc-Si-doped SiO_2. Though perhaps not an ideal technique, this method still does produce freestanding nc-Si that are available for nanocrystal surface studies. There exist several colloidal[106–109] and aerosol[110–113] chemistry synthetic methods for the fabrication of silicon nanocrystals with diameters less than $\lesssim 5$ nm, yet these techniques are in their infancy. It is therefore desirable to take advantage of existing, well-developed methods for the synthesis of silicon nanocrystals within silicon dioxide. Hopefully the techniques outlined here will be of use for further surface chemistry and single-particle studies.

Appendix B

Mathematical Model for Deconvolving Ensemble Measurements

B.1 Introduction

In Section 4.4.4, we record the photoluminescence (PL) intensity, I_{PL}; absorbance cross section, σ; experimental decay rate, Γ_{exp}; radiative decay rate, Γ_{rad}; and quantum efficiency, Q, from silicon nanocrystals (nc-Si) coupled to nanoporous gold (np-Au). Each of these optoelectronic properties is dependent on the metal/ semiconductor separation distance, which is varied by increasing the etch depth, D. The enhancements of these factors, i.e., η_{PL}, η_{σ}, $\eta_{\Gamma_{exp}}$, $\eta_{\Gamma_{rad}}$, and η_{Q}, respectively, are plotted as a function of D in Figs. 4.13, 4.15, 4.17, 4.18, and 4.19, respectively.

In all cases, these enhancements peak at 7.5 nm $< D <$ 12.5 nm, and have a rising tail at $D \sim 17.5{-}20$ nm. Our results can be interpreted in the context of a model that accounts for local-field effects as well as the spatial distribution of nanocrystals in the sample. The nanocrystals closest to the np-Au will be most affected by its presence because the strength of the enhanced local field is expected to decay with metal/emitter separation distance, r, as r^{-6}. At extremely small nc-Si/np-Au separations, however, luminescence quenching processes must be considered,[74] and if np-Au directly contacts a Si nanocrystal, electronic charge transfer could also quench luminescence.[9] The green lines in Figs. 4.13, 4.15, 4.17, 4.18, and 4.19 are fits produced by applying this model to our data, and we describe

the model in the present appendix.

B.2 Model for the Quantitative Analysis of Ensemble Results

From a qualitative perspective, the non-monotonic trends in enhancements in Figs. 4.13, 4.15, 4.17, 4.18, and 4.19, including the rising tail at $D \sim 20$ nm, is unsurprising when the bimodal distribution of 780 nm emitters within the nc-Si distribution, indicated in the red curve of Fig. 4.7, is considered. We interpret the trend quantitatively in the context of a model that accounts for three important factors. Firstly, the spatial distribution of 780 nm emitters, N, introduced in Eq. (4.2) as a function of the distance from the unetched surface, d, is reformulated as a function of etch depth, D, and metal/emitter separation distance in the etched sample, $r = d - D$, i.e.,

$$N(r,D) = N_{total}(r,D) \times \left\{ \exp\left[\frac{-2}{(7.05)^2} \cdot ((r+D) - 9.6)^2\right] + \exp\left[\frac{-2}{(7.05)^2} \cdot ((r+D) - 28.8)^2\right] \right\} \quad \text{(B.1)}$$

where

$$N_{total}(r,D) = \exp\left\{\frac{-2}{(14.1)^2} \cdot ((r+D) - 19.2)^2\right\} \quad \text{(B.2)}$$

Secondly, we consider that the Si nanocrystals are subjected to a field that is the sum of the applied field, E_{app} and the enhanced local field. The latter decays from its maximum value of $f_{enh} \cdot E_{app}$, where f_{enh} is the enhancement factor, with r as r^{-6}. The total field is then

$$\frac{E(r)}{E_{app}} = f_{enh} \cdot r^{-6} + 1 \quad \text{(B.3)}$$

Thirdly, we consider that, at extremely small nc-Si/np-Au separations, luminescence quenching processes occur,[74] and if np-Au directly contacts a Si nanocrystal, electronic charge transfer can also quench luminescence.[9] We approximate

that these mechanisms act to quench all luminescence over a dead zone of width, z.

We monitor the evolution of enhancements of five different physical properties, η_{PL}, η_{σ}, $\eta_{\Gamma_{exp}}$, $\eta_{\Gamma_{rad}}$, and η_{Q}. Each one is enhanced in a field, $E(r)$, according to its own constant interaction factor, which we designate as χ_{PL}, χ_{σ}, $\chi_{\Gamma_{exp}}$, $\chi_{\Gamma_{rad}}$, and χ_{Q}, respectively.

The enhancement in PL intensity, $\eta_{PL}(D)$, is the ratio of the sum of enhanced intensities (integrated from $z \leq r < \infty$ because emission is quenched at positions $r \leq z$) to the sum of the reference intensities. This enhancement is therefore given by

$$\eta_{PL}(D) = \frac{\chi_{PL} \int_z^\infty drN(r,D)E(r)}{\int_0^\infty drN(r,D)} \tag{B.4}$$

Whereas the measured photoluminescence intensity is the sum of emission intensity from each nanocrystal, measurements of the other optical properties considered in this appendix and in Chapter 4 detect average values, and the functional form of their enhancements is slightly different from η_{PL} in Eq. (B.4). The enhancement in absorbance cross section, η_{σ}, is

$$\begin{aligned} \eta_{\sigma}(D) &= \frac{\chi_{\sigma} \int_z^\infty drN(r,D)E(r) / \int_z^\infty drN(r,D)}{\int_0^\infty drN(r,D) / \int_0^\infty drN(r,D)} \\ &= \frac{\chi_{\sigma} \int_z^\infty drN(r,D)E(r)}{\int_z^\infty drN(r,D)} \end{aligned} \tag{B.5}$$

The enhancement in experimental decay rate, $\eta_{\Gamma_{exp}}$, radiative decay rate, $\eta_{\Gamma_{rad}}$, and quantum efficiency, η_{Q}, are, respectively,

$$\eta_{\Gamma_{exp}}(D) = \frac{\chi_{\Gamma_{exp}} \int_z^\infty drN(r,D)E(r)}{\int_z^\infty drN(r,D)} \tag{B.6}$$

$$\eta_{\Gamma_{rad}}(D) = \frac{\chi_{\Gamma_{rad}} \int_z^\infty drN(r,D)E(r)}{\int_z^\infty drN(r,D)} \tag{B.7}$$

$$\eta_Q(D) = \frac{\chi_Q \int_z^\infty drN(r,D)E(r)}{\int_z^\infty drN(r,D)} \tag{B.8}$$

B.3 Conclusions and Predictions

The data of Figs. 4.13, 4.15, 4.17, 4.18, and 4.19 were fit to the predicted trends of Eqs. (B.4)−(B.8). Two very interesting quantities can be deduced from these fits. Firstly, this analysis determines the dead zone width, z. The best fits obtained with our model give $z = 1.6$ nm. In other words, at metal/semiconductor separation distances less than 1.6 nm, quenching processes become more important than enhancement effects, and the emission is decreased.

Secondly, fitting our data to this model gives us the interaction factors, χ_{PL}, χ_σ, $\chi_{\Gamma_{exp}}$, $\chi_{\Gamma_{rad}}$ and χ_Q. A significant limitation on the enhancement magnitudes attained in Chapter 4 is the wide distribution in nanocrystal positions. The optical phenomena reported in the present appendix and in Chapter 4 contain some contributions from Si nanocrystals strongly coupled to np-Au, but we cannot neglect the large contribution from non-interacting nanocrystals far from the np-Au. With the present distribution, $N(r,D)$ in Eq. (B.1), we measure a maximum of $\eta_{PL} \sim 4$ at $D = 10$ nm. Replacing $N(r, D = 10\,\text{nm})$ by an idealized, much narrower, distribution of emitters,

$$N'(r) = \exp\left\{\frac{-2}{(14.1)^2} \cdot (r - 1.75)^2\right\} \tag{B.9}$$

yields a PL intensity enhancement, η_{PL}, greater than 50.

Despite the fact that the measurements in Chapter 4 are obscured and dampened by the wide distribution of silicon nanocrystal positions in the sample, the analysis in the present appendix gives good insight for the design of more idealistic coupled metal/semiconductor systems. We predict that with close coupling

($\sim$ 1.6 nm separation distances) and narrowing spatial distributions, a much larger enhancement can be obtained in a system very similar to the one at hand.

Bibliography

[1] G. E. Moore, Electronics **38**, 114 (1965).

[2] Sematech, *International Technology Roadmap for Semiconductors*, 2005.

[3] J. S. Kilby, IEEE Transactions on Electron Devices **23**, 648 (1976).

[4] L. T. Canham, Applied Physics Letters **57**, 1046 (1990).

[5] A. G. Cullis and L. T. Canham, Nature **353**, 335 (1991).

[6] J. Valenta, R. Juhasz, and J. Linnros, Applied Physics Letters **80**, 1070 (2002).

[7] Z. H. Lu, D. J. Lockwood, and J. M. Baribeau, Nature **378**, 258 (1995).

[8] N. Lalic and J. Linnros, Journal of Luminescence **80**, 263 (1998).

[9] R. J. Walters, G. I. Bourianoff, and H. A. Atwater, Nature Materials **4**, 143 (2005).

[10] A. Irrera, D. Pacifici, M. Miritello, G. Franz, F. Priolo, F. Iacona, D. Sanfilippo, G. Di Stefano, and P. G. Fallica, Applied Physics Letters **81**, 1866 (2002).

[11] T. Shimizu-Iwayama, S. Nakao, and K. Saitoh, Applied Physics Letters **65**, 1814 (1994).

[12] L. E. Brus, P. F. Szajowski, W. L. Wilson, T. D. Harris, S. Schuppler, and P. H. Citrin, Journal of the American Chemical Society **117**, 2915 (1995).

[13] Q. Zhang, S. C. Bayliss, and D. A. Hutt, Applied Physics Letters **66**, 1977 (1995).

[14] M. Zacharias, J. Heitmann, R. Scholz, U. Kahler, M. Schmidt, and J. Blasing, Applied Physics Letters **80**, 661 (2002).

[15] B. Delley and E. F. Steigmeier, Physical Review B **47**, 1397 (1993).

[16] A. G. Cullis, L. T. Canham, and P. D. J. Calcott, Journal of Applied Physics **82**, 909 (1997).

[17] J. P. Proot, C. Delerue, and G. Allan, Applied Physics Letters **61**, 1948 (1992).

[18] L. Brus, Journal of Physical Chemistry **90**, 2555 (1986).

[19] S. Schuppler, S. L. Friedman, M. A. Marcus, D. L. Adler, Y. H. Xie, F. M. Ross, Y. J. Chabal, T. D. Harris, L. Brus, W. L. Brown, E. E. Chaban, P. F. Szajowski, S. B. Christman, and P. H. Citrin, Physical Review B **52**, 4910 (1995).

[20] Y. Kanemitsu, H. Uto, Y. Masumoto, T. Masumoto, T. Futagi, and H. Mimura, Physical Review B **48**, 2827 (1993).

[21] M. V. Wolkin, J. Jorne, P. M. Fauchet, G. Allan, and C. Delerue, Physical Review Letters **82**, 197 (1999).

[22] A. Puzder, A. J. Williamson, J. C. Grossman, and G. Galli, Physical Review Letters **88**, 097401 (2002).

[23] A. Puzder, A. J. Williamson, J. C. Grossman, and G. Galli, Journal of Chemical Physics **117**, 6721 (2002).

[24] R. J. Walters, J. Kalkman, A. Polman, H. A. Atwater, and M. J. A. De Dood, Physical Review B **73**, 132302 (2006).

[25] R. Espiau de Lamaëstre, H. Bernas, D. Pacifici, G. Franzò, and F. Priolo, Applied Physics Letters **88**, 181115 (2006).

[26] X. Brokmann, L. Coolen, M. Dahan, and J. P. Hermier, Physical Review Letters **93**, 107403 (2004).

[27] G. S. Solomon, M. Pelton, and Y. Yamamoto, Physical Review Letters **86**, 3903 (2001).

[28] M. Fujii, M. Yoshida, Y. Kanzawa, S. Hayashi, and K. Yamamoto, Applied Physics Letters **71**, 1198 (1997).

[29] P. G. Kik, M. L. Brongersma, and A. Polman, Applied Physics Letters **76**, 2325 (2000).

[30] K. S. Min and H. A. Atwater, Applied Physics Letters **72**, 1884 (1998).

[31] R. Ragan, K. S. Min, and H. A. Atwater, Materials Science and Engineering B **87**, 204 (2001).

[32] M. Fleischmann, P. J. Hendra, and A. J. McQuillan, Chemical Physics Letters **26**, 163 (1974).

[33] J. Gersten and A. Nitzan, Journal of Chemical Physics **73**, 3023 (1980).

[34] A. M. Glass, P. F. Liao, J. G. Bergman, and D. H. Olson, Optics Letters **5**, 368 (1980).

[35] K. T. Shimizu, W. K. Woo, B. R. Fisher, H. J. Eisler, and M. G. Bawendi, Physical Review Letters **89**, 117401 (2002).

[36] O. Kulakovich, N. Strekal, A. Yaroshevich, S. Maskevich, S. Gaponenko, I. Nabiev, U. Woggon, and M. Artemyev, Nano Letters **2**, 1449 (2002).

[37] K. Okamoto, I. Niki, A. Shvartser, Y. Narukawa, T. Mukai, and A. Scherer, Nature Materials **3**, 601 (2004).

[38] L. Pavesi, L. Dal Negro, C. Mazzoleni, G. Franz, and F. Priolo, Nature **408**, 440 (2000).

[39] M. H. Nayfeh, S. Rao, N. Barry, J. Therrien, G. Belomoin, A. Smith, and S. Chaieb, Applied Physics Letters **80**, 121 (2002).

[40] J. F. Ziegler, J. P. Biersack, and U. Littmark, *The Stopping and Range of Ions in Solids*, Volume 1, Pergamon Press, New York, 1985.

[41] K. S. Min, K. V. Shcheglov, C. M. Yang, H. A. Atwater, M. L. Brongersma, and A. Polman, Applied Physics Letters **69**, 2033 (1996).

[42] K. S. Min, K. V. Shcheglov, C. M. Yang, H. A. Atwater, M. L. Brongersma, and A. Polman, Applied Physics Letters **68**, 2511 (1996).

[43] M. L. Brongersma, A. Polman, K. S. Min, E. Boer, T. Tambo, and H. A. Atwater, Applied Physics Letters **72**, 2577 (1998).

[44] T. Feng, *Silicon Nanocrystal Charging Dynamics and Memory Device Applications*, Ph.D. thesis, California Institute of Technology, 2005.

[45] J. F. Moulden, W. F. Stickle, P. E. Sobol, and K. D. Bomben, *Handbook of X-Ray Photoelectron Spectrocopy*, Perkin-Elmer Corporation, Eden Prairie, MN, 1992.

[46] M. S. Hybertsen, Physical Review Letters **72**, 1514 (1994).

[47] Y. Kanemitsu, Physics Reports **263**, 1 (1995).

[48] F. Lukeš, Surface Science **30**, 91 (1972).

[49] F. Zhou and J. D. Head, Journal of Physical Chemistry B **104**, 9981 (2000).

[50] Y. J. Chabal, K. Raghavachari, X. Zhang, and E. Garfunkel, Physical Review B **66**, 161315(R) (2002).

[51] M. Faraday, Philosophical Transactions of the Royal Society of London **147**, 145 (1857).

[52] G. Mie, Annalen Der Physik **25**, 377 (1908).

[53] D. L. Jeanmaire and R. P. Van Duyne, Journal of Electroanalytical Chemistry **84**, 1 (1977).

[54] M. G. Albrecht and J. A. Creighton, Journal of the American Chemical Society **99**, 5215 (1977).

[55] S. A. Maier, P. G. Kik, H. A. Atwater, S. Meltzer, E. Harel, B. E. Koel, and A. A. G. Requicha, Nature Materials **2**, 229 (2003).

[56] A. Wokaun, D. J. Bergman, J. P. Heritage, A. M. Glass, P. F. Liao, and D. H. Olson, Physical Review B **24**, 849 (1981).

[57] C. J. Chen and R. A. Osgood, Physical Review Letters **50**, 1705 (1983).

[58] S. Nie and S. R. Emory, Science **275**, 1102 (1997).

[59] M. Moskovits, Reviews of Modern Physics **57**, 783 (1985).

[60] M. Kerker, D.-S. Wang, and H. Chew, Applied Optics **19**, 4159 (1980).

[61] J. Gersten and A. Nitzan, Journal of Chemical Physics **75**, 1139 (1981).

[62] A. Wokaun, H.-P. Lutz, A. P. King, U. P. Wild, and R. R. Ernst, Journal of Chemical Physics **79**, 509 (1983).

[63] J. Kümmerlen, A. Leitner, H. Brunner, F. R. Aussenegg, and A. Wokaun, Molecular Physics **80**, 1031 (1993).

[64] C. D. Geddes and J. R. Lakowicz, Journal of Fluorescence **12**, 121 (2002).

[65] P. C. Das and A. Puri, Physical Review B **65**, 155416 (2002).

[66] L. A. Blanco and F. J. Garcìa de Abajo, Journal of Quantitative Spectroscopy & Radiative Transfer **89**, 37 (2004).

[67] I. A. Larkin, M. I. Stockman, M. Achermann, and V. I. Klimov, Physical Review B **69**, 121403(R) (2004).

[68] D. V. Guzatov and V. V. Klimov, Chemical Physics Letters **412**, 341 (2005).

[69] T. Nakamura and S. Hayashi, Japanese Journal of Applied Physics **44**, 6833 (2005).

[70] R.R. Chance, A. Prock, and R. Silbey, Journal of Chemical Physics **62**, 2245 (1975).

[71] A. Kramer, W. Trabesinger, B. Hecht, and U. P. Wild, Applied Physics Letters **80**, 1652 (2002).

[72] W. Trabesinger, A. Kramer, M. Kreiter, B. Hecht, and U. P. Wild, Applied Physics Letters **81**, 2118 (2002).

[73] E. Dulkeith, M. Ringler, T. A. Klar, J. Feldmann, A. Muñoz Javier, and W. J. Parak, Nano Letters **5**, 585 (2005).

[74] P. Anger, P. Bharadwaj, and L. Novotny, Physical Review Letters **96**, 113002 (2006).

[75] N. E. Hecker, R. A. Höpfel, N. Sawaki, T. Maier, and G. Strasser, Applied Physics Letters **75**, 1577 (1999).

[76] A. Neogi, C.-W. Lee, H. O. Everitt, T. Kuroda, A. Tackeuchi, and E. Yablonovitch, Physical Review B **66**, 153305 (2002).

[77] A. Neogi, H. Morkoç, T. Kuroda, and A. Tackeuchi, Optics Letters **30**, 93 (2005).

[78] I. Honma, T. Sano, and H. Komiyama, Journal of Physical Chemistry **97**, 6692 (1993).

[79] S. A. Maier and H. A. Atwater, Journal of Applied Physics **98**, 011101 (2005).

[80] C. F. Bohren and D. R. Huffman, *Absorption and Scattering of Light by Small Particles*, John Wiley & Sons, Inc., New York, 1983.

[81] K. L. Kelly, E. Coronado, L. L. Zhao, and G. C. Schatz, Journal of Physical Chemistry B **107**, 668 (2003).

[82] T. A. Klar, M. Perner, S. Grosse, G. von Plessen, W. Spirkl, and J. Feldmann, Physical Review Letters **80**, 4249 (1998).

[83] L. A. Sweatlock, S. A. Maier, H. A. Atwater, J. J. Penninkhof, and A. Polman, Physical Review B **71**, 235408 (2005).

[84] C. L. Haynes, A. D. McFarland, L. L. Zhao, R. P. Van Duyne, G. C. Schatz, L. Gunnarsson, J. Prikulis, B. Kasemo, and M. Kall, Journal of Physical Chemistry B **107**, 7337 (2003).

[85] L. L. Zhao, K. L. Kelly, and G. C. Schatz, Journal of Physical Chemistry B **107**, 7343 (2003).

[86] *Maxwell's Equations by Finite Integration Algorithm (MaFIA)*, Gesellschaft für Computer Simulationstechnik (CST), Darmstadt, Germany, 4th edition, 2000.

[87] E. D. Palik, editor, *Handbook of Optical Constants*, Academic Press, London, 1985.

[88] T. Fischer, V. Petrova-Koch, K. Shcheglov, M. S. Brandt, and F. Koch, Thin Solid Films **276**, 100 (1996).

[89] Y. Ding and J. Erlebacher, Journal of the American Chemical Society **125**, 7772 (2003).

[90] M. L. Brongersma, A. Polman, K. S. Min, and H. A. Atwater, Journal of Applied Physics **86**, 759 (1999).

[91] C. Garcia, B. Garrido, P. Pellegrino, R. Ferre, J. A. Moreno, J. R. Morante, L. Pavesi, and M. Cazzanelli, Applied Physics Letters **82**, 1595 (2003).

[92] D. Kovalev, J. Diener, H. Heckler, G. Polisski, N. Kunzner, and F. Koch, Physical Review B **61**, 4485 (2000).

[93] G. Franzò, S. Coffa, F. Priolo, and C. Spinella, Journal of Applied Physics **81**, 2784 (1997).

[94] C. Delerue, G. Allan, and M. Lannoo, Physical Review B **48**, 11024 (1993).

[95] B. P. van der Gaag and A. Scherer, Applied Physics Letters **56**, 481 (1990).

[96] A. Wokaun, J. P. Gordon, and P. F. Liao, Physical Review Letters **48**, 957 (1982).

[97] R. J. Walters, P. G. Kik, J. D. Casperson, H. A. Atwater, M. Lindstedt, M. Giorgi, and G. Bourianoff, Applied Physics Letters **85**, 2622 (2004).

[98] K. R. Williams, K. Gupta, and M. Wasilik, Journal of Microelectromechanical Systems **12**, 761 (2003).

[99] R. H. Fowler and L. Nordheim, Proceedings of the Royal Society of London, Series A **119**, 173 (1928).

[100] K. Hamad-Schifferli, J. J. Schwartz, A. T. Santos, S. G. Zhang, and J. M. Jacobson, Nature **415**, 152 (2002).

[101] J. J. Penninkhof, T. van Dillen, S. Roorda, C. Graf, A. van Blaaderen, A. M. Vredenberg, and A. Polman, Nuclear Instruments and Methods in Physics Research Section B **242**, 523 (2006).

[102] A. H. Fu, C. M. Micheel, J. Cha, H. Chang, H. Yang, and A. P. Alivisatos, Journal of the American Chemical Society **126**, 10832 (2004).

[103] A. Bansal, X. L. Li, I. Lauermann, N. S. Lewis, S. I. Yi, and W. H. Weinberg, Journal of the American Chemical Society **118**, 7225 (1996).

[104] A. Bansal and N. S. Lewis, Journal of Physical Chemistry B **102**, 1067 (1998).

[105] W. J. Royea, A. Juang, and N. S. Lewis, Applied Physics Letters **77**, 1988 (2000).

[106] J. D. Holmes, K. J. Ziegler, R. C. Doty, L. E. Pell, K. P. Johnston, and B. A. Korgel, Journal of the American Chemical Society **123**, 3743 (2001).

[107] J. P. Wilcoxon, G. A. Samara, and P. N. Provencio, Physical Review B **60**, 2704 (1999).

[108] R. K. Baldwin, K. A. Pettigrew, J. C. Garno, P. P. Power, G. Y. Liu, and S. M. Kauzlarich, Journal of the American Chemical Society **124**, 1150 (2002).

[109] R. D. Tilley, J. H. Warner, K. Yamamoto, I. Matsui, and H. Fujimori, Chemical Communications **14**, 1833 (2005).

[110] R. M. Sankaran, D. Holunga, R. C. Flagan, and K. P. Giapis, Nano Letters **5**, 537 (2005).

[111] Y. Kanemitsu, T. Ogawa, K. Shiraishi, and K. Takeda, Physical Review B **48**, 4883 (1993).

[112] K. A. Littau, P. F. Szajowski, A. J. Muller, A. R. Kortan, and L. E. Brus, Journal of Physical Chemistry **97**, 1224 (1993).

[113] M. L. Ostraat, J. W. De Blauwe, M. L. Green, L. D. Bell, H. A. Atwater, and R. C. Flagan, Journal of the Electrochemical Society **148**, G265 (2001).